2.10 Heat Exchange

The heat exchange with the atmosphere is calculated on basis of the four physical processes

- Latent heat flux (or the heat loss due to vaporisation)
- Sensible heat flux (or the heat flux due to convection)
- Net short wave radiation
- Net long wave radiation

Latent and sensible heat fluxes and long-wave radiation are assumed to occur at the surface. The absorption profile for the short-wave flux is approximated using Beer's law. The attenuation of the light intensity is described through the modified Beer's law as

$$I(d) = (1-\beta)I_0 e^{-\lambda d} \tag{2.99}$$

where $I(d)$ is the intensity at depth d below the surface; I_0 is the intensity just below the water surface; β is a quantity that takes into account that a fraction of light energy (the infrared) is absorbed near the surface; λ is the light extinction coefficient. Typical values for β and λ are 0.2-0.6 and 0.5-1.4 m^{-1}, respectively. β and λ are user-specified constants. The default values are $\beta = 0.3$ and $\lambda = 1.0\ m^{-1}$. The fraction of the light energy that is absorbed near the surface is βI_0. The net short-wave radiation, $q_{sr,net}$, is attenuated as described by the modified Beer's law. Hence the surface net heat flux is given by

$$Q_n = q_v + q_c + \beta q_{sr,net} + q_{lr,net} \tag{2.100}$$

For three-dimensional calculations the source term $\hat{H}$ is given by

$$\hat{H} = \frac{\partial}{\partial z}\left(\frac{q_{sr,net}(1-\beta)e^{-\lambda(\eta-z)}}{\rho_0 c_p}\right) = \frac{q_{sr,net}(1-\beta)\frac{e^{-\lambda(\eta-z)}}{\lambda}}{\rho_0 c_p} \tag{2.101}$$

For two-dimensional calculations the source term $\hat{H}$ is given by

$$\hat{H} = \frac{q_v + q_c + q_{sr,net} + q_{lr,net}}{\rho_0 c_p} \tag{2.102}$$

The calculation of the latent heat flux, sensible heat flux, net short wave radiation, and net long wave radiation as described in the following sections.

In areas covered by ice the heat exchange is excluded.

2.10.1 Vaporisation

Dalton's law yields the following relationship for the vaporative heat loss (or latent flux), see Sahlberg, 1984

$$q_v = LC_e(a_1 + b_1 W_{2m})(Q_{water} - Q_{air}) \tag{2.103}$$

where $L = 2.5 \cdot 10^6 \ J/kg$ is the latent heat vaporisation (in the literature $L = 2.5 \cdot 10^6 - 2300 \ T_{water}$ is commonly used); $C_e = 1.32 \cdot 10^{-3}$ is the moisture transfer coefficient (or Dalton number); W_{2m} is the wind speed 2 m above the sea surface; Q_{water} is the water vapour density close to the surface; Q_{air} is the water vapour density in the atmosphere; a_1 and b_1 are user specified constants. The default values are $a_1 = 0.5$ and $b_1 = 0.9$.

Measurements of Q_{water} and Q_{air} are not directly available but the vapour density can be related to the vapour pressure as

$$Q_i = \frac{0.2167}{T_i + T_k} e_i \tag{2.104}$$

in which subscript i refers to both water and air. The vapour pressure close to the sea, e_{water}, can be expressed in terms of the water temperature assuming that the air close to the surface is saturated and has the same temperature as the water

$$e_{water} = 6.11 e^{K\left(\frac{1}{T_k} - \frac{1}{T_{water} + T_k}\right)} \tag{2.105}$$

where $K = 5418 \ °K$ and $T_K = 273.15 \ °K$ is the temperature at 0 C. Similarly the vapour pressure of the air, e_{air}, can be expressed in terms of the air temperature and the relative humidity, R

$$e_{air} = R \cdot 6.11 e^{K\left(\frac{1}{T_k} - \frac{1}{T_{air} + T_k}\right)} \tag{2.106}$$

Replacing Q_{water} and Q_{air} with these expressions the latent heat can be written as

$$q_v = -P_v\left(a_1 + b_1 W_{2m}\right)\cdot \left(\frac{\exp\left(K\left(\frac{1}{T_k} - \frac{1}{T_{water}+T_k}\right)\right)}{T_{water}+T_k} - \frac{R\cdot\exp\left(K\left(\frac{1}{T_k} - \frac{1}{T_{air}+T_k}\right)\right)}{T_{air}+T_k} \right) \qquad (2.107)$$

where all constants have been included in a new latent constant $P_v = 4370\ J\cdot{}^{\circ}K/m^3$. During cooling of the surface the latent heat loss has a major effect with typical values up to 100 W/m^2.

2.10.2 Convection

The sensible heat flux, $q_c\ (W/m^2)$, (or the heat flux due to convection) depends on the type of boundary layer between the sea surface and the atmosphere. Generally this boundary layer is turbulent implying the following relationship

$$q_c = \begin{cases} \rho_{air} c_{air} c_{heating} W_{10}(T_{air} - T_{water}) & T_{air} \geq T \\ \rho_{air} c_{air} c_{cooling} W_{10}(T_{air} - T_{water}) & T_{air} < T \end{cases} \qquad (2.108)$$

where ρ_{air} is the air density 1.225 kg/m^3; $c_{air} = 1007\ J/(kg\cdot{}^{\circ}K)$ is the specific heat of air; $c_{heating} = 0.0011$ and $c_{cooling} = 0.0011$, respectively, is the sensible transfer coefficient (or Stanton number) for heating and cooling (see Kantha and Clayson, 2000); W_{10} is the wind speed 10 m above the sea surface; T_{water} is the temperature at the sea surface; T_{air} is the temperature of the air.

The convective heat flux typically varies between 0 and 100 W/m^2.

2.10.3 Short wave radiation

Radiation from the sun consists of electromagnetic waves with wave lengths varying from 1,000 to 30,000 Å. Most of this is absorbed in the ozone layer, leaving only a fraction of the energy to reach the surface of the Earth. Furthermore, the spectrum changes when sunrays pass through the atmosphere. Most of the infrared and ultraviolet compound is absorbed such that the solar radiation on the Earth mainly consists of light with wave lengths between 4,000 and 9,000 Å. This radiation is normally termed short wave radiation. The intensity depends on the distance to the sun, declination angle and latitude, extraterrestrial radiation and the cloudiness and amount of water vapour in the atmosphere (see Iqbal, 1983)

The eccentricity in the solar orbit, E_0, is given by

$$E_0 = \left(\frac{r_0}{r}\right)^2 = 1.000110 + 0.034221\cos(\Gamma) + 0.001280\sin(\Gamma) + 0.000719\cos(2\Gamma) + 0.000077\sin(2\Gamma) \tag{2.109}$$

where r_0 is the mean distance to the sun, r is the actual distance and the day angle $\Gamma\ (rad)$ is defined by

$$\Gamma = \frac{2\pi(d_n - 1)}{365} \tag{2.110}$$

and d_n is the Julian day of the year.

The daily rotation of the Earth around the polar axes contributes to changes in the solar radiation. The seasonal radiation is governed by the declination angle, $\delta\ (rad)$, which can be expressed by

$$\begin{aligned}\delta = {} & 0.006918 - 0.399912\cos(\Gamma) + 0.07257\sin(\Gamma) - \\ & 0.006758\cos(2\Gamma) + 0.000907\sin(2\Gamma) - \\ & 0.002697\cos(3\Gamma) + 0.00148\sin(3\Gamma)\end{aligned} \tag{2.111}$$

The day length, n_d, varies with δ. For a given latitude, ϕ, (positive on the northern hemisphere) the day length is given by

$$n_d = \frac{24}{\pi}\arccos\left(-\tan(\phi)\tan(\delta)\right) \tag{2.112}$$

and the sunrise angle, $\omega_{sr}\ (rad)$, and the sunset angle $\omega_{ss}\ (rad)$ are

$$\omega_{sr} = \arccos\left(-\tan(\phi)\tan(\delta)\right) \quad and \quad \omega_{ss} = \omega_{sr} \tag{2.113}$$

The intensity of short wave radiation on the surface parallel to the surface of the Earth changes with the angle of incidence. The highest intensity is in zenith and the lowest during sunrise and sunset. Integrated over one day the extraterrestrial intensity, $H_0\ (MJ/m^2/day)$, in short wave radiation on the surface can be derived as

$$H_0 = \frac{24}{\pi} q_{sc} E_0 \cos(\phi)\cos(\delta)\left(\sin(\omega_{sr}) - \omega_{sr}\cos(\omega_{sr})\right) \tag{2.114}$$

where $q_{sc} = 4.9212\ (MJ/m^2/h)$ is the solar constant.

For determination of daily radiation under cloudy skies, $H\ (MJ/m^2/day)$, the following relation is used

$$\frac{H}{H_0} = a_2 + b_2 \frac{n}{n_d} \tag{2.115}$$

in which n is the number of sunshine hours and n_d is the maximum number of sunshine hours. a_2 and b_2 are user specified constants. The default values are $a_2 = 0.295$ and $b_2 = 0.371$. The user-specified clearness coefficient corresponds to n/n_d. Thus the average hourly short wave radiation, $q_s\ (MJ/m^2/h)$, can be expressed as

$$q_s = \left(\frac{H}{H_0}\right) q_0 \left(a_3 + b_3 \cos(\omega_i)\right) \tag{2.116}$$

where

$$a_3 = 0.4090 + 0.5016 \sin\left(\omega_{sr} - \frac{\pi}{3}\right) \tag{2.117}$$

$$b_3 = 0.6609 + 0.4767 \sin\left(\omega_{sr} - \frac{\pi}{3}\right) \tag{2.118}$$

The extraterrestrial intensity, $q_0\ (MJ/m^2/h)$ and the hour angle ω_i is given by

$$q_0 = q_{sc} E_0 \left(\sin(\phi)\sin(\delta) + \frac{24}{\pi}\cos(\phi)\cos(\delta)\cos(\omega_i)\right) \tag{2.119}$$

$$\omega_i = \frac{\pi}{12}\left(12 + \Delta t_{displacement} + \frac{4}{60}(L_S - L_E) - \frac{E_t}{60} - t_{local}\right) \tag{2.120}$$

$\Delta t_{displacement}$ is the displacement hours due to summer time and the time meridian L_S is the standard longitude for the time zone. $\Delta t_{displacement}$ and L_S are user specified constants. The default values are $\Delta t_{displacement} = 0\ (h)$ and $L_S = 0\ (\deg)$. L_E is the local longitude in degrees. $E_t\ (s)$ is the discrepancy in time due to solar orbit and is varying during the year. It is given by

$$E_t = \begin{pmatrix} 0.000075 + 0.001868\cos(\Gamma) - 0.032077\sin(\Gamma) \\ -0.014615\cos(2\Gamma) - 0.04089\sin(2\Gamma) \end{pmatrix} \cdot 229.18 \tag{2.121}$$

Finally, t_{local} is the local time in hours.

Solar radiation that impinges on the sea surface does not all penetrate the water surface. Parts are reflected back and are lost unless they are backscattered from the surrounding atmosphere. This reflection of solar energy is termed the albedo. The amount of energy, which is lost due to albedo, depends on the angle of incidence and angle of refraction. For a smooth sea the reflection can be expressed as

$$\alpha = \frac{1}{2}\left(\frac{\sin^2(i-r)}{\sin^2(i+r)} + \frac{\tan^2(i-r)}{\tan^2(i+r)}\right) \tag{2.122}$$

where i is the angle of incidence, r the refraction angle and α the reflection coefficient, which typically varies from 5 to 40 %. α can be approximated using

$$\alpha = \begin{cases} \frac{altitude}{5} 0.48 & altitude < 5 \\ \frac{30 - altitude}{25}(0.48 - 0.05) & 5 \le altitude \le 30 \\ 0.05 & altitude > 30 \end{cases} \tag{2.123}$$

where the altitude in degrees is given by

$$altitude = 90 - \left(\frac{180}{\pi}\arccos(\sin(\delta)\sin(\phi) + \cos(\delta)\cos(\phi)\cos(\omega_i))\right) \tag{2.124}$$

Thus the net short wave radiation, $q_{s,net}$ (W/m^2), can eventually be expressed as

$$q_{sr,net} = (1-\alpha)q_s \frac{10^6}{3600} \tag{2.125}$$

2.10.4 Long wave radiation

A body or a surface emits electromagnetic energy at all wavelengths of the spectrum. The long wave radiation consists of waves with wavelengths between 9,000 and 25,000 Å. The radiation in this interval is termed infrared radiation and is emitted from the atmosphere and the sea surface. The long wave emittance from the surface to the atmosphere minus the long wave radiation from the atmosphere to the sea surface is called the net long wave radiation and is dependent on the cloudiness, the air temperature, the vapour pressure in the air and the relative humidity. The net outgoing long wave radiation, $q_{lr,net}$ (W/m^2), is given by Brunt's equation (See Lind and Falkenmark, 1972)

$$q_{lr,net} = -\sigma_{sb}\left(T_{air} + T_K\right)^4\left(a - b\sqrt{e_d}\right)\left(c + d\frac{n}{n_d}\right) \tag{2.126}$$

where e_d is the vapour pressure at dew point temperature measured in mb; n is the number of sunshine hours, n_d is the maximum number of sunshine hours; $\sigma_{sb} = 5.6697 \cdot 10^{-8}\ W/(m^2 \cdot {}^\circ K^4)$ is Stefan Boltzman's constant; $T_{air}\ ({}^\circ C)$ is the air temperature. The coefficients a, b, c and d are given as

$$a = 0.56; b = 0.077 mb^{-1/2}; c = 0.10; d = .90 \tag{2.127}$$

The vapour pressure is determined as

$$e_d = 10 \cdot R\, e_{saturated} \tag{2.128}$$

where R is the relative humidity and the saturated vapour pressure, $e_{saturated}$ (kPa), with 100 % relative humidity in the interval from –51 to 52 °C can be estimated by

$$e_{saturated} = 3.38639 \cdot \left(\left(7.38 \cdot 10^{-3} \cdot T_{air} + 0.8072\right)^8 - 1.9 \cdot 10^{-5}\left|1.8 \cdot T_{air} + 48\right| + 1.316 \cdot 10^{-3}\right) \tag{2.129}$$

3 NUMERICAL SOLUTION

3.1 Spatial Discretization

The discretization in solution domain is performed using a finite volume method. The spatial domain is discretized by subdivision of the continuum into non-overlapping cells/elements.

In the two-dimensional case the elements can be arbitrarily shaped polygons, however, here only triangles and quadrilateral elements are considered.

In the three-dimensional case a layered mesh is used: in the horizontal domain an unstructured mesh is used while in the vertical domain a structured mesh is used (see Figure 3.1gure 3.1). The vertical mesh is based on either sigma coordinates or combined sigma/z-level coordinates. For the hybrid sigma/z-level mesh sigma coordinates are used from the free surface to a specified depth and z-level coordinates are used below. The different types of vertical mesh are illustrated in Figure 3.2. The elements in the sigma domain and the z-level domain can be prisms with either a 3-sided or 4-sided polygonal base. Hence, the horizontal faces are either triangles or quadrilateral element. The elements are perfectly vertical and all layers have identical topology.

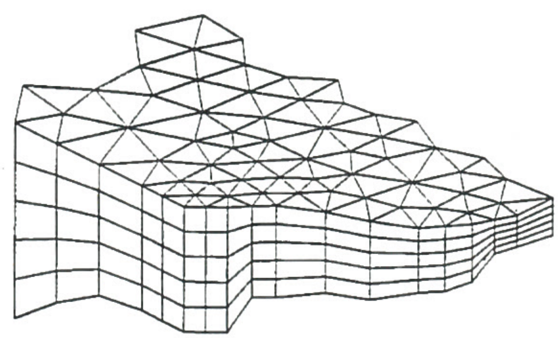

Figure 3.1 Principle of meshing for the three-dimensional case

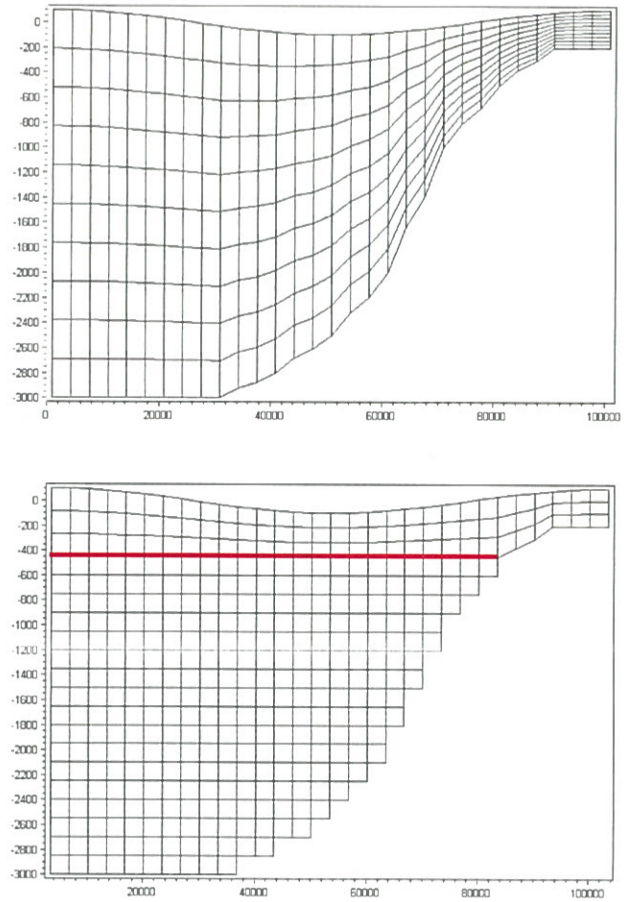

Figure 3.2 *Illustrations of the different vertical grids. Upper: sigma mesh, Lower: combined sigma/z-level mesh with simple bathymetry adjustment. The red line shows the interface between the z-level domain and the sigma-level domain*

The most important advantage using sigma coordinates is their ability to accurately represent the bathymetry and provide consistent resolution near the bed. However, sigma coordinates can suffer from significant errors in the horizontal pressure gradients, advection and mixing terms in areas with sharp topographic changes (steep slopes). These errors can give rise to unrealistic flows.

The use of z-level coordinates allows a simple calculation of the horizontal pressure gradients, advection and mixing terms, but the disadvantages are their inaccuracy in representing the bathymetry and that the stair-step representation of the bathymetry can result in unrealistic flow velocities near the bottom.

3.1.1 Vertical Mesh

For the vertical discretization both a standard sigma mesh and a combined sigma/z-level mesh can be used. For the hybrid sigma/z-level mesh sigma coordinates are used from the free surface to a specified depth, z_σ, and z-level coordinates are used below. At least one sigma layer is needed to allow changes in the surface elevation.

Sigma

In the sigma domain a constant number of layers, N_σ, are used and each sigma layer is a fixed fraction of the total depth of the sigma layer, h_σ, where $h_\sigma = \eta - \max(z_b, z_\sigma)$. The discretization in the sigma domain is given by a number of discrete σ-levels $\{\sigma_i,\ i = 1, (N_\sigma + 1)\}$. Here σ varies from $\sigma_1 = 0$ at the bottom interface of the lowest sigma layer to $\sigma_{N_\sigma+1} = 1$ at the free surface.

Variable sigma coordinates can be obtained using a discrete formulation of the general vertical coordinate (s-coordinate) system proposed by Song and Haidvogel (1994). First an equidistant discretization in a s-coordinate system $(-1 \le s \le 0)$ is defined

$$s_i = -\frac{N_\sigma + 1 - i}{N_\sigma} \qquad i = 1, (N_\sigma + 1) \tag{3.1}$$

The discrete sigma coordinates can then be determined by

$$\sigma_i = 1 + \sigma_c s_i + (1 - \sigma_c) c(s_i) \quad i = 1, (N_\sigma + 1) \tag{3.2}$$

where

$$c(s) = (1 - b)\frac{\sinh(\theta s)}{\sinh(\theta)} + b\frac{\tanh\left(\theta\left(s + \frac{1}{2}\right)\right) - \tanh\left(\frac{\theta}{2}\right)}{2\tanh\left(\frac{\theta}{2}\right)} \tag{3.3}$$

Here σ_c is a weighting factor between the equidistant distribution and the stretch distribution, θ is the surface control parameter and b is the bottom control parameter. The range for the weighting factor is $0<\sigma_c\le 1$ where the value 1 corresponds to equidistant distribution and 0 corresponds to stretched distribution. A small value of σ_c can result in linear instability. The range of the surface control parameter is $0<\theta\le 20$ and the range of the bottom control parameter is $0\le b\le 1$. If $\theta<<1$ and $b=0$ an equidistant vertical resolution is obtained. By increasing the value of the θ, the highest resolution is achieved near the surface. If $\theta>0$ and $b=1$ a high resolution is obtained both near the surface and near the bottom.

Examples of a mesh using variable vertical discretization are shown in Figure 3.3 and Figure 3.4.

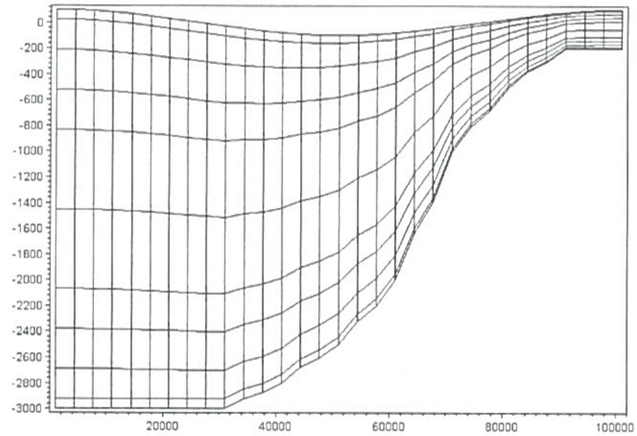

Figure 3.3 Example of vertical distribution using layer thickness distribution. Number of layers: 10, thickness of layers 1 to 10: .025, 0.075, 0.1, 0.01, 0.02, 0.02, 0.1, 0.1, 0.075, 0.025

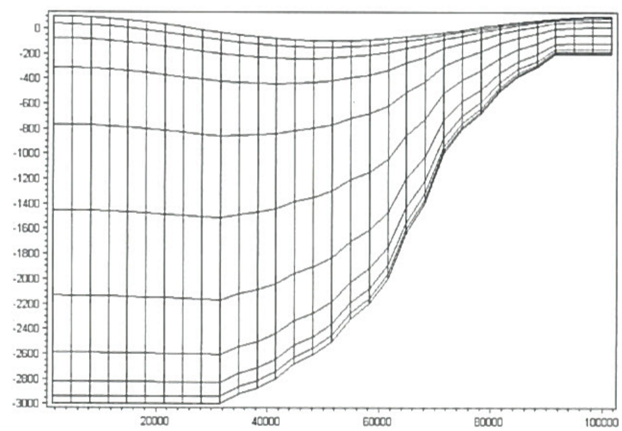

Figure 3.4 Example of vertical distribution using variable distribution. Number of layers: 10, $\sigma_c = 0.1$, $\theta = 5$, $b = 1$

Combined sigma/z-level

In the z-level domain the discretization is given by a number of discrete z-levels $\{z_i,\ i = 1, (N_z + 1)\}$, where N_z is the number of layers in the z-level domain. z_1 is the minimum z-level and z_{N_z+1} is the maximum z-level, which is equal to the sigma depth, z_σ. The corresponding layer thickness is given by

$$\Delta z_i = z_{i+1} - z_i \qquad i = 1, N_z \tag{3.4}$$

The discretization is illustrated in Figure 3.5 and Figure 3.6.

Using standard z-level discretization the bottom depth is rounded to the nearest z-level. Hence, for a cell in the horizontal mesh with the cell-averaged depth, z_b, the cells in the corresponding column in the z-domain are included if the following criteria is satisfied

$$(\mathrm{z}_{i+1} - \mathrm{z}_i)/2 \geq z_b \quad i = 1, N_z \tag{3.5}$$

The cell-averaged depth, z_b, is calculated as the mean value of the depth at the vortices of each cell. For the standard z-level discretization the minimum depth is given by z_1. Too take into account the correct depth for the case where the bottom depth is below the minimum z-level ($z_1 > z_b$) a bottom fitted approach is used. Here, a correction factor, f_1, for the layer thickness in the bottom cell is introduced. The correction factor is used in the calculation of the volume and face integrals. The correction factor for the bottom cell is calculated by

$$f_1 = \frac{(z_2 - z_b)}{\Delta z_1} \tag{3.6}$$

The corrected layer thickness is given by $\Delta z_1^* = f_1 \Delta z_1$. The simple bathymetry adjustment approach is illustrated in Figure 3.5.

For a more accurate representation of the bottom depth an advanced bathymetry adjustment approach can be used. For a cell in the horizontal mesh with the cell-averaged depth, z_b, the cells in the corresponding column in the z-domain are included if the following criteria is satisfied

$$\mathrm{z}_{i+1} > z_b \qquad i = 1, N_z \tag{3.7}$$

A correction factor, f_i, is introduced for the layer thickness

$$f_i = max\left(\frac{(z_{i+1} - z_b)}{\Delta z_i}, \frac{z_{min}}{\Delta z_i}\right) \qquad z_i < z_b < z_{i+1} \;\; or \;\; z_1 > z_b \tag{3.8}$$

$$f_i = 1 \qquad\qquad z_1 \geq z_b$$

A minimum layer thickness, Δz_{min}, is introduced to avoid very small values of the correction factor. The correction factor is used in the calculation of the volume and face integrals. The corrected layer thicknesses are given by $\{\Delta z_i^* = f_i \Delta z_i,\ i = 1, N_z\}$. The advanced bathymetry adjustment approach is illustrated in Figure 3.6.

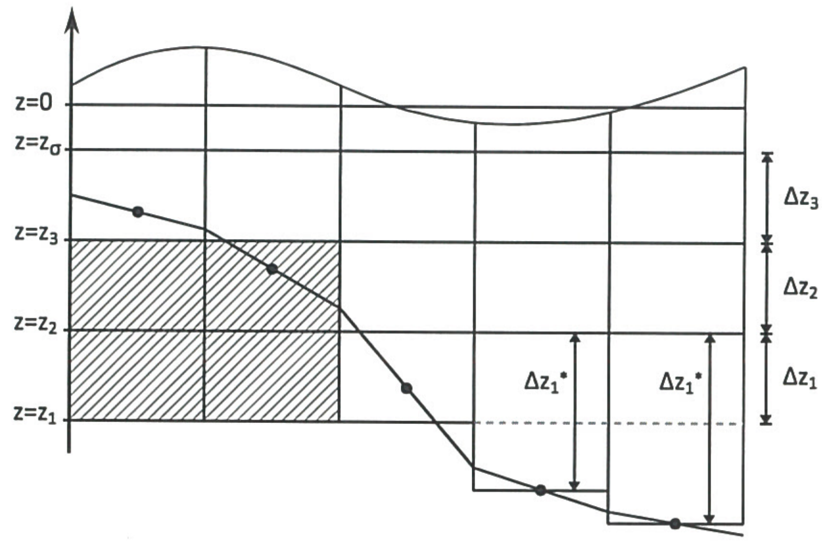

Figure 3.5 Simple bathymetry adjustment approach

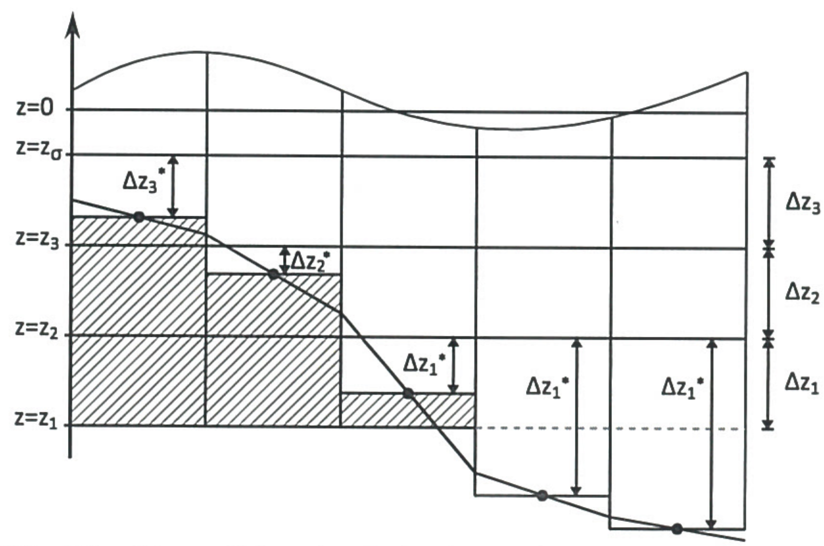

Figure 3.6 Advanced bathymetry adjustment approach

3.1.2 Shallow water equations

The integral form of the system of shallow water equations can in general form be written

$$\frac{\partial \boldsymbol{U}}{\partial t} + \nabla \cdot \boldsymbol{F}(\boldsymbol{U}) = \boldsymbol{S}(\boldsymbol{U}) \tag{3.9}$$

where $\boldsymbol{U}$ is the vector of conserved variables, $\boldsymbol{F}$ is the flux vector function and $\boldsymbol{S}$ is the vector of source terms.

In Cartesian co-ordinates the system of 2D shallow water equations can be written

$$\frac{\partial \boldsymbol{U}}{\partial t}+\frac{\partial\left(\boldsymbol{F}_x^I-\boldsymbol{F}_x^V\right)}{\partial x}+\frac{\partial\left(\boldsymbol{F}_y^I-\boldsymbol{F}_y^V\right)}{\partial y}=\boldsymbol{S} \tag{3.10}$$

where the superscripts I and V denote the inviscid (convective) and viscous fluxes, respectively and where

$$\boldsymbol{U}=\begin{bmatrix} h \\ h\bar{u} \\ h\bar{v} \end{bmatrix},$$

$$\boldsymbol{F}_x^{\,I}=\begin{bmatrix} h\bar{u} \\ h\bar{u}^2+\frac{1}{2}g(h^2-d^2) \\ h\bar{u}\bar{v} \end{bmatrix}, \quad \mathrm{F}_x^{\,V}=\begin{bmatrix} 0 \\ hA\left(2\frac{\partial \bar{u}}{\partial x}\right) \\ hA\left(\frac{\partial \bar{u}}{\partial y}+\frac{\partial \bar{v}}{\partial x}\right) \end{bmatrix}$$

$$\boldsymbol{F}_y^{\,I}=\begin{bmatrix} h\bar{v} \\ h\bar{v}\bar{u} \\ h\bar{v}^2+\frac{1}{2}g(h^2-d^2) \end{bmatrix}_a, \quad \mathrm{F}_y^{\,V}=\begin{bmatrix} 0 \\ hA\left(\frac{\partial \bar{u}}{\partial y}+\frac{\partial \bar{v}}{\partial x}\right) \\ hA\left(2\frac{\partial \bar{v}}{\partial x}\right) \end{bmatrix} \tag{3.11}$$

$$\boldsymbol{S}=\begin{bmatrix} 0 \\ g\eta\frac{\partial d}{\partial x}+f\bar{v}h-\frac{h}{\rho_0}\frac{\partial p_a}{\partial x}-\frac{gh^2}{2\rho_0}\frac{\partial \rho}{\partial x}-\frac{1}{\rho_0}\left(\frac{\partial s_{xx}}{\partial x}+\frac{\partial s_{xy}}{\partial y}\right) \\ +\frac{\tau_{sx}}{\rho_0}-\frac{\tau_{bx}}{\rho_0}+hu_s \\ g\eta\frac{\partial d}{\partial y}-f\bar{u}h-\frac{h}{\rho_0}\frac{\partial p_a}{\partial y}-\frac{gh^2}{2\rho_0}\frac{\partial \rho}{\partial y}-\frac{1}{\rho_0}\left(\frac{\partial s_{yx}}{\partial x}+\frac{\partial s_{yy}}{\partial y}\right) \\ +\frac{\tau_{sy}}{\rho_0}-\frac{\tau_{by}}{\rho_0}+hv_s \end{bmatrix}$$

In Cartesian co-ordinates the system of 3D shallow water equations can be written

$$\frac{\partial \boldsymbol{U}}{\partial t}+\frac{\partial \boldsymbol{F}_x^I}{\partial x'}+\frac{\partial \boldsymbol{F}_y^I}{\partial y'}+\frac{\partial \boldsymbol{F}_\sigma^I}{\partial \sigma}+\frac{\partial \boldsymbol{F}_x^V}{\partial x}+\frac{\partial \boldsymbol{F}_y^V}{\partial y}+\frac{\partial \boldsymbol{F}_\sigma^V}{\partial \sigma}=\boldsymbol{S} \tag{3.12}$$

where the superscripts I and V denote the inviscid (convective) and viscous fluxes, respectively and where

$$\boldsymbol{U}=\begin{bmatrix} h \\ hu \\ hv \end{bmatrix},$$

$$\boldsymbol{F}_x^I=\begin{bmatrix} h\bar{u} \\ hu^2+\frac{1}{2}g(h^2-d^2) \\ huv \end{bmatrix},\quad \boldsymbol{F}_x^V=\begin{bmatrix} 0 \\ hA\left(2\frac{\partial u}{\partial x}\right) \\ hA\left(\frac{\partial u}{\partial y}+\frac{\partial v}{\partial x}\right) \end{bmatrix}$$

$$\boldsymbol{F}_y^I=\begin{bmatrix} h\bar{v} \\ hvu \\ hv^2+\frac{1}{2}g(h^2-d^2) \end{bmatrix},\quad \boldsymbol{F}_y^V=\begin{bmatrix} 0 \\ hA\left(\frac{\partial u}{\partial y}+\frac{\partial v}{\partial x}\right) \\ hA\left(2\frac{\partial v}{\partial x}\right) \end{bmatrix} \tag{3.13}$$

$$\boldsymbol{F}_\sigma^I=\begin{bmatrix} h\omega \\ h\omega u \\ h\omega v \end{bmatrix},\quad \boldsymbol{F}_\sigma^V=\begin{bmatrix} 0 \\ \frac{\upsilon_t}{h}\frac{\partial u}{\partial \sigma} \\ \frac{\upsilon_t}{h}\frac{\partial v}{\partial \sigma} \end{bmatrix}$$

$$\boldsymbol{S}=\begin{bmatrix} 0 \\ g\eta\frac{\partial d}{\partial x}+fvh-\frac{h}{\rho_0}\frac{\partial p_a}{\partial x'}-\frac{hg}{\rho_0}\int_z^\eta\frac{\partial \rho}{\partial x}dz-\frac{1}{\rho_0}\left(\frac{\partial s_{xx}}{\partial x}+\frac{\partial s_{xy}}{\partial y}\right) \\ g\eta\frac{\partial d}{\partial y}-fuh-\frac{h}{\rho_0}\frac{\partial p_a}{\partial y'}-\frac{hg}{\rho_0}\int_z^\eta\frac{\partial \rho}{\partial y}dz-\frac{1}{\rho_0}\left(\frac{\partial s_{yx}}{\partial x}+\frac{\partial s_{yy}}{\partial y}\right) \end{bmatrix}$$

Integrating Eq. (3.9) over the ith cell and using Gauss's theorem to rewrite the flux integral gives

$$\int_{A_i}\frac{\partial \boldsymbol{U}}{\partial t}d\Omega+\int_{\Gamma_i}(\boldsymbol{F}\cdot\boldsymbol{n})\,ds=\int_{A_i}\boldsymbol{S}(\boldsymbol{U})d\Omega \tag{3.14}$$

where A_i is the area/volume of the cell Ω is the integration variable defined on A_i, Γ_i is the boundary of the ith cell and ds is the integration variable along the boundary. $\boldsymbol{n}$ is the unit outward normal vector along the boundary. Evaluating the area/volume integrals by a one-point quadrature rule, the quadrature point being the centroid of the cell, and evaluating the boundary intergral using a mid-point quadrature rule, Eq. (3.14) can be written

$$\frac{\partial U_i}{\partial t} + \frac{1}{A_i} \sum_{j}^{NS} \boldsymbol{F} \cdot \boldsymbol{n}\, \Delta\Gamma_j = S_i \tag{3.15}$$

Here U_i and S_i, respectively, are average values of U and S over the ith cell and stored at the cell centre, NS is the number of sides of the cell, n_j is the unit outward normal vector at the jth side and $\Delta\Gamma_j$ the length/area of the jth interface.

Both a first order and a second order scheme can be applied for the spatial discretization.

For the 2D case an approximate Riemann solver (Roe's scheme, see Roe, 1981) is used to calculate the convective fluxes at the interface of the cells. Using the Roe's scheme the dependent variables to the left and to the right of an interface have to be estimated. Second-order spatial accuracy is achieved by employing a linear gradient-reconstruction technique. The average gradients are estimated using the approach by Jawahar and Kamath, 2000. To avoid numerical oscillations a second order TVD slope limiter (Van Leer limiter, see Hirch, 1990 and Darwish, 2003) is used.

For the 3D case an approximate Riemann solver (Roe's scheme, see Roe, 1981) is used to calculate the convective fluxes at the vertical interface of the cells (x'y'-plane). Using the Roe's scheme the dependent variables to the left and to the right of an interface have to be estimated. Second-order spatial accuracy is achieved by employing a linear gradient-reconstruction technique. The average gradients are estimated using the approach by Jawahar and Kamath, 2000. To avoid numerical oscillations a second order TVD slope limiter (Van Leer limiter, see Hirch, 1990 and Darwish, 2003) is used. The convective fluxes at the horizontal interfaces (vertical line) are derived using first order upwinding for the low order scheme. For the higher order scheme the fluxes are approximated by the mean value of the fluxes calculated based on the cell values above and below the interface for the higher order scheme.

3.1.3 Transport equations

The transport equations arise in the salt and temperature model, the turbulence model and the generic transport model. They all share the form of Equation Eq. (2.20) in Cartesian coordinates. For the 2D case the integral form of the transport equation can be given by Eq. (3.9) where

$$\boldsymbol{U} = h\bar{C}$$

$$\boldsymbol{F}^I = \left[h\bar{u}\bar{C}, \quad h\bar{v}\bar{C}\right]$$
$$\boldsymbol{F}^V = \left[hD_h\frac{\partial\bar{C}}{\partial x}, \quad hD_h\frac{\partial\bar{C}}{\partial y}\right] \tag{3.16}$$

$$\boldsymbol{S} = -hk_p\bar{C} + hC_sS.$$

For the 3D case the integral form of the transport equation can be given by Eq. (3.9) where

$$\boldsymbol{U} = hC$$

$$\boldsymbol{F}^I = \left[huC, \quad hvC, \quad h\omega C\right]$$
$$\boldsymbol{F}^V = \left[hD_h\partial\frac{\partial C}{\partial x}, \quad hD_h\partial\frac{\partial C}{\partial y}, \quad h\frac{D_h}{h}\partial\frac{\partial C}{\partial\sigma}\right] \tag{3.17}$$

$$\boldsymbol{S} = -hk_pC + hC_sS.$$

The discrete finite volume form of the transport equation is given by Eq. (3.15). As for the shallow water equations both a first order and a second order scheme can be applied for the spatial discretization.

In 2D the low order approximation uses simple first order upwinding, i.e., element average values in the upwinding direction are used as values at the boundaries. The higher order version approximates gradients to obtain second order accurate values at the boundaries. Values in the upwinding direction are used. To provide stability and minimize oscillatory effects, a TVD-MUSCL limiter is applied (see Hirch, 1990, and Darwish, 2003).

In 3D the low order version uses simple first order upwinding. The higher order version approximates horizontal gradients to obtain second order accurate values at the horizontal boundaries. Values in the upwinding direction are used. To provide stability and minimize oscillatory effects, an ENO (Essentially Non-Oscillatory) type procedure is applied to limit the horizontal gradients. In the vertical direction a 3rd order ENO procedure is used to obtain the vertical face values (Shu, 1997).

3.2 Time Integration

Consider the general form of the equations

$$\frac{\partial \boldsymbol{U}}{\partial t} = \boldsymbol{G}(\boldsymbol{U}) \tag{3.18}$$

For 2D simulations, there are two methods of time integration for both the shallow water equations and the transport equations: A low order method and a higher order method. The low order method is a first order explicit Euler method

$$\boldsymbol{U}_{n+1} = \boldsymbol{U}_n + \Delta t\ \boldsymbol{G}(\boldsymbol{U}_n) \tag{3.19}$$

where Δt is the time step interval. The higher order method uses a second order Runge Kutta method on the form:

$$\begin{aligned} \boldsymbol{U}_{n+\frac{1}{2}} &= \boldsymbol{U}_n + \tfrac{1}{2}\Delta t\ \boldsymbol{G}(\boldsymbol{U}_n) \\ \boldsymbol{U}_{n+1} &= \boldsymbol{U}_n + \Delta t\ \boldsymbol{G}(\boldsymbol{U}_{n+\frac{1}{2}}) \end{aligned} \tag{3.20}$$

For 3D simulations the time integration is semi-implicit. The horizontal terms are treated implicitly and the vertical terms are treated implicitly or partly explicitly and partly implicitly. Consider the equations in the general semi-implicit form.

$$\frac{\partial \boldsymbol{U}}{\partial t} = \boldsymbol{G}_h(\boldsymbol{U}) + \boldsymbol{G}_v(B\boldsymbol{U}) = \boldsymbol{G}_h(\boldsymbol{U}) + \boldsymbol{G}_v^I(\boldsymbol{U}) + \boldsymbol{G}_v^V(\boldsymbol{U}) \tag{3.21}$$

where the h and v subscripts refer to horizontal and vertical terms, respectively, and the superscripts refer to invicid and viscous terms, respectively. As for 2D simulations, there is a lower order and a higher order time integration method.

The low order method used for the 3D shallow water equations can written as

$$\boldsymbol{U}_{n+1} - \tfrac{1}{2}\Delta t\left(\boldsymbol{G}_v(\boldsymbol{U}_{n+1}) + \boldsymbol{G}_v(\boldsymbol{U}_n)\right) = \boldsymbol{U}_n + \Delta t\ \boldsymbol{G}_h(\boldsymbol{U}_n) \tag{3.22}$$

The horizontal terms are integrated using a first order explicit Euler method and the vertical terms using a second order implicit trapezoidal rule. The higher order method can be written

$$
\begin{aligned}
U_{n+1/2} - \tfrac{1}{4}\Delta t\ \left(G_v(U_{n+1/2}) + G_v(U_n)\right) &= U_n + \tfrac{1}{2}\Delta t\ G_h(U_n) \\
U_{n+1} - \tfrac{1}{2}\Delta t\ \left(G_v(U_{n+1}) + G_v(U_n)\right) &= U_n + \Delta t\ G_h(U_{n+1/2})
\end{aligned}
\qquad (3.23)
$$

The horizontal terms are integrated using a second order Runge Kutta method and the vertical terms using a second order implicit trapezoidal rule.

The low order method used for the 3D transport equation can written as

$$
U_{n+1} - \tfrac{1}{2}\Delta t\left(\ G_v^V(U_{n+1}) + G_v^V(U_n)\right) = U_n + \Delta t\ G_h(U_n) + \Delta t\ G_v^I(\qquad (3.24)
$$

The horizontal terms and the vertical convective terms are integrated using a first order explicit Euler method and the vertical viscous terms are integrated using a second order implicit trapezoidal rule. The higher order method can be written

$$
\begin{aligned}
U_{n+1/2} - \tfrac{1}{4}\Delta t\ \left(G_v^V(U_{n+1/2}) + G_v^V(U_n)\right) &= \\
&U_n + \tfrac{1}{2}\Delta t\ G_h(U_n) + \tfrac{1}{2}\Delta t\ G_v^I(U_n) \\
U_{n+1} - \tfrac{1}{2}\Delta t\ \left(G_v^V(U_{n+1}) + G_v^V(U_n)\right) &= \\
&U_n + \Delta t\ G_h(U_{n+1/2}) + \Delta t\ G_v^I(U_{n+1/2})
\end{aligned}
\qquad (3.25)
$$

The horizontal terms and the vertical convective terms are integrated using a second order Runge Kutta method and the vertical terms are integrated using a second order implicit trapezoidal rule for the vertical terms.

3.3 Boundary Conditions

3.3.1 Closed boundaries

Along closed boundaries (land boundaries) normal fluxes are forced to zero for all variables. For the momentum equations this leads to full-slip along land boundaries.

3.3.2 Open boundaries

The open boundary conditions can be specified either in form of a unit discharge or as the surface elevation for the hydrodynamic equations. For transport equations either a specified value or a specified gradient can be given.

3.3.3 Flooding and drying

The approach for treatment of the moving boundaries problem (flooding and drying fronts) is based on the work by Zhao et al. (1994) and Sleigh et al. (1998). When the depths are small the problem is reformulated and only when the depths are very small the elements/cells are removed from the calculation. The reformulation is made by setting the momentum fluxes to zero and only taking the mass fluxes into consideration.

The depth in each element/cell is monitored and the elements are classified as dry, partially dry or wet. Also the element faces are monitored to identify flooded boundaries.

- An element face is defined as flooded if the following two criteria are satisfied: Firstly, the water depth at one side of face must be less than a tolerance depth, h_{dry}, and the water depth at the other side of the face larger than a tolerance depth, h_{flood}. Secondly, the sum of the still water depth at the side for which the water depth is less than h_{dry} and the surface elevation at the other side must be larger than zero.

- An element is dry if the water depth is less than a tolerance depth, h_{dry}, and no of the element faces are flooded boundaries. The element is removed from the calculation.

- An element is partially dry if the water depth is larger than h_{dry} and less than a tolerance depth, h_{wet}, or when the depth is less than the h_{dry} and one of the element faces is a flooded boundary. The momentum fluxes are set to zero and only the mass fluxes are calculated.

- An element is wet if the water depth is greater than h_{wet}. Both the mass fluxes and the momentum fluxes are calculated.

The wetting depth, h_{wet}, must be larger than the drying depth, h_{dry}, and flooding depth, h_{flood}, must satisfy

$$h_{dry} < h_{flood} < h_{wet} \tag{3.26}$$

The default values are $h_{dry} = 0.005\,m$, $h_{flood} = 0.05\,m$ and $h_{wet} = 0.1\,m$.

Note, that for very small values of the tolerance depth, h_{wet}, unrealistically high flow velocities can occur in the simulation and give cause to stability problems.

4 VALIDATION

The new finite-volume model has been successfully tested in a number of basic, idealised situations for which computed results can be compared with analytical solutions or information from the literature. The model has also been applied and tested in more natural geophysical conditions; ocean scale, inner shelves, estuaries, lakes and overland, which are more realistic and complicated than academic and laboratory tests. A detailed validation report is under preparation.

This chapter presents a comparison between numerical model results and laboratory measurements for a dam-break flow in an L-shaped channel.

Additional information on model validation and applications can be found here

http://mikebydhi.com/Download/DocumentsAndTools/PapersAndDocs.aspx

4.1 Dam-break Flow through Sharp Bend

The physical model to be studied combines a square-shaped upstream reservoir and an L-shaped channel. The flow will be essentially two-dimensional in the reservoir and at the angle between the two reaches of the L-shaped channel. However, there are numerical and experimental evidences that the flow will be mostly unidimensional in both rectilinear reaches. Two characteristics or the dam-break flow are of special interest, namely

- The "damping effect" of the corner
- The upstream-moving hydraulic jump which forms at the corner

The multiple reflections of the expansion wave in the reservoir will also offer an opportunity to test the 2D capabilities of the numerical models. As the flow in the reservoir will remain subcritical with relatively small-amplitude waves, computations could be checked for excessive numerical dissipation.

4.1.1 Physical experiments

A comprehensive experimental study of a dam-break flow in a channel with a 90 bend has been reported by Frazão and Zech (2002, 1999a, 1999b). The channel is made of a 3.92 and a 2.92 metre long and 0.495 metre wide rectilinear reaches connected at right angle by a 0.495 x 0.495 m square element. The channel slope is equal to zero. A guillotine-type gate connects this L-shaped channel to a 2.44 x 2.39 m (nearly) square reservoir. The reservoir bottom level is 33 cm lower that the channel bed level. At the downstream boundary a chute is placed. See the enclosed figure for details.

Frazão and Zech performed measurements for both dry bed and wet bed condition. Here comparisons are made for the case where the water in the reservoir is initially at rest, with the free surface 20 cm above the channel bed level, i.e. the water depth in the reservoir is 53 cm. The channel bed is initially dry. The Manning coefficients evaluated through steady-state flow experimentation are 0.0095 and 0.0195 s/m$^{1/3}$, respectively, for the bed and the walls of the channel.

The water level was measured at six gauging points. The locations of the gauges are shown in Figure 4.1 and the co-ordinates are listed in Table 4.1.

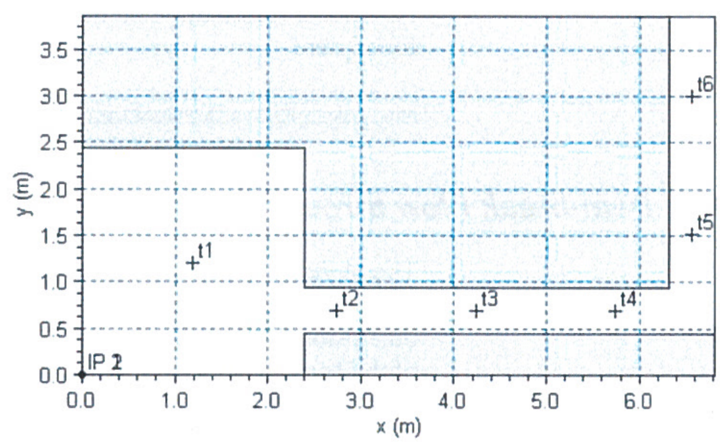

Figure 4.1 Set-up of the experiment by Frazão and Zech (2002)

Table 4.1 Location of the gauging points

Location	x (m)	y (m)
T1	1.19	1.20
T2	2.74	0.69
T3	4.24	0.69
T4	5.74	0.69
T5	6.56	1.51
T6	6.56	3.01

4.1.2 Numerical experiments

Simulations are performed using both the two-dimensional and the three-dimensional shallow water equations.

An unstructured mesh is used containing 18311 triangular elements and 9537 nodes. The minimum edge length is 0.01906 m and the maximum edge length is 0.06125 m. In the 3D simulation 10 layers is used for the vertical discretization. The time step is 0.002 s. At the downstream boundary, a free outfall (absorbing) boundary condition is applied. The wetting depth, flooding depth and drying depth are 0.002 m, 0.001 m and 0.0001 m, respectively.

A constant Manning coefficient of 105.26 $m^{1/3}/s$ is applied in the 2D simulations, while a constant roughness height of $5 \cdot 10^{-5}$ m is applied in the 3D simulation.

4.1.3 Results

In Figure 4.2 time series of calculated surface elevations at the six gauges locations are compared to the measurements. In Figure 4.3 contour plots of the surface elevations are shown at T = 1.6, 3.2 and 4.8 s (two-dimensional simulation).

In Figure 4.4 a vector plot and contour plots of the current speed at a vertical profile along the centre line (from (x,y)=(5.7, 0.69) to (x,y)=(6.4, 0.69)) at T = 6.4 s is shown.

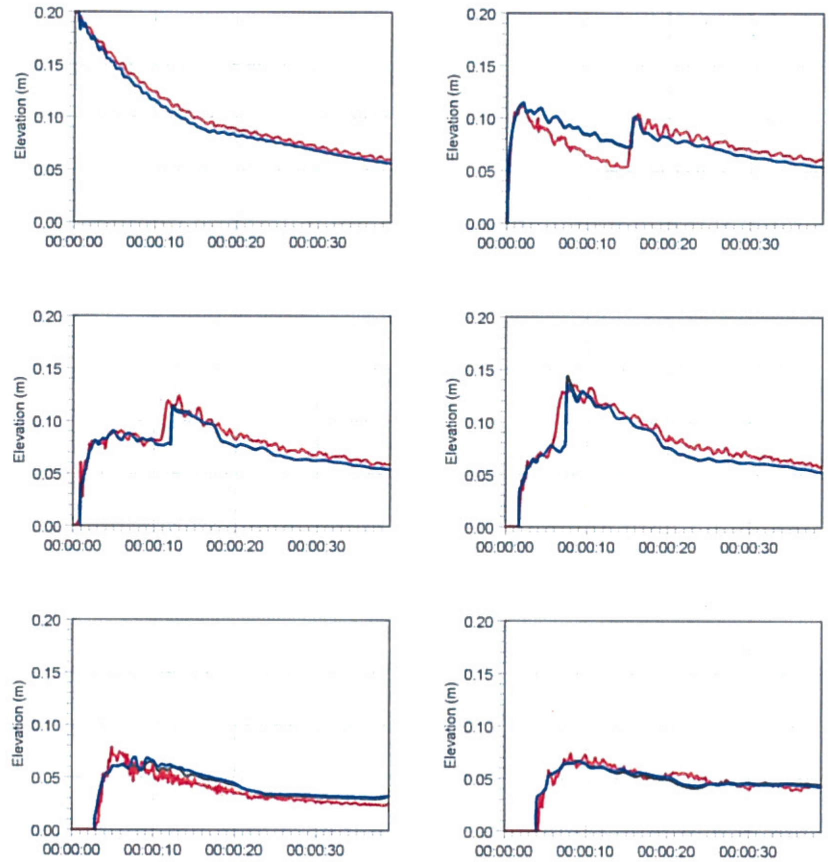

Figure 4.2 *Time evolution of the water level at the six gauge locations. (blue) 3D calculation, (black) 2D calculation and (red) Measurements by Frazão and Zech (1999a,b)*

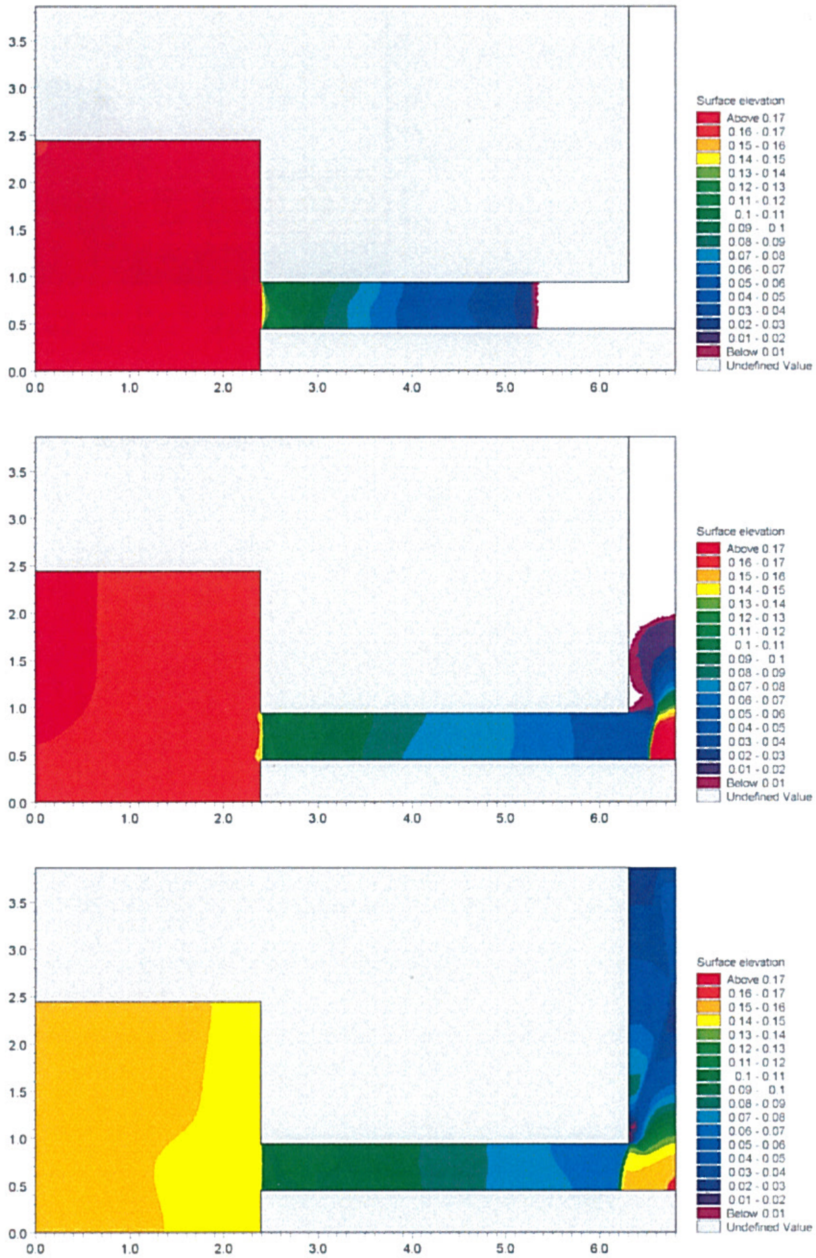

Figure 4.3 *Contour plots of the surface elevation at T = 1.6 s (top), T = 3.2 s (middle) and T = 4.8 s (bottom).*

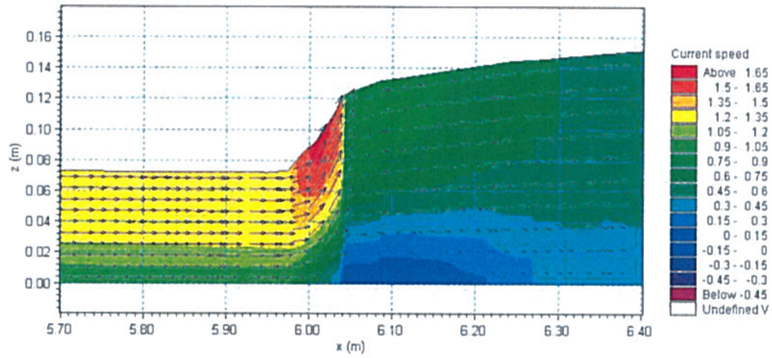

Figure 4.4 *Vector plot and contour plots of the current speed at a vertical profile along the centre line at T = 6.4 s*

5 REFERENCES

Darwish M.S. and Moukalled F. (2003), *TVD schemes for unstructured grids*, Int. J. of Heat and Mass Transfor, 46, 599-611)

Geernaert G.L. and Plant W.L (1990), *Surface Waves and fluxes, Volume 1 – Current theory*, Kluwer Academic Publishers, The Netherlands.

Hirsch, C. (1990). *Numerical Computation of Internal and External Flows, Volume 2*: Computational Methods for Inviscid and Viscous Flows, Wiley.

Iqbal M. (1983). *An Introduction to solar Radiation,* Academic Press.

Jawahar P. and H. Kamath. (2000). *A high-resolution procedure for Euler and Navier-Stokes computations on unstructured grids*, Journal Comp. Physics, 164, 165-203.

Kantha and Clayson (2000). *Small Scale Processes in Geophysical Fluid flows,* International Geophysics Series, Volume 67.

Munk, W., Anderson, E. (1948), *Notes on the theory of the thermocline,* Journal of Marine Research, 7, 276-295.

Lind & Falkenmark (1972), *Hydrology: en inledning till vattenressursläran*, Studentlitteratur (in Swedish).

Pugh, D.T. (1987), *Tides, surges and mean sea-level: a handbook for engineers and scientists*. Wiley, Chichester, 472pp

Rodi, W. (1984), *Turbulence models and their applications in hydraulics,* IAHR, Delft, the Netherlands.

Rodi, W. (1980), *Turbulence Models and Their Application in Hydraulics - A State of the Art Review*, Special IAHR Publication.

Roe, P. L. (1981), *Approximate Riemann solvers, parameter vectors, and difference-schemes*, Journal of Computational Physics, 43, 357-372.

Sahlberg J. (1984). *A hydrodynamic model for heat contents calculations on lakes at the ice formation date,* Document D4: 1984, Swedish council for Building Research.

Shu C.W. (1997), *Essentially Non-Oscillatory and Weighted Essenetially Non-Oscillatory Schemes for Hyperbolic Conservation Laws*, NASA/CR-97-206253, ICASE Report No. 97-65, NASA Langley Research Center, pp. 83.

Smagorinsky (1963), J. *General Circulation Experiment with the Primitive Equations*, Monthly Weather Review, 91, No. 3, pp 99-164.

Sleigh, P.A., Gaskell, P.H., Bersins, M. and Wright, N.G. (1998), *An unstructured finite-volume algorithm for predicting flow in rivers and estuaries*, Computers & Fluids, Vol. **27**, No. 4, 479-508.

Soares Frazão, S. and Zech, Y. (2002), *Dam-break in channel with 90° bend*, Journal of Hydraulic Engineering, ASCE, 2002, **128**, No. 11, 956-968.

Soares Frazão, S. and Zech, Y. (1999a), *Effects of a sharp bend on dam-break flow*, Proc., 28th IAHR Congress, Graz, Austria, Technical Univ. Graz, Graz, Austria (CD-Rom).

Soares Frazão, S. and Zech, Y. (1999b), *Dam-break flow through sharp bends – Physical model and 2D Boltzmann model validation*, Proc., CADAM Meeting Wallingford, U.K., 2-3 March 1998, European Commission, Brussels, Belgium, 151-169.

UNESCO (1981), *The practical salinity scale 1978 and the international equation of state of seawater 1980*, UNESCO technical papers in marine science, 36, 1981.

Wu, Jin (1994), *The sea surface is aerodynamically rough even under light winds*, Boundary layer Meteorology, 69, 149-158.

Wu, Jin (1980), *Wind-stress Coefficients over sea surface and near neutral conditions – A revisit*, Journal of Physical. Oceanography, 10, 727-740.

Zhao, D.H., Shen, H.W., Tabios, G.Q., Tan, W.Y. and Lai, J.S. (1994), *Finite-volume two-dimensional unsteady-flow model for river basins*, Journal of Hydraulic Engineering, ASCE, 1994, **120**, No. 7, 863-833.

STUDY REPORT W&AR-03
RESERVOIR TEMPERATURE MODEL

ATTACHMENT C

DON PEDRO RESERVOIR BATHYMETRIC STUDY REPORT

This Page Intentionally Left Blank.

Don Pedro Reservoir Bathymetric Study Report

Prepared for:

Turlock Irrigation District

Modesto Irrigation District and

Turlock and Modesto, California

Prepared by:

HDR Engineering, Inc.

Sacramento, California

October 2012

Don Pedro Project

FERC No. 2299

TABLE OF CONTENTS

Section No.	Description	Page No.
1.0	Objectives	1
2.0	Study Area	1
3.0	Methods	3
4.0	Results and Analysis	6
5.0	Discussion	7
6.0	References	8

List of Tables

Table No.	Description	Page No.
Table 4.0-1.	Don Pedro Reservoir volume comparison between original elevation storage curve and 2011 bathymetry survey data	6

List of Figures

Figure No.	Description	Page No.
Figure 2.0-1.	Don Pedro bathymetry survey plan transects and water surface gages.	2
Figure 4.0-1.	Don Pedro Reservoir area-capacity curves (reference data: ACOE 1972; 2011 bathymetry study).	7

Attachments

Attachment	Description
A	Quality Assurance Documentation
B	Don Pedro Reservoir Bathymetric Contours (Sheets 1-15)

BATHYMETRIC STUDY REPORT

1.0 Objectives

The objective of this study was to develop an accurate reservoir geometry for the Turlock Irrigation District and Modesto Irrigation District (collectively, the "Districts") Don Pedro Reservoir (FERC No. 2299). The resulting reservoir geometry is also used to update the reservoir's elevation-storage curve and provide data on existing conditions for inclusion in the three-dimensional ("3-D") reservoir temperature model under development in support of the FERC relicensing of the Don Pedro Project ("Project").

2.0 Study Area

The study area consists of Don Pedro Reservoir located in Tuolumne County, California, on the Tuolumne River (Figure 2.0-1). Based on Engineer's estimates developed prior to the construction of the Project, at the normal maximum pool elevation of 830 feet (ft) (NGVD 29), Don Pedro Reservoir has a surface area of 12,960 acres and stores 2,030,000 acre-feet of water (ACOE 1972).

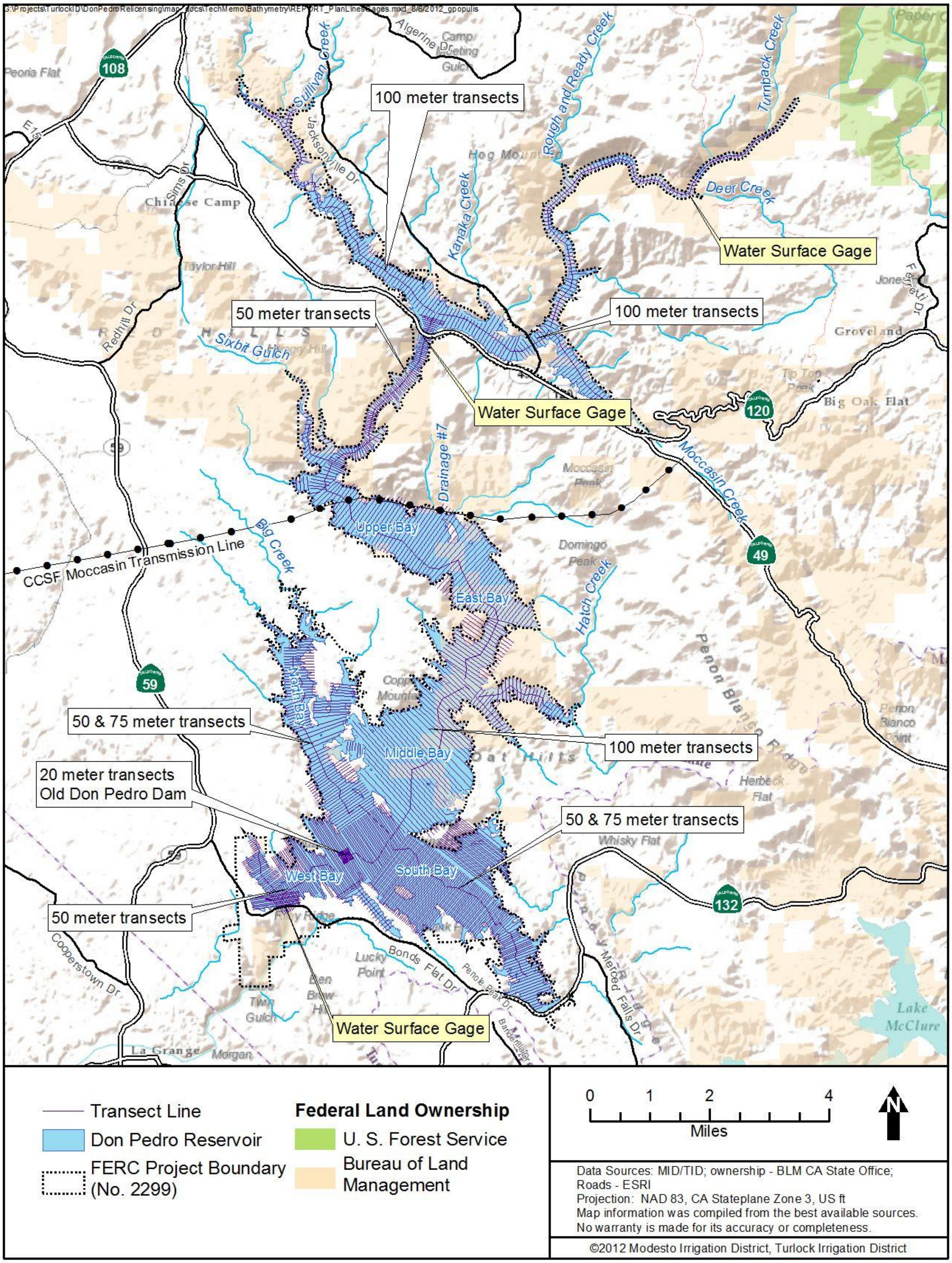

Figure 2.0-1. Don Pedro bathymetry survey plan transects and water surface gages.

3.0 Methods

Bathymetry below the full pool elevation of 830 ft was determined by two techniques: underwater surfaces were surveyed using field measurements (Section 3.1) and topographic information for surfaces above the water were obtained using radar technology (Section 3.2). Data obtained by the two techniques were synthesized into one surface using geographic information system (GIS) software (Section 3.3). Quality assurance and quality control practices are described in Section 3.4.

3.1 Field Survey

The field survey was performed over 16 days between May 1 and June 5, 2011, from a flat-bottom aluminum Johnboat with an outboard motor. This time period was selected due to the relatively high water levels, relatively calm weather, and low amount of recreational boater activity.

During the bathymetric data collection, Don Pedro Reservoir's water surface elevation ranged from approximately 792 ft to 805 ft. Depth data for Don Pedro Reservoir was collected using an Airmar B258 1-kW dual frequency transducer and a Foruno FCV-585 digital depth sounder (with real-time depth profile display) connected to a Trimble PRO-XR GPS and TSC1 Data Collector, capable of providing a real time differential Global Positioning System ("DGPS") data stream. The depth sounder's transducer was mounted onto the side of the boat and lowered 0.3 ft below the surface of the water. The GPS dome antenna was mounted on a platform above the level of the boat. The accuracy of the B258 transducer was ± 0.1 foot of depth (for depths roughly 4 ft or greater) and the accuracy of the PRO-XR GPS receiver was less than one meter of linear distance (with optimal satellite coverage).

Soundings were taken at approximately 1-second intervals and the boat speed was set to ensure that bottom features were appropriately sampled. The boat was navigated along the transect lines using the DGPS, and the position of each sounding was determined using the DGPS system. All depth and horizontal positioning data were recorded digitally in the field as a series of points with x-y-z coordinates, using a rugged field notebook personal computer, running Hypack Hydrographic Survey software.

A total of 1152 transects, spaced at 50, 75, 100 meter intervals and oriented approximately perpendicular to the longitudinal axis of the reservoir, were pre-located and created using Hypack. Areas of topographical concern, such as the Old Don Pedro Dam, were surveyed with greater density for added resolution. In addition to the standard transects, perpendicular "tie lines", oriented approximately parallel to the longitudinal axis of the reservoir and its tributary arms, were established to ensure inter-transect data consistency. A Furuno real-time depth profile display was deployed to identify and navigate areas of topographical concern including confined coves and bars that were found while performing routine grid transects. Transects covered the entire reservoir at the water surface elevation during the time of the field data collection (Figure 2.0-1).

Once all the data were collected, the sounder depth records were edited in Microsoft Excel to remove all but the necessary data to be matched up with a DGPS location and depths were corrected for submergence of the transducer, i.e. the "draft" or the depth from the water surface to the face of the transducer.

Reservoir water level elevations were measured throughout the study from three gages. Water surface elevations near the dam of the reservoir are routinely measured and recorded hourly by TID.[1] For this study, water surface elevation gages were also installed at two other locations, where existing benchmarks provided vertical control for combining all elevation data to a common datum: (1) the Highway 120/49 Bridge across Railroad Canyon (NGS E1389),[2] and (2) the Wards Ferry Bridge (NGS HS4439).[3] All vertical control measurements were then converted to match the vertical datum of the gage at Don Pedro Dam. These reservoir elevations were incorporated into the bathymetric model to adjust each reservoir depth measurement across the reservoir for changes in water surface elevation between the beginning and end of each survey period to the reservoir datum.

The potential existed for an energy slope to form on the surface of Don Pedro Reservoir, as relatively large rates of inflow were observed at the time of the survey.[4] (When an energy slope is present, a reservoir's water surface elevation increases from downstream to upstream.) Hence, on May 5, 2011, a water surface elevation logger (WSEL) was surveyed near the upper end of the reservoir using the monuments at the Highway 120/49 Bridge and at Wards Ferry Bridge. Water surface elevations as detected by the new logger were then compared to the water level as detected by the gage at Don Pedro Dam. After analyzing the collected water level information, it was determined that there was not a measurable energy gradient during the period of survey. Hence, for the purpose of this data collection effort, the water surface of Don Pedro Reservoir was assumed to be flat.

3.2 IFSAR

Topographic information above 792 ft was obtained by interferometric synthetic aperture radar (IFSAR), which was collected by the vendor Intermap during August 2004. The water surface of the reservoir at the time the IFSAR data were collected was 760 ft and the resulting Digital Terrain Model (DTM) extends upwards to well above the reservoir's full pool elevation of 830 ft.

3.3 Surface Model Generation

A contour line at the normal maximum water surface elevation of 830 ft was generated using a GIS contouring tool with the IFSAR DTM. It was visually checked and modified as needed using a horizontally more accurate hi-resolution aerial image.

1 http://www.tid.org/water/hydrological-data
2 http://www.ngs.noaa.gov/cgi-bin/ds_mark.prl?PidBox=HS1389
3 http://www.ngs.noaa.gov/cgi-bin/ds_mark.prl?PidBox=HS4439
4 Inflows to Don Pedro Reservoir ranged from 5,192 cfs to 12,652 cfs during this study (http://cdec.water.ca.gov/).

The bathymetric survey point data were imported into ESRI ArcGIS Desktop software where the point data was integrated with the IFSAR DTM data to make a continuous network of points below the normal maximum water surface contour. That network of points was used develop a network of bottom lines or thalwegs. The points, the bottom lines and the normal maximum water surface contour were then used as input for the ESRI surface interpolation tool "Topo to Raster". The Old Don Pedro Dam was located during the survey and construction drawings of that dam[5] were useful to integrate that feature into the interpolated surface. Contours at 10 ft intervals were then inferred using ESRI contouring tools. The result of this analysis was a continuous surface model that will be used as input to the 3-D reservoir temperature model.

3.4 Quality Assurance and Quality Control

Data quality was assured by following manufacturer's instructions and periodically verifying data values through an alternative measurement (in the field) and third-party review (in the office). Throughout the field survey, the depths measured by the sounder were periodically compared to the actual depth. The actual depth was measured by either lowering a "bar" beneath the sounder or by direct measurement of the bottom with a lead line or pole. Measurement of the "draft" or the depth from the water surface to the face of the transducer was also periodically recorded.

Quality Assurance of the bathymetric surface was performed by an independent reviewer following three steps. The first step consisted of a review of the field methods and materials. The second step consisted of checking the edited raw data. Finally, the third step consisted of verifying the methods used in the production of the final deliverable.

Review of field methods included a review of the "bar checks" performed in the field and described above. In addition, specifications of the sounder and DGPS used in the survey were reviewed to confirm the accuracy of the data as reported. The water surface elevation data at the three gages were also checked for consistency.

Next the processing of the raw data was checked. Any data with DGPS errors or sounding errors that had been flagged by the modeler were checked to confirm that the deletion was appropriate prior to interpolation. Soundings were spot checked for consistency. The crossing of transects and tie-lines was reviewed to ensure that the sounder recorded similar depths at the intersection of survey lines. If any sharp differences in depth at adjacent points were present, they were identified as either an error or a real feature.

The last step was check of the final bathymetric surface (Attachment A). Once the field methods and raw data were reviewed, the production of contours from a bathymetric surface was checked. Calculation of the bottom elevation from sounding depths was reviewed to ensure corrections for the draft and varying water surface elevation were properly accounted for. The method of interpolation and settings used in the interpolation was reviewed to ensure that reasonable contours were generated. Contours created using interpolation were checked against actual soundings to verify that the interpolated surface is reasonable. Finally, contours were checked

[5] TID and MID 1920

against the original elevation-storage curve, as well as historical United States Geological Survey (USGS) maps.

4.0 Results and Analysis

Don Pedro Reservoir contours at 10-ft intervals are displayed along with a shaded relief of the surface in a series of maps at the end of this report (Figures 1 through 15 in Attachment B).

Using the survey data, reservoir volume was calculated in one-foot contour intervals from the bottom of the reservoir to the normal full pool elevation. The calculated storage using the new bathymetry data is compared to the original storage capacity information in Table 4.0-1 and Figure 4.0-1. The original elevation-storage curve indicated that Don Pedro Reservoir at the time of its construction had a total storage capacity of 2,030,000 acre-feet of water at elevation 830 ft (ACOE 1972), while the new bathymetric surface indicates the reservoir holds 2,014,306 acre-feet at that elevation—a difference of less than 1 percent.

Table 4.0-1. Don Pedro Reservoir volume comparison between original elevation storage curve and 2011 bathymetry survey data.

	Cumulative Volume (ac-ft)				Incremental	
Elevation (ft)	Original Storage Curve[1]	2011 Bathymetry Survey	Gain (Loss) in Total Storage[2]	Percent Gain/Loss of Total Storage	Gain (Loss) in Total Storage[2]	Percent
550	158731	158578	(153)	-0.01%	(153)	-0.10%
570	212870	211023	(1,847)	-0.09%	(1,694)	-0.80%
590	274760	272508	(2,252)	-0.11%	(405)	-0.15%
620	384060	382330	(1,730)	-0.09%	523	0.14%
650	517450	516849	(601)	-0.03%	1,129	0.22%
680	678950	677807	(1,143)	-0.06%	(542)	-0.08%
710	869700	867442	(2,258)	-0.11%	(1,116)	-0.13%
740	1094900	1090096	(4,804)	-0.24%	(2,545)	-0.23%
770	1359200	1350810	(8,390)	-0.41%	(3,586)	-0.26%
800	1669000	1657028	(11,972)	-0.59%	(3,582)	-0.21%
830	2030000	2014306	(15,694)	-0.77%	(3,722)	-0.18%

[1]ACOE 1972 Flood Control Manual
[2] Original Survey Volume at Elevation – 2011 Survey Volume at Same Elevation

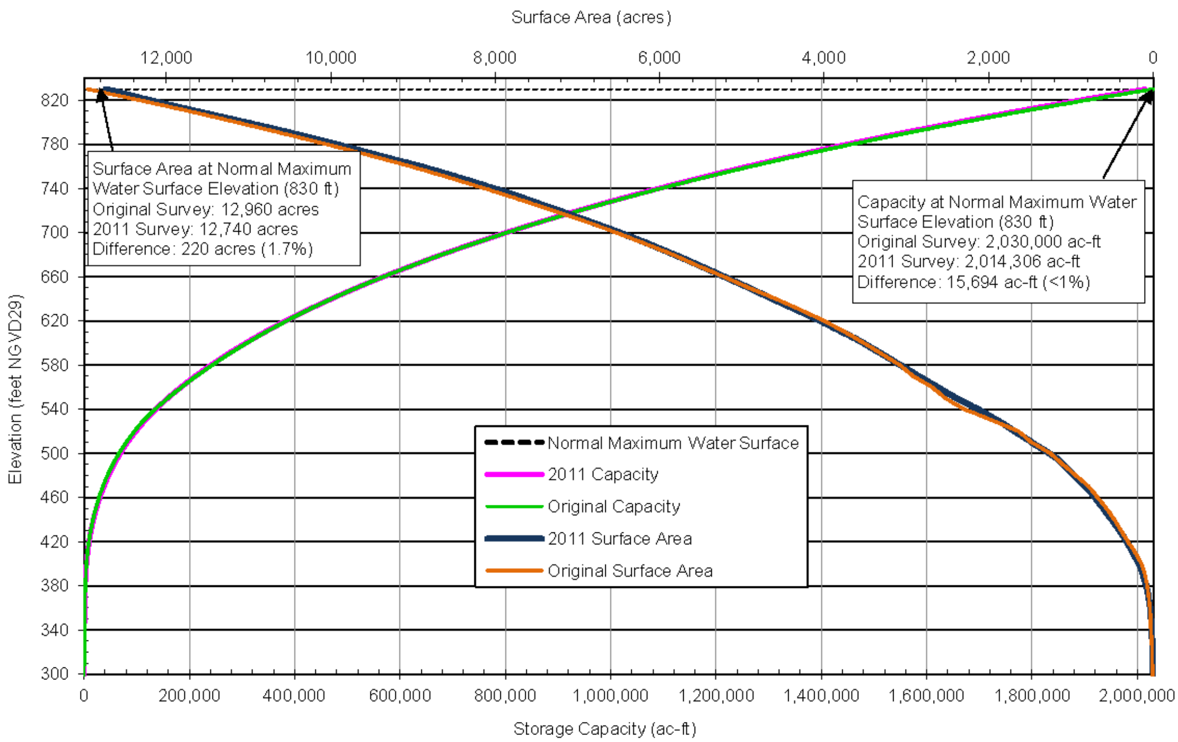

Figure 4.0-1. Don Pedro Reservoir area-capacity curves (reference data: ACOE 1972; 2011 bathymetry study).

5.0 Discussion

As demonstrated in Section 4.0, the storage volumes provided by the original elevation-storage curve and the new bathymetric surface differ by less than 1%. It is recognized that the two estimates were developed based on different survey methods and bathymetric surface calculation methodologies. Other than the elevation-storage curve itself, the input data used to generate the ACOE 1972 curve were not available. However, both methods relied on engineering standards for computations in use at the time of survey, indicating an appropriate level of computational rigor was applied to both estimates. Therefore, it is reasonable to conclude that, for all intents and purposes, the 2011 survey substantially confirms the 1972 elevation-storage information and that any loss of storage in the Don Pedro Reservoir since Project construction can be considered to be minimal.

6.0 References

ACOE. 1972. Report on Reservoir Regulation for Flood Control. Appendix A Flood Control Regulations. Don Pedro Dam and Lake, Tuolumne River, California. Department of the Army. Sacramento District, Corps of Engineers. Sacramento, California. August.

Barnes, D.H. 1987. The Greening of Paradise Valley. The first 100 years (1887-1987) of the Modesto Irrigation District. Commissioned by the Modesto Irrigation District in recognition of its centennial year. 233 pp. Available on line at: http://www.mid.org/about/history/default.html

Environmental Science Research Institute ArcGIS 10. Available online at: <http://help.arcgis.com/en/ arcgisdesktop/10.0/help/index.html>.

Intermap. Available online at: <http://www.intermap.com/>.

TID and MID, 1920. Don Pedro Dam. General Plan of Dam and Spillway. 1 inch = 20 and 40 feet. R.V. Miekle, Chief Engineer. Sheet Number 15 of 42. September. TID file 1-149.

DON PEDRO RESERVOIR
BATHYMETRIC STUDY REPORT

Attachment A

Third Party Bathymetric Survey

This Page Intentionally Left Blank.

Developed by G. Populis 12-9-2011
Updated by R. Olden 12-9-2011
Check Performed by F. Brilhante 12-15-2011

BathPnts_Final: This file is the set of bathymetric point used in the Topo to Raster tool.

- Surface elevations were normalized by using hourly reservoir surface elevation from TID and a lookup table to interpolate elevations for specific times.
    - ***Checked, interpolated elevations were correct and application to bathy data was correct, calculation of bottom elevations was correct***
    - ***Assumed GroundElev = SurfaceElev – CorDepth1 where CorDepth1=RawDepth1+CorDepth2 and Cordepth2 is the boat draft***
- Points with repeating identical and sequential depth reading assumed to be errors and were found and queried out of the dataset.
    - ***This is reasonable***
- Where multiple points near each other disagreed with each other regarding depth readings a decision was made to query out point determined to be errors. Available topo information used where available in making these decisions.
    - ***This is reasonable***

BathPnts_Original: This dataset contains all bathymetric points we collected.

- These are all the originally collected bathymetric points, with surface elevation added through the lookup table and the TID reservoir surface elevations.
- An attribute field was also added and used to query out points before exporting to the final point dataset.
- Codes for comment field used to track the removal of points for final point input file
    - R – Same depth as previous point. Queried out as error.
        - ***ok***
    - X – Removed as error based on visual inspection and comparison with other existing topography.
        - ***Agree with this approach, however points near the old dam should be checked again when the final product is complete***
    - XD – Removed from Old Don Pedro Dam. Plan to add old dam back to surface post interpolation as vector using as-built drawings
        - ***A reasonable approach, note most of the points flagged as XD are between 590 and 607. The old dam had a spillway elevation of 590 and a crest of 607 the data tends to support this . Keep this in mind when adding the old dam to the final product.***

IFSAR_Points_Final_Below_HW: This dataset contains all the IFSAR points below the high water line, without overlapping our BathPnts_Final dataset.

- IFSAR raster which was converted to NGVD29 datum and was converted to points.
    - ***Assume conversion is correct value appear reasonable.***

Developed by G. Populis 12-9-2011
Updated by R. Olden 12-9-2011
Check Performed by F. Brilhante 12-15-2011

- Points within the high water polygon of the reservoir were selected and extracted.
    - ***ok***
- Any points higher than 830 ft. (high water) were removed.
    - ***ok***
- Points at the reservoir surface elevation, 762.9 ft, and below at the time the IFSAR data was collected were removed.
    - ***ok***
- Any points within 50 ft. of our bathymetry points were removed.
    - ***Ok a check of IFSAR data to our bathy data shows good agreement***
- Any points that were within 18 ft. of the high water line and were more than 24 ft. lower than 830 ft. (below 806 ft.) were removed. This was done due to a slight imperfection in the alignment between the IFSAR data and our bathymetric points. We did not want to be creating large flat spots or cliffs where none existed. (We made an exception to this rule for the points in Boxcar Canyon where steeper slopes are normal.
    - ***ok***

IFSAR_Points_Final_Above_HW: This dataset contains all the IFSAR points above the high water line, and is used mainly to inform the slope near the high water line.

- IFSAR raster which was converted to NGVD29 datum was converted to points.
    - ***ok***
- Any points below 830 were removed.
    - ***ok***
- Points within 18 ft. of the high water line and more than 24 ft. above 830 ft. elevation (Above 854 ft.) were removed. (Same reason as previous section.)
    - ***ok***

BottomLine_Final: This dataset shows a representation of the drainages / low point of the underwater topology. This is used primarily to inform the interpolation of the points into a raster elevation file.

This approach is reasonable and will yield a good surface for use in modeling.

- Main Tuolumne River drainage was aligned using the lowest point from each transect in the bathymetric data. Old topographic maps were used to inform the decision making process.
- Other major drainages were created using the same techniques.
- Where possible aerial imagery was used to align drainages. Reservoir elevation was about 750 ft. when the aerial imagery was flown.
- Old topographic maps were used to adjust bottom lines where gaps in the bathymetric data and aerial photos existed.
- Other bottom lines were created using flow lines created by the 'topo to raster' tool in ArcInfo 10 3D Analyst.

Developed by G. Populis 12-9-2011
Updated by R. Olden 12-9-2011
Check Performed by F. Brilhante 12-15-2011

Highwater_Line_Final: This is a linear representation of the high water line around Don Pedro Reservoir and is used as a contour line (830 ft.) to inform the interpolation.

- Original high water line was created from a mix of ESRI CD data "Teleatlas" and IFSAR data.
- Updates were made utilizing the 1 ft. pixel aerial photography and reprocessed IFSAR data.
    - ***Was the level of the reservoir known when the aerial was flown?***

DP_Bathy: This is the elevation raster created by the Topo to Raster tool. This will be processed later to create the final terrain.

- DP_Bathy was created using the Topo to Raster tool in 3D Analyst using the settings shown below. (error message is because tool was already run and file name already exists
    - ***The resultant surface looks good. I will check it again when the data is collected and the interpolation looks sound.***
    - ***The hillshade, however, makes it look like there are artifacts from the data. I recommend either not using it or taking steps to smooth it out some more***

Developed by G. Populis 12-9-2011
Updated by R. Olden 12-9-2011
Check Performed by F. Brilhante 12-15-2011

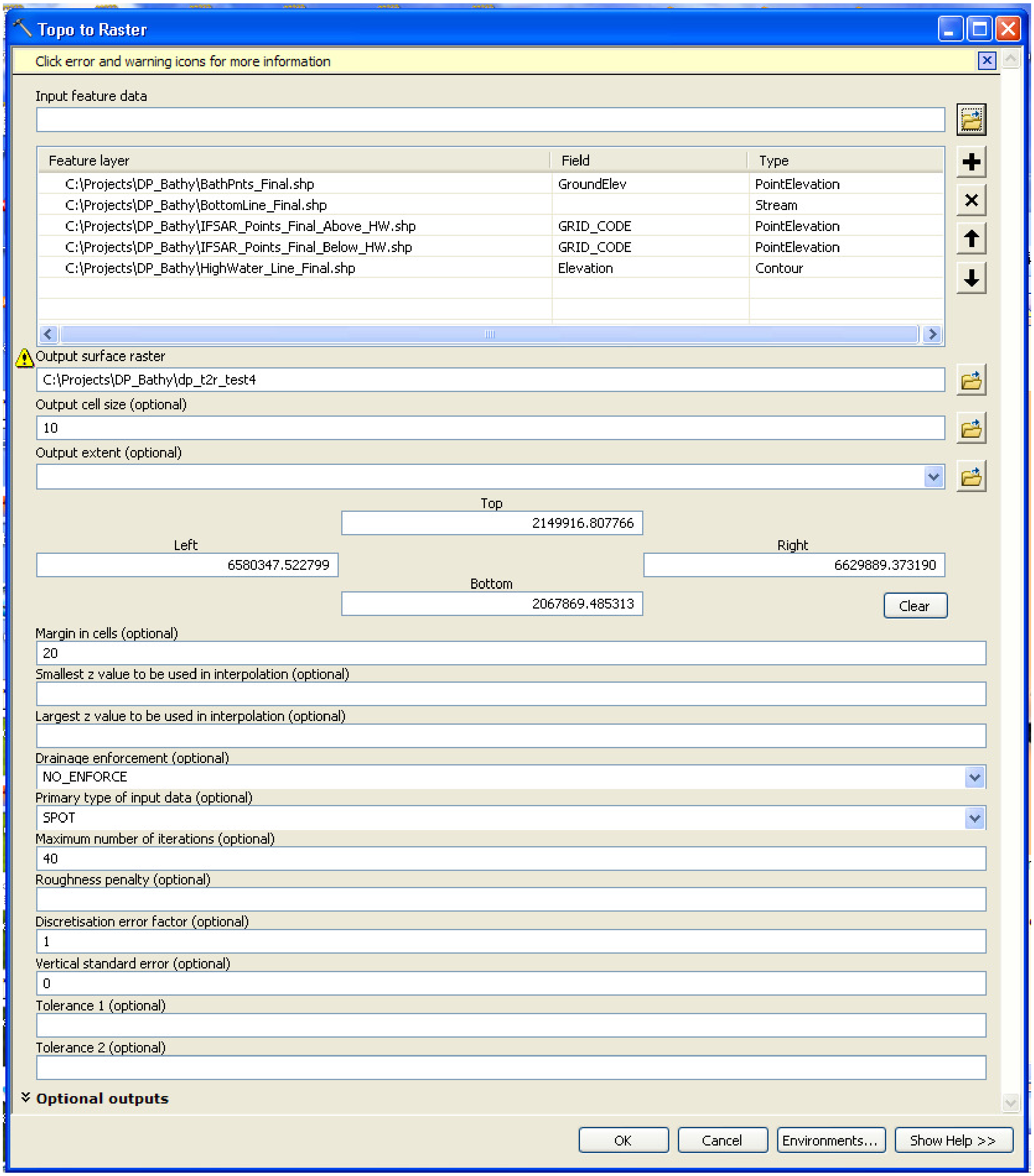

DON PEDRO RESERVOIR
BATHYMETRIC STUDY REPORT

Attachment B

Don Pedro Reservoir Bathymetric Contours (Sheets 1 - 15)

This Page Intentionally Left Blank.

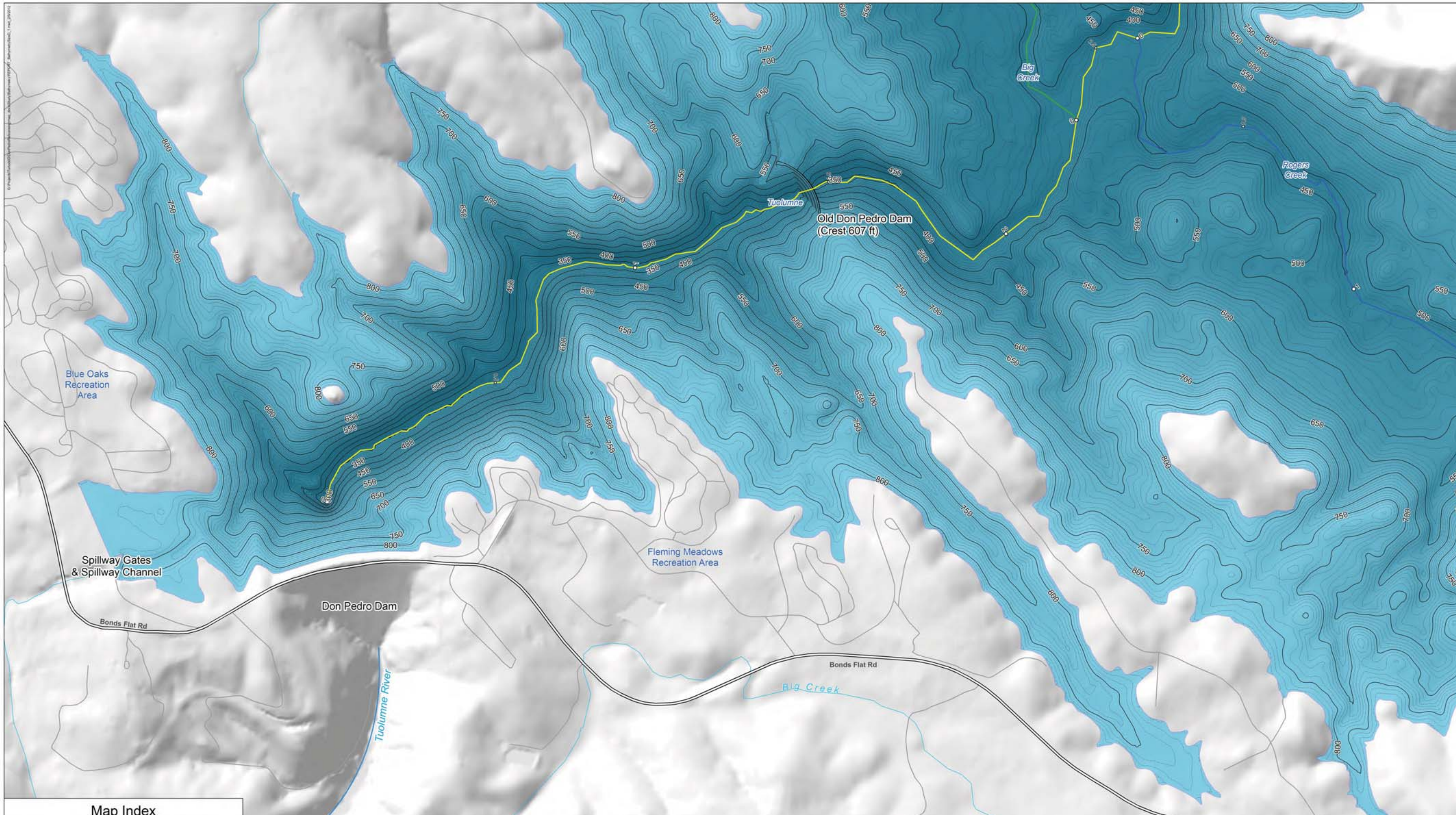

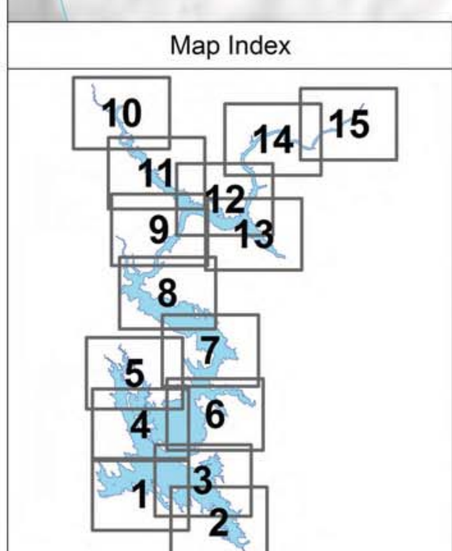

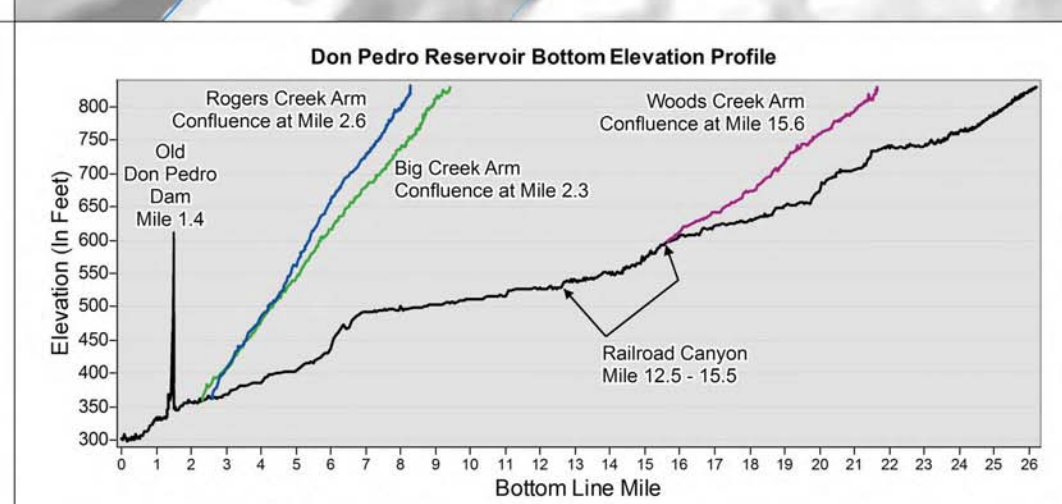

Modesto Irrigation District &
Turlock Irrigation District

Don Pedro Reservoir
Bathymetric Contours

Figure 1.4-3
Sheet 1 of 15

Bathymetric survey conducted May 1st, 2011 to June 5th, 2011
10 Foot Contour Elevation in
National Geodesic Vertical Datum of 1929 (NGVD29)
Prepared by: HDR Engineering Inc.

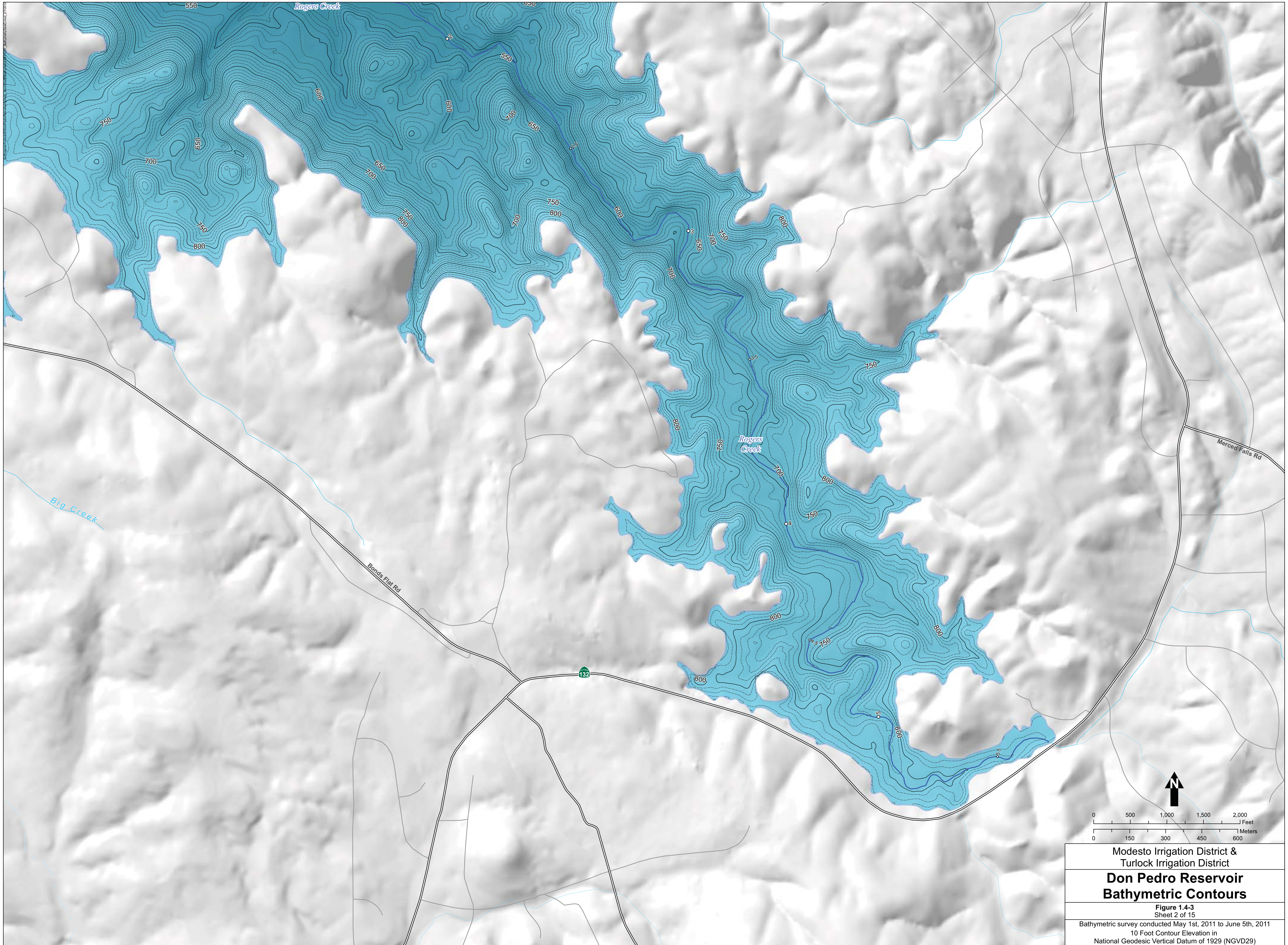

Modesto Irrigation District &
Turlock Irrigation District

Don Pedro Reservoir Bathymetric Contours

Figure 1.4-3
Sheet 2 of 15

Bathymetric survey conducted May 1st, 2011 to June 5th, 2011
10 Foot Contour Elevation in
National Geodesic Vertical Datum of 1929 (NGVD29)
Prepared by: HDR Engineering Inc.

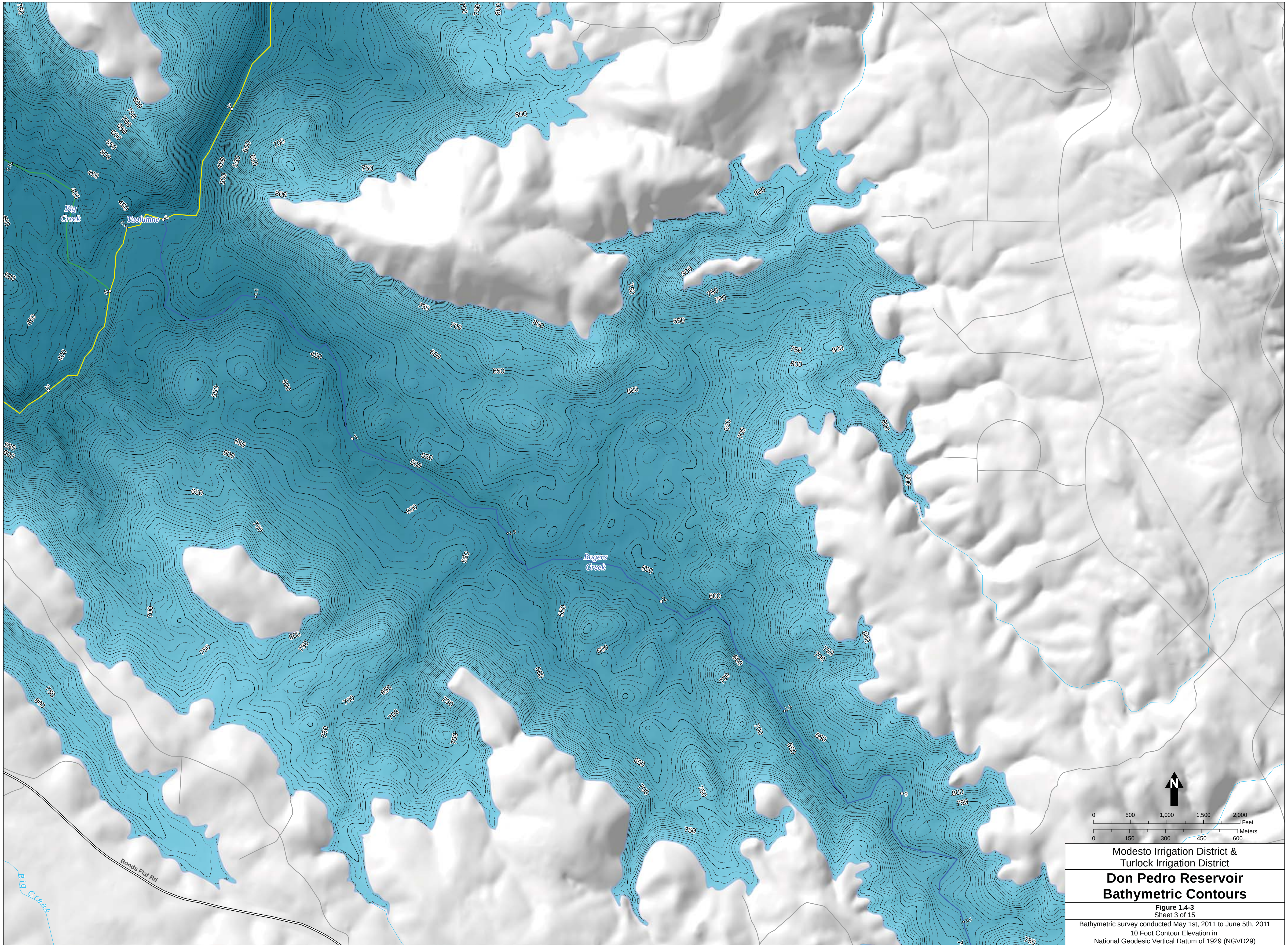

Modesto Irrigation District &
Turlock Irrigation District

Don Pedro Reservoir
Bathymetric Contours

Figure 1.4-3
Sheet 3 of 15

Bathymetric survey conducted May 1st, 2011 to June 5th, 2011
10 Foot Contour Elevation in
National Geodesic Vertical Datum of 1929 (NGVD29)
Prepared by: HDR Engineering Inc.

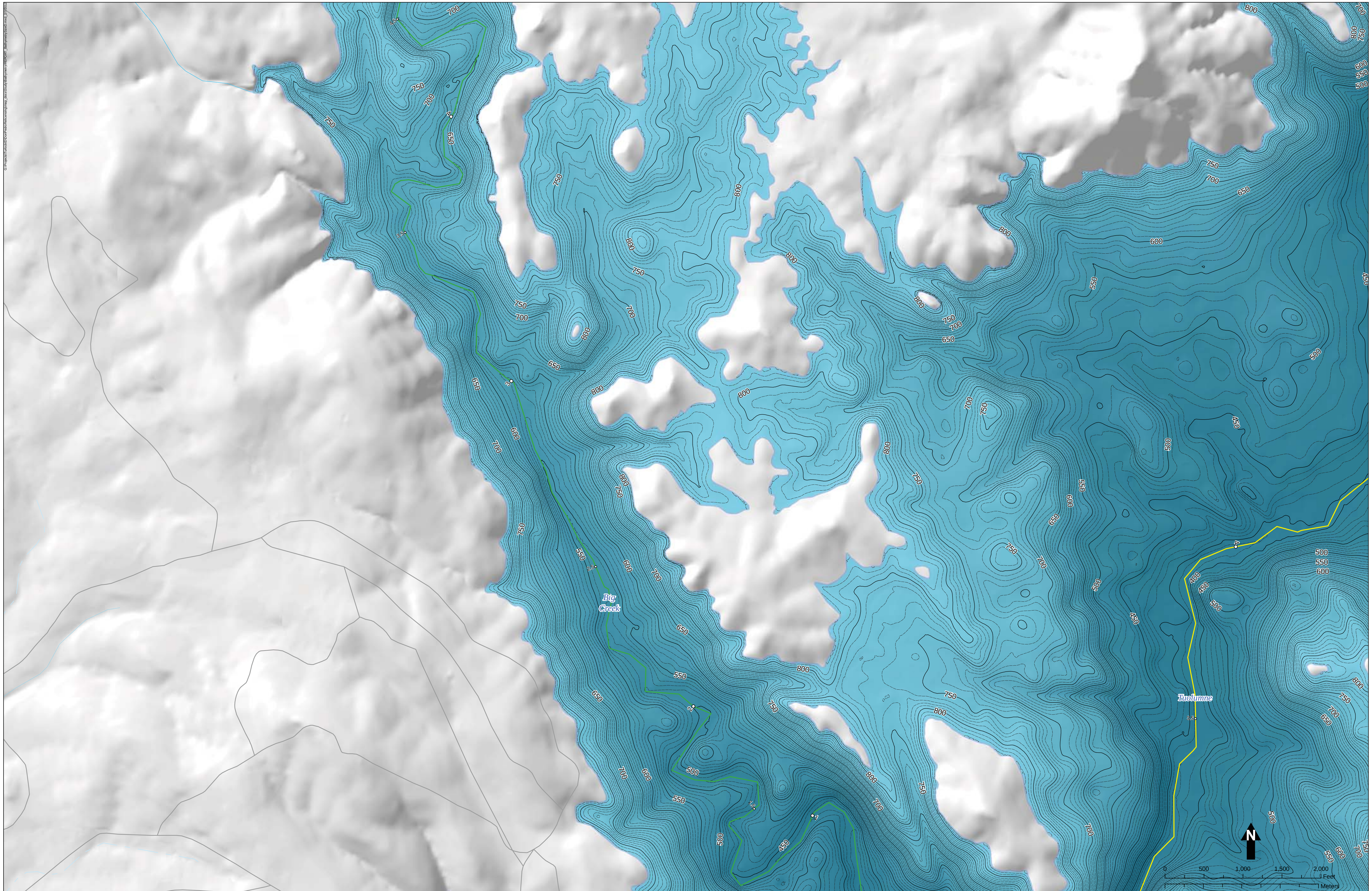

Modesto Irrigation District &
Turlock Irrigation District

Don Pedro Reservoir
Bathymetric Contours

Figure 1.4-3
Sheet 4 of 15

Bathymetric survey conducted May 1st, 2011 to June 5th, 2011
10 Foot Contour Elevation in
National Geodesic Vertical Datum of 1929 (NGVD29)
Prepared by: HDR Engineering Inc.

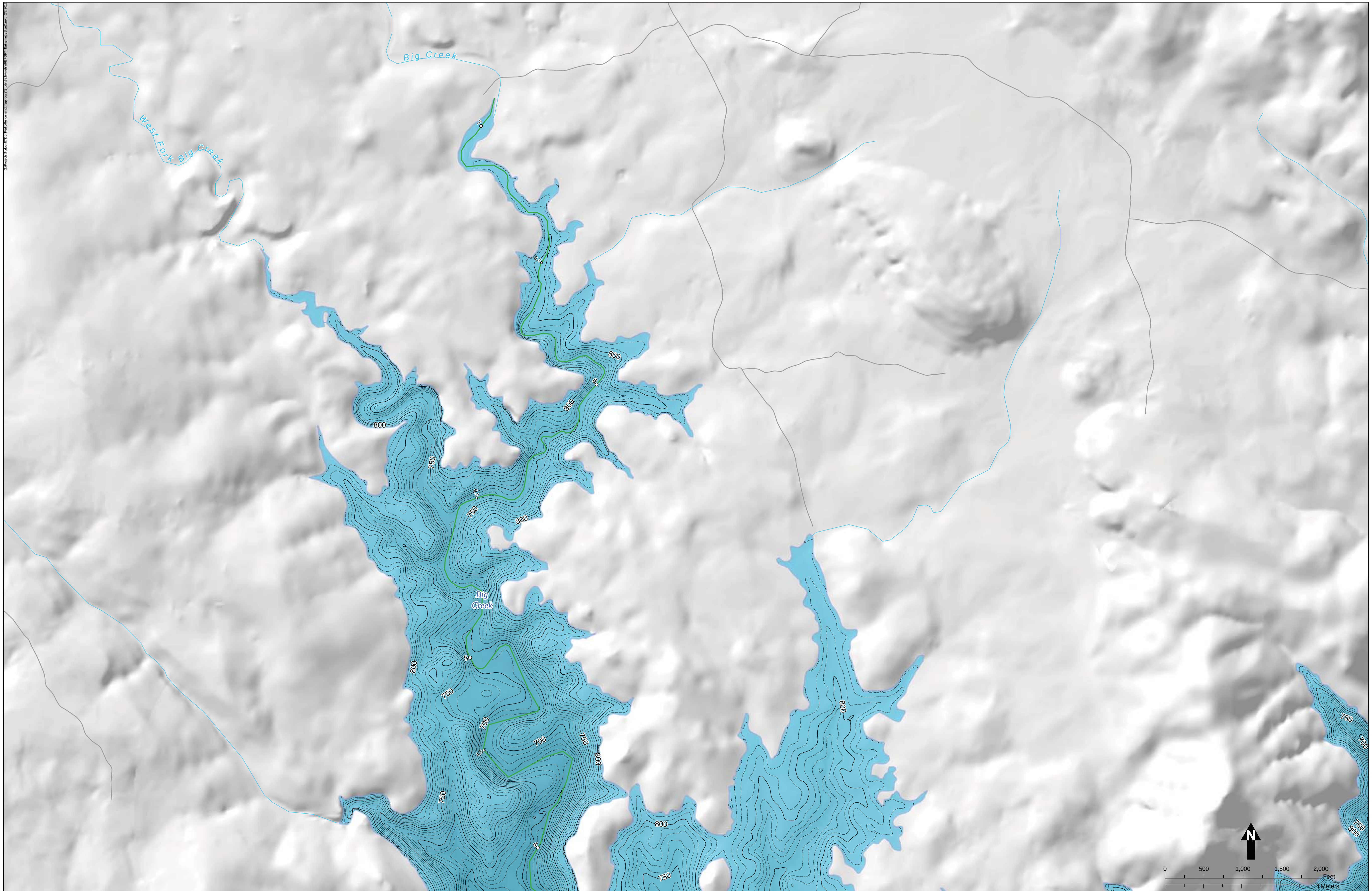

Modesto Irrigation District &
Turlock Irrigation District

Don Pedro Reservoir
Bathymetric Contours

Figure 1.4-3
Sheet 5 of 15

Bathymetric survey conducted May 1st, 2011 to June 5th, 2011
10 Foot Contour Elevation in
National Geodesic Vertical Datum of 1929 (NGVD29)
Prepared by: HDR Engineering Inc.

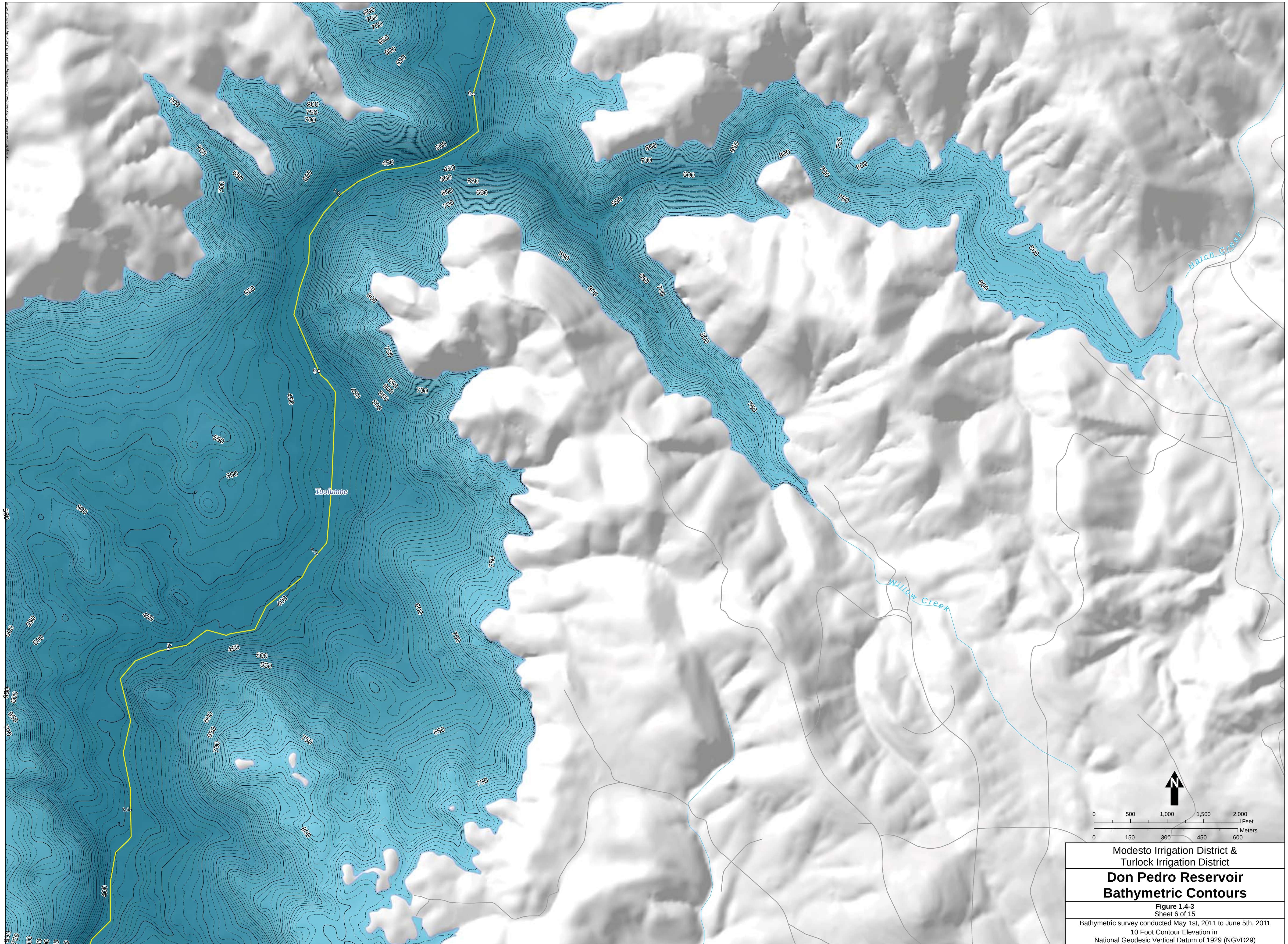

Modesto Irrigation District &
Turlock Irrigation District

Don Pedro Reservoir
Bathymetric Contours

Figure 1.4-3
Sheet 6 of 15

Bathymetric survey conducted May 1st, 2011 to June 5th, 2011
10 Foot Contour Elevation in
National Geodesic Vertical Datum of 1929 (NGVD29)
Prepared by: HDR Engineering Inc.

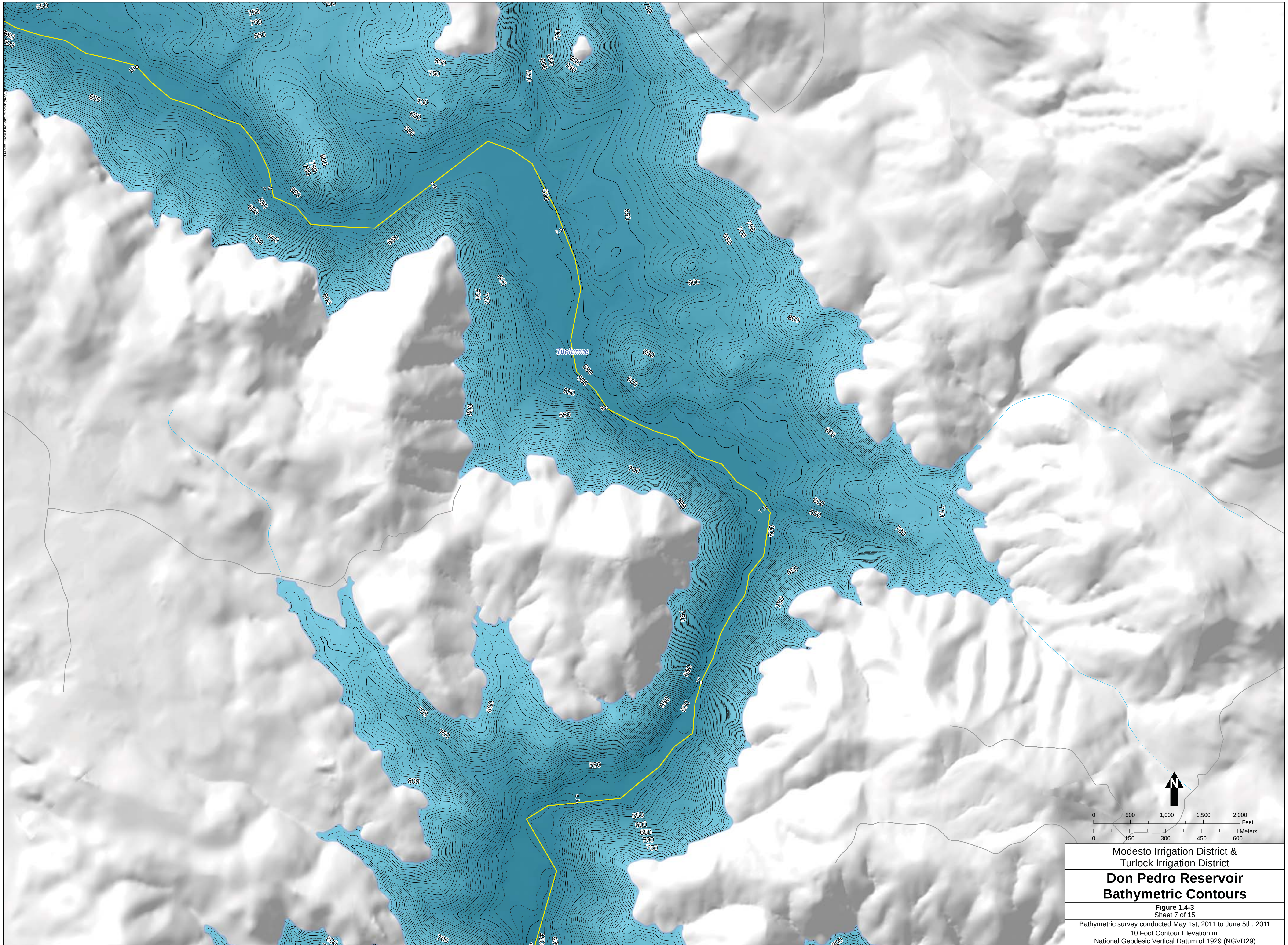

Modesto Irrigation District &
Turlock Irrigation District

Don Pedro Reservoir
Bathymetric Contours

Figure 1.4-3
Sheet 7 of 15

Bathymetric survey conducted May 1st, 2011 to June 5th, 2011
10 Foot Contour Elevation in
National Geodesic Vertical Datum of 1929 (NGVD29)
Prepared by: HDR Engineering Inc.

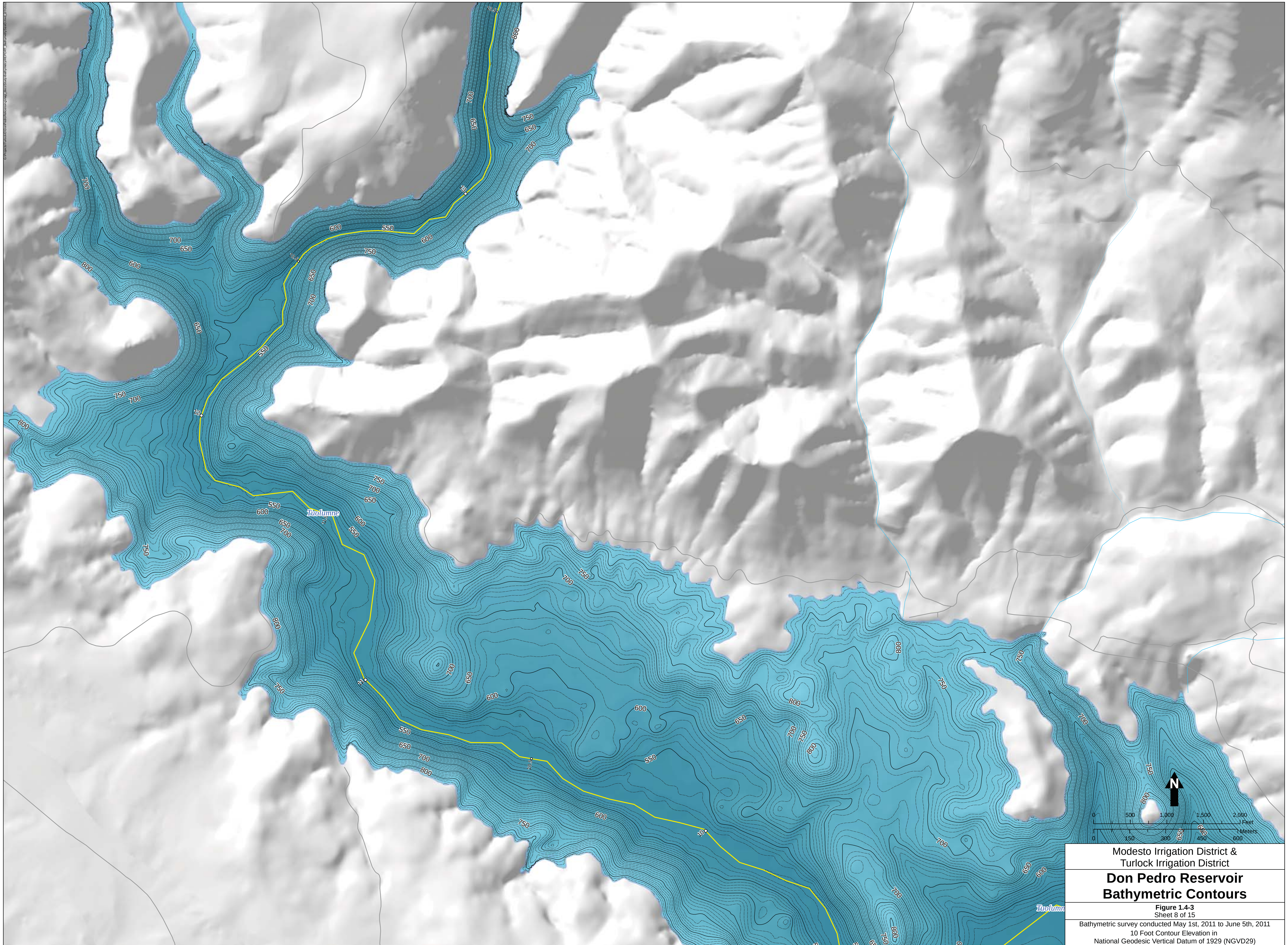

Modesto Irrigation District &
Turlock Irrigation District

Don Pedro Reservoir Bathymetric Contours

Figure 1.4-3
Sheet 8 of 15

Bathymetric survey conducted May 1st, 2011 to June 5th, 2011
10 Foot Contour Elevation in
National Geodesic Vertical Datum of 1929 (NGVD29)
Prepared by: HDR Engineering Inc.

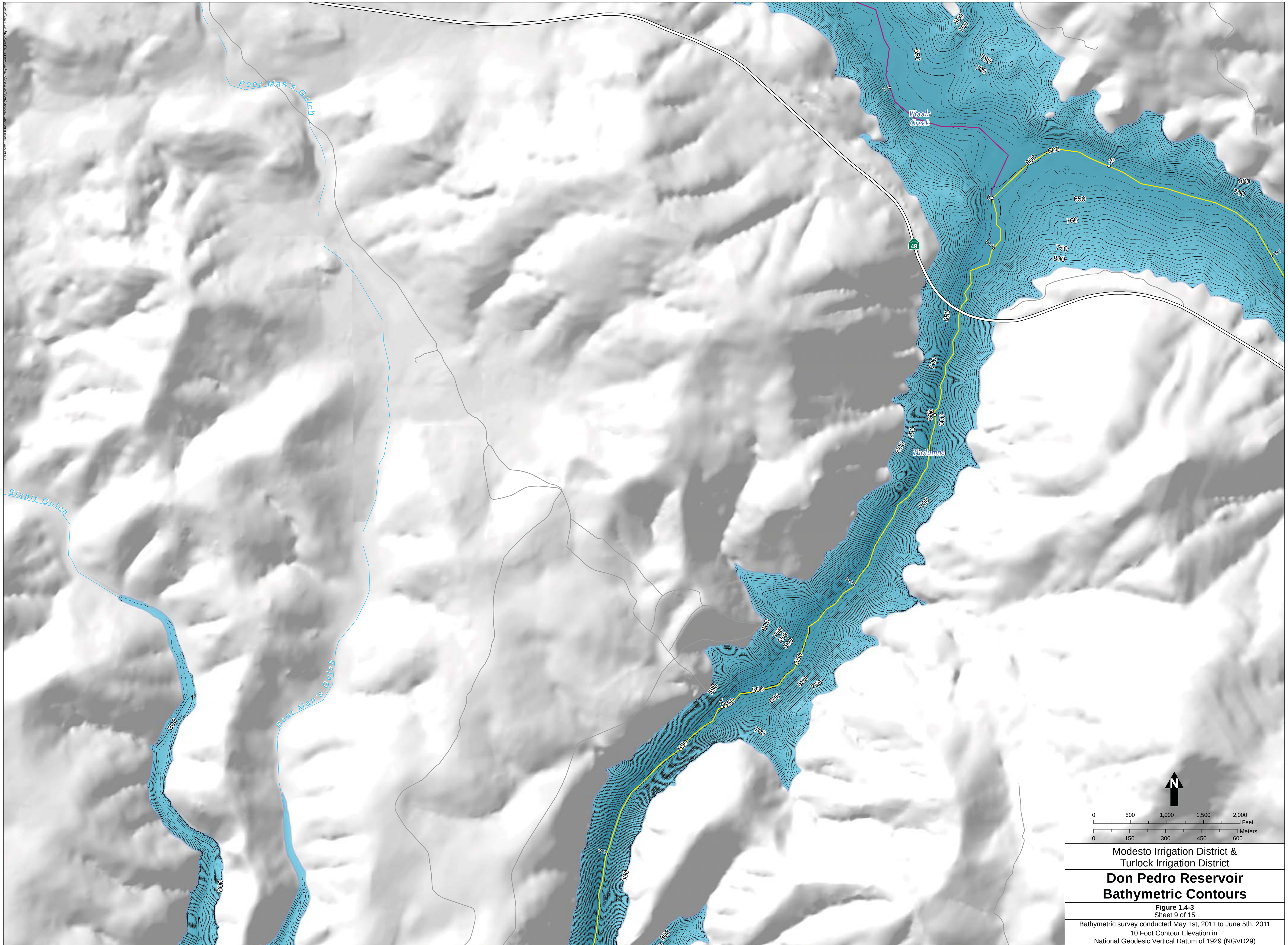

Modesto Irrigation District &
Turlock Irrigation District

Don Pedro Reservoir
Bathymetric Contours

Figure 1.4-3
Sheet 9 of 15

Bathymetric survey conducted May 1st, 2011 to June 5th, 2011
10 Foot Contour Elevation in
National Geodesic Vertical Datum of 1929 (NGVD29)
Prepared by: HDR Engineering Inc.

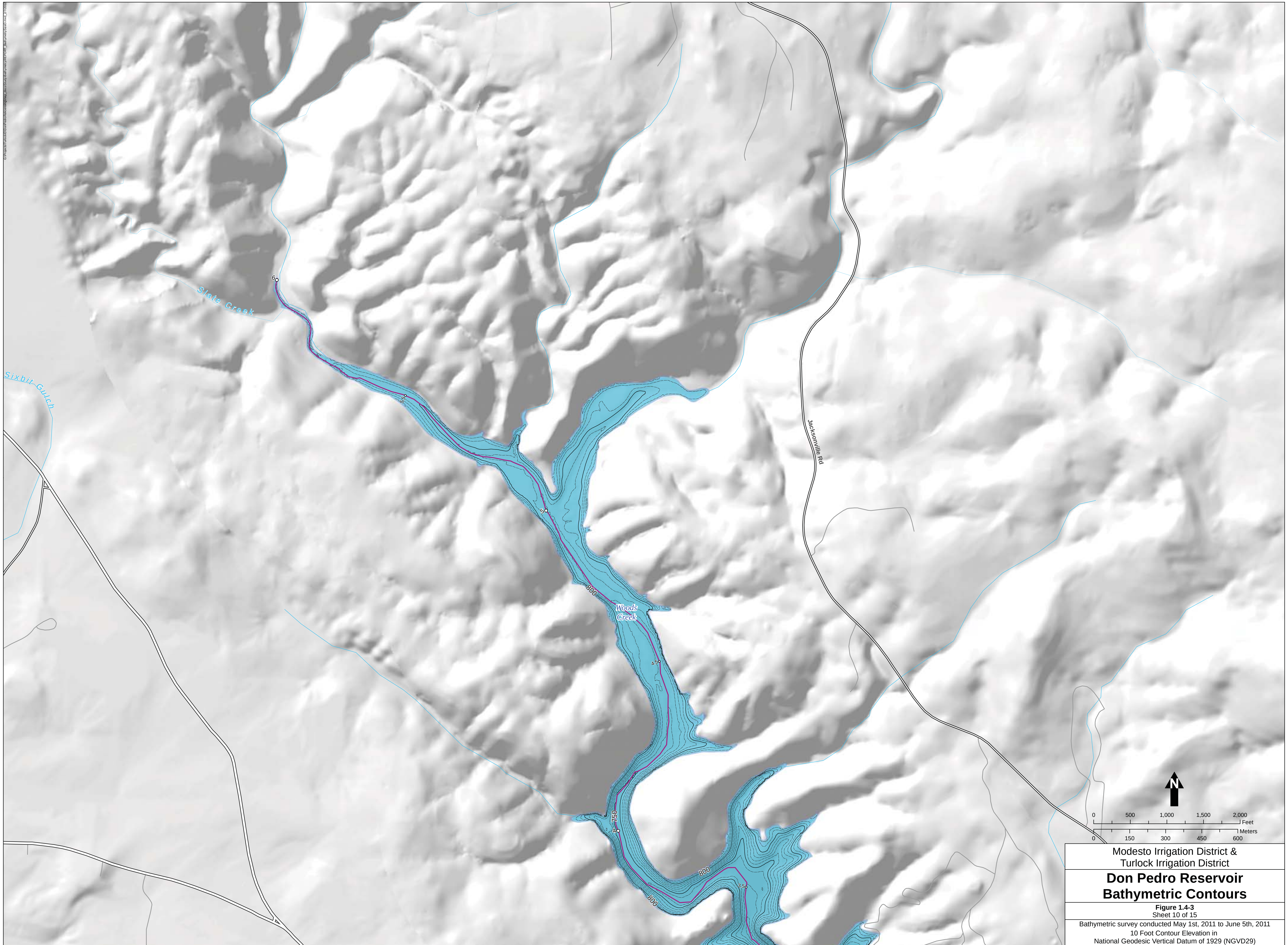

Slate Creek
Sixbit Gulch
Jacksonville Rd
Woods Creek
800
750
800
800
N
0
500
1,000
1,500
2,000
Feet
0
150
300
450
600
Meters
Modesto Irrigation District &
Turlock Irrigation District
Don Pedro Reservoir
Bathymetric Contours
Figure 1.4-3
Sheet 10 of 15
Bathymetric survey conducted May 1st, 2011 to June 5th, 2011
10 Foot Contour Elevation in
National Geodesic Vertical Datum of 1929 (NGVD29)
Prepared by: HDR Engineering Inc.

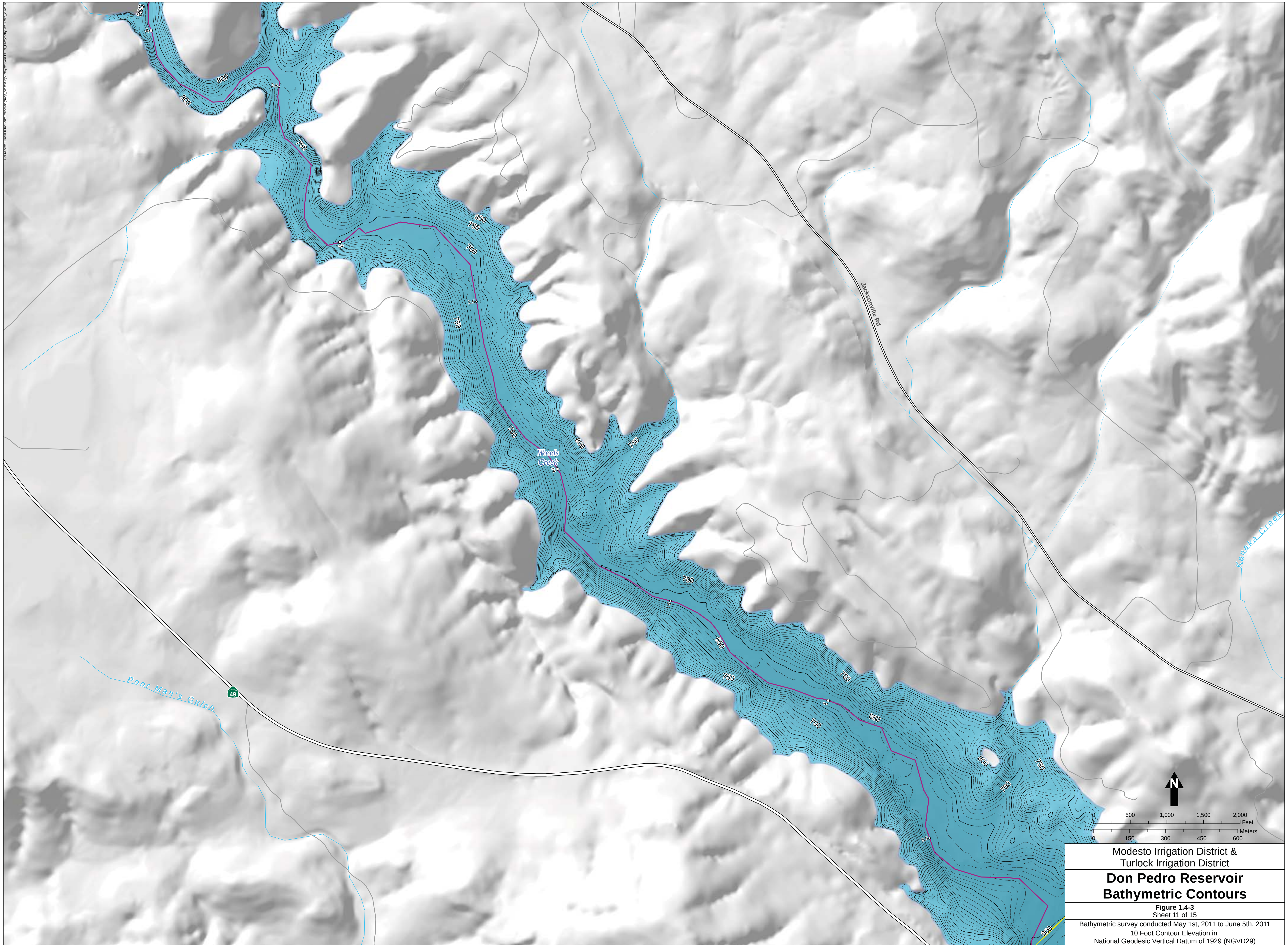

Modesto Irrigation District &
Turlock Irrigation District

Don Pedro Reservoir
Bathymetric Contours

Figure 1.4-3
Sheet 11 of 15

Bathymetric survey conducted May 1st, 2011 to June 5th, 2011
10 Foot Contour Elevation in
National Geodesic Vertical Datum of 1929 (NGVD29)
Prepared by: HDR Engineering Inc.

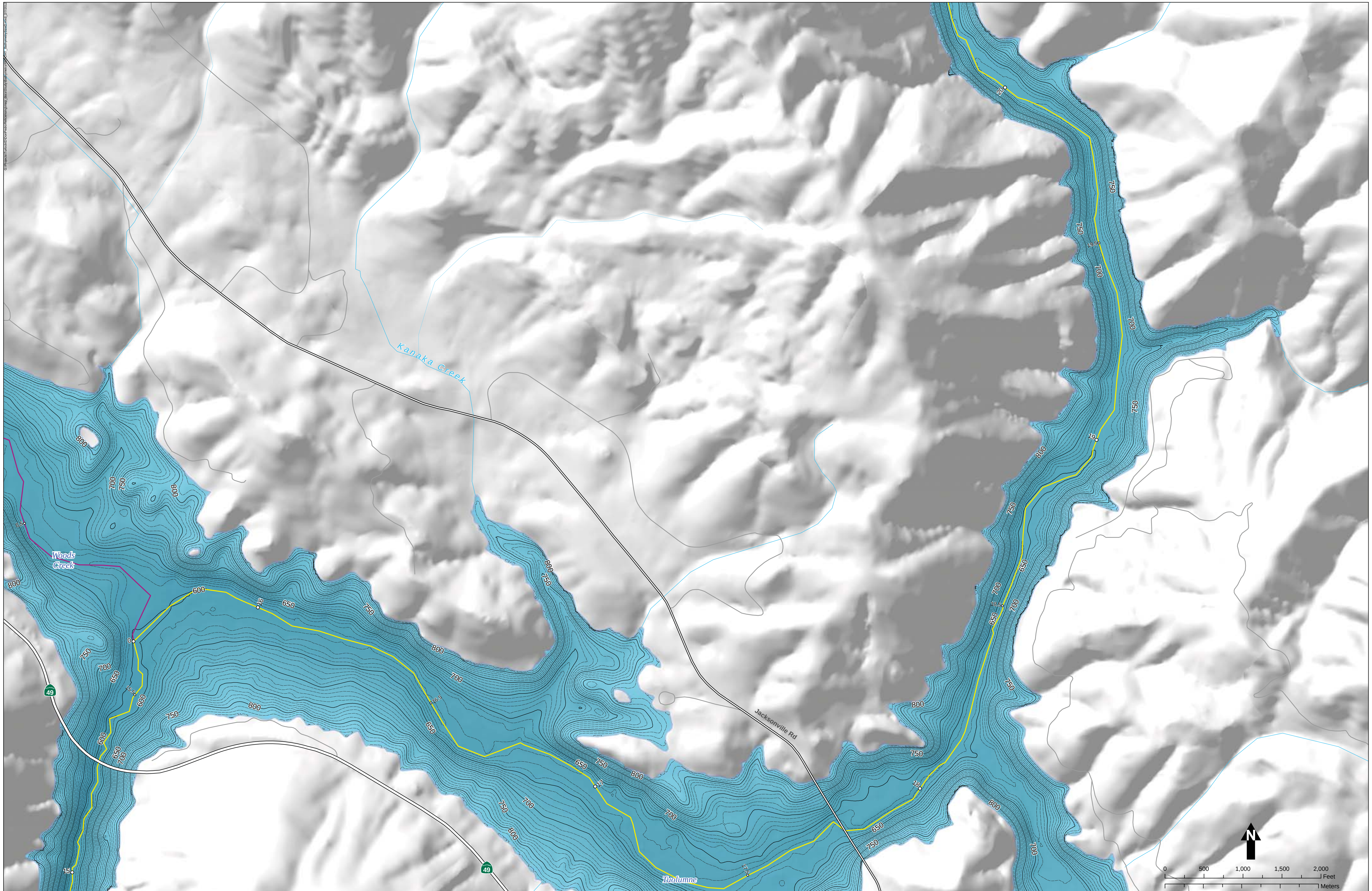

Modesto Irrigation District &
Turlock Irrigation District

Don Pedro Reservoir
Bathymetric Contours

Figure 1.4-3
Sheet 12 of 15

Bathymetric survey conducted May 1st, 2011 to June 5th, 2011
10 Foot Contour Elevation in
National Geodesic Vertical Datum of 1929 (NGVD29)
Prepared by: HDR Engineering Inc.

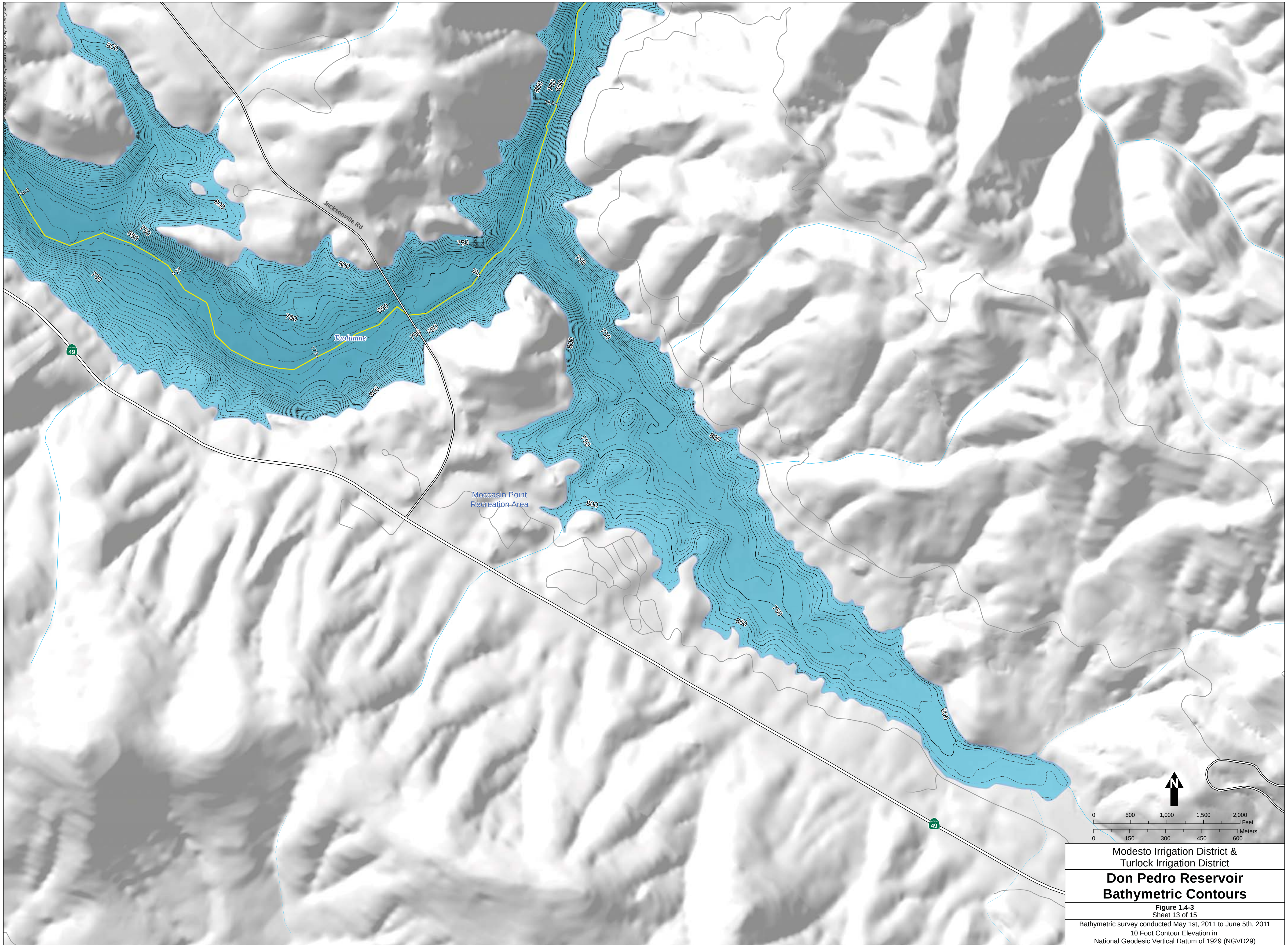

Modesto Irrigation District &
Turlock Irrigation District

Don Pedro Reservoir
Bathymetric Contours

Figure 1.4-3
Sheet 13 of 15

Bathymetric survey conducted May 1st, 2011 to June 5th, 2011
10 Foot Contour Elevation in
National Geodesic Vertical Datum of 1929 (NGVD29)
Prepared by: HDR Engineering Inc.

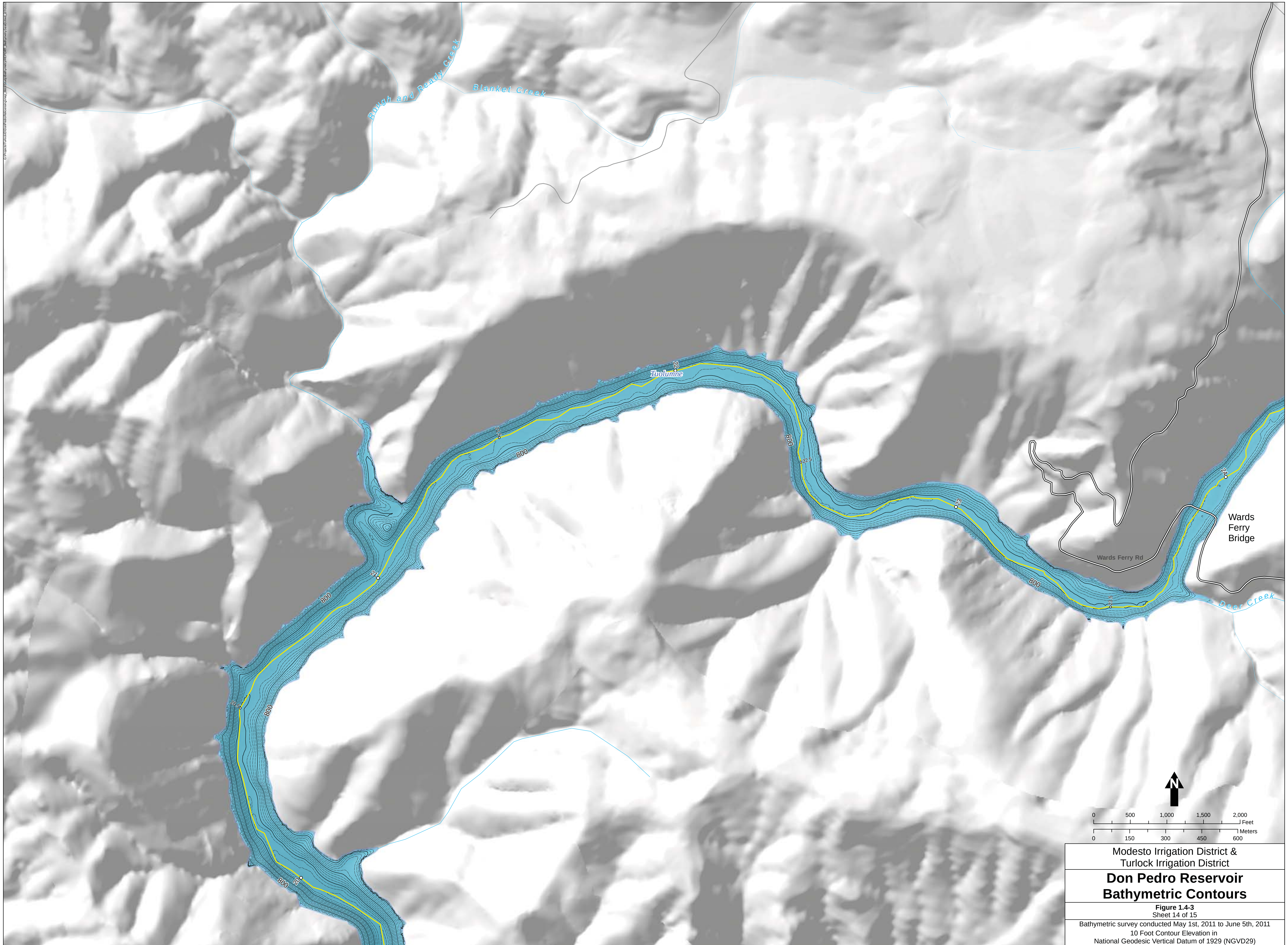

Modesto Irrigation District &
Turlock Irrigation District

Don Pedro Reservoir
Bathymetric Contours

Figure 1.4-3
Sheet 14 of 15

Bathymetric survey conducted May 1st, 2011 to June 5th, 2011
10 Foot Contour Elevation in
National Geodesic Vertical Datum of 1929 (NGVD29)
Prepared by: HDR Engineering Inc.

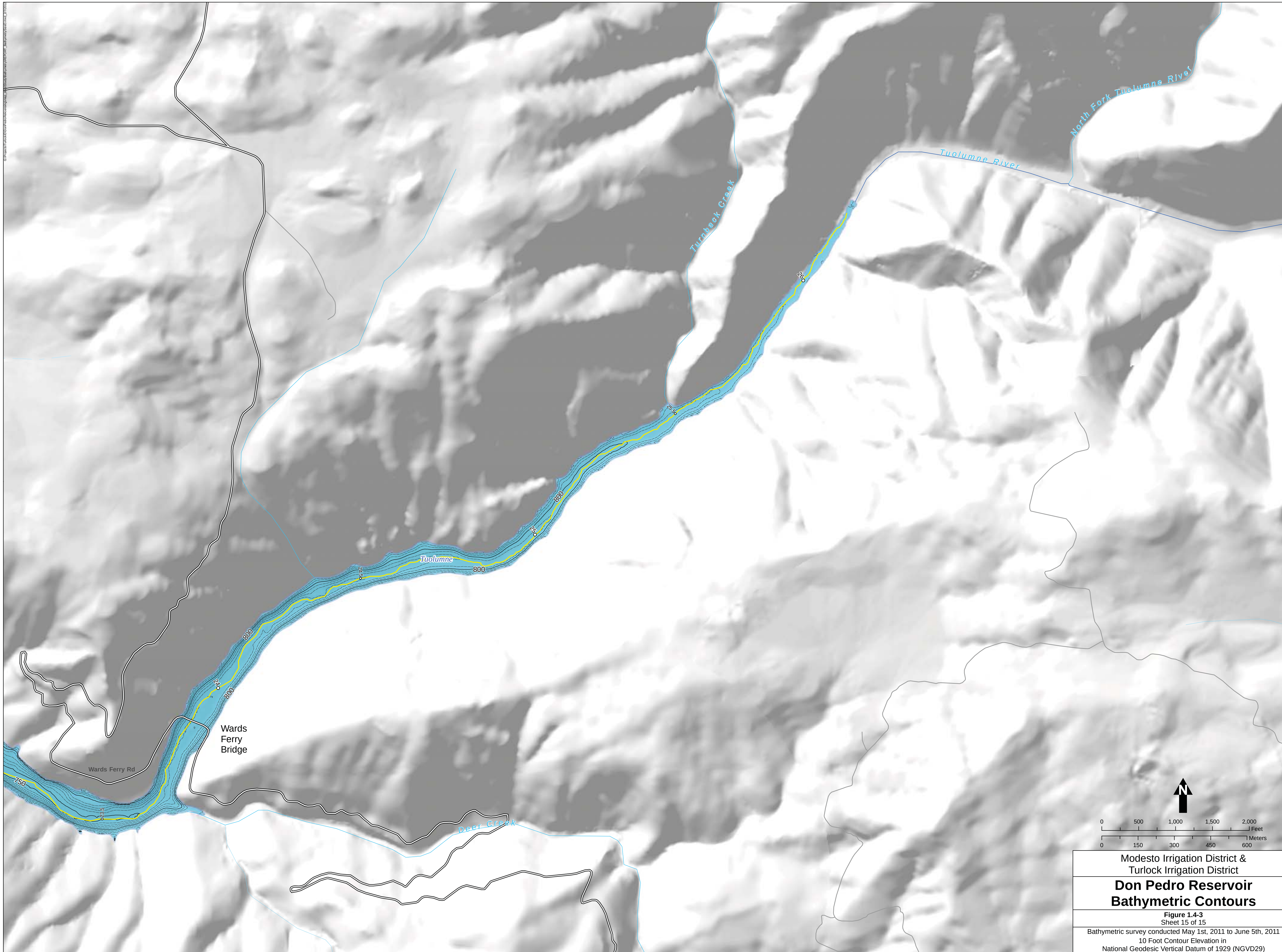

Modesto Irrigation District &
Turlock Irrigation District

Don Pedro Reservoir
Bathymetric Contours

Figure 1.4-3
Sheet 15 of 15

Bathymetric survey conducted May 1st, 2011 to June 5th, 2011
10 Foot Contour Elevation in
National Geodesic Vertical Datum of 1929 (NGVD29)
Prepared by: HDR Engineering Inc.

STUDY REPORT W&AR-03
RESERVOIR TEMPERATURE MODEL

ATTACHMENT D

WATER TEMPERATURE AND LOCAL METEOROLOGY DATA SET
(May 2013)

Due to the size and format of the material in Study W&AR-03 Attachment D, copies of the material may be obtained upon request to the Districts. Please contact John Devine, Relicensing Project Manager, at 207.775.4495 or by e-mail at john.devine@hdrinc.com.

This Page Intentionally Left Blank.

STUDY REPORT W&AR-03
DON PEDRO RESEVOIR TEMPERATURE MODEL

ATTACHMENT E

FULL PERIOD OF RECORD METEOROLOGICAL DATA SET

This Page Intentionally Left Blank.

TABLE OF CONTENTS

Section No.	Description	Page No.
1.0	INTRODUCTION	1-1
2.0	data requirements	2-1
3.0	data sources	3-1
4.0	Full period of record data set development	4-1
4.1	Reservoir Temperature Model Temperature Data Set	4-1
4.2	Lower Tuolumne Temperature Model Data Set	4-3
5.0	References	5-1

List of Figures

Figure No.	Description	Page No.
Figure 3.0-1.	Weather station locations.	3-3

List of Tables

Table No.	Description	Page No.
Table 3.0-1.	Weather stations.	3-1

1.0 INTRODUCTION

FERC approved the Districts' Don Pedro Reservoir Temperature Model Study Plan (W&AR-03) in its December 22, 2011 Study Plan Determination. The study includes the development of a three-dimensional (3-D) model of the reservoir's thermal conditions. One of the input requirements for the model is a hydrologic and meteorological data set for the full period of record to be evaluated by the model; that is, Water Year (WY) 1971 through WY 2012) (TID/MID 2011a). Likewise, application of the FERC-approved Lower Tuolumne River Temperature Model (W&AR-16) also requires a long-term meteorological data set (TID/MID 2011b).

This report provides a description of the development of the full period of record meteorological data set. The identification and analysis of the available historical data are described, as are the methods used to create the full period of record of input meteorology.

2.0 DATA REQUIREMENTS

The Reservoir Temperature Model employs a 3-D model platform, the Danish Hydraulic Institute (DHI) MIKE3-FM model, while the Lower Tuolumne River Temperature Model employs the US Army Corp of Engineers’ HEC-RAS platform (DHI 2011; ACOE 2010). The MIKE3 platform requires the following hourly meteorological input data:

- air temperature (°F),
- relative humidity (%),
- wind speed (mph),
- hourly wind direction (degrees), and
- clearness, 0 (cloudy) to 1 (clear).

MIKE3-FM calculates solar radiation from sun angle relationships and the clearness index.

The HEC-RAS platform requires hourly meteorological input data as well, consisting of the following parameters:

- air Temperature (°F),
- relative Humidity (°F),
- barometric Pressure (in Hg),
- short-wave solar radiation (watt-hours/ft^2/day), and
- wind speed (mph).

Development of the long term data set for each parameter is discussed below.

3.0 DATA SOURCES

The long term meteorological data set was derived from measured data at nearby weather stations operated by, or in cooperation with, the National Oceanic and Atmospheric Administration (NOAA, 2013) and the California Irrigation Management Information System (CIMIS). Solar radiation data were available at many of the NOAA sites.

Weather stations were identified that (1) were representative of the meteorology of each model area; (2) had the required data types; and (3) had either the full period of record or sufficient period of record to be useful as supplemental data. Table 3.0-1 provides a summary of the weather stations selected and Figure 3.0-1 shows the location of each gage.

Table 3.0-1. Weather stations.

Weather Station	Operating Agency	Period of Record[1]	Data Type[1]
Don Pedro	TID/MID	11/30/2010 to 12/31/2012	Air Temperature Relative Humidity Wind Speed Wind Direction Barometric Pressure Solar Radiation
Crocker Ranch	TID/MID	11/30/2010 to 12/31/2012	Air Temperature Relative Humidity Wind Speed Barometric Pressure Solar Radiation
Stockton Metropolitan Airport	NOAA[3], NREL[4]	10/1/1970 to 12/31/2012	Air Temperature Relative Humidity Wind Speed Barometric Pressure
Modesto City-County Airport	NOAA[3], NREL[4]	1/1/1973 to 12/31/2012	Air Temperature Relative Humidity Wind Speed Barometric Pressure Modeled Solar Radiation
Castle Air Force Base	NOAA[3], NREL[4]	1/1/1973 to 12/31/2012	Air Temperature Relative Humidity Wind Speed Barometric Pressure
Modesto	CIMIS[2]	1/1/2010 to 12/31/2012	Air Temperature Relative Humidity Wind Speed Barometric Pressure Solar Radiation
Denair II	CIMIS[2]	1/1/2010 to 12/31/2012	Solar Radiation
Oakdale	CIMIS[2]	1/1/2010 to 12/31/2012	Solar Radiation

Weather Station	Operating Agency	Period of Record[1]	Data Type[1]
Sacramento Executive Airport	NOAA[3], NREL[4]	10/1/1970 to 12/31/1991	Modeled Solar Radiation

1 Only includes weather station data or date ranges used in the dataset creation.
2 CIMIS (2013)
3 NOAA (2013)
4 NREL (2013)

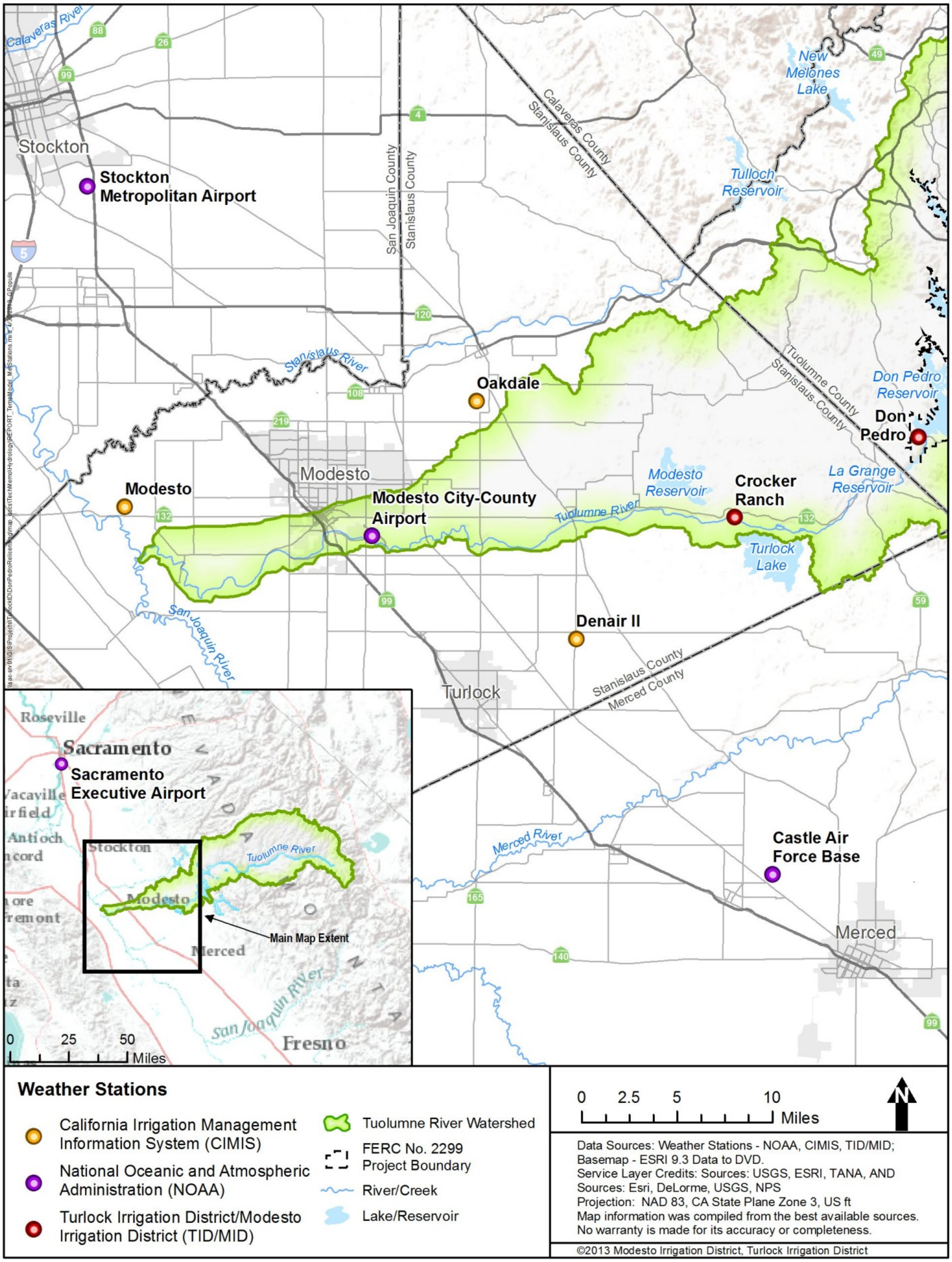

Figure 3.0-1. Weather station locations.

4.0 FULL PERIOD OF RECORD DATA SET DEVELOPMENT

Following extraction of data from the various sources (Section 3.0), data were verified and/or validated as appropriate. Air temperature, relative humidity, barometric pressure, and wind speed data were reviewed for completeness and accuracy. Visual inspection of the data using HEC-DSS was performed to identify and remove obvious data errors. For example, single hour "spikes" of an exceptional magnitude for each data type were removed. Linear interpolation was then used to fill in data gaps up to an appropriate maximum number of hours based on data set type and the level of variability within each data type.

It was observed that the NOAA Stockton Metropolitan Airport weather station data set was considerably more complete than the other weather station data sets. The NOAA Modesto City-County Airport weather station was the nearest weather station to the Don Pedro Project that contained the full period of record; however a large portion of the data was missing, including nighttime values for the majority of the recorded days. The Stockton Metropolitan Airport weather station data were compared to other weather stations in Table 3.0-1 and it was concluded that the Stockton Metropolitan Airport weather station data are sufficiently representative of the other gages for purposes of developing the long term meteorology.

To complete the full period of record data set using the Stockton Metropolitan Airport weather station data, remaining gaps in air temperature, relative humidity, barometric pressure, and wind speed data at the Stockton Metropolitan Airport weather station were filled in using data from the other weather stations.

Development of the full period of record clearness and wind direction data sets is discussed below in the MIKE3-FM model input data set development discussion (Section 4.1). Development of the full period of record solar radiation data set is discussed below in the HEC-RAS model input data set development discussion (Section 4.2).

The complete data set is available on CD upon request from John Devine at John.Devine@hdrinc.com.

4.1 Reservoir Temperature Model Temperature Data Set

The full period of record meteorological data set for input into the MIKE3-FM was developed to best represent conditions at the Districts' Don Pedro meteorological station. The data set was tested by running the MIKE3-FM model for 2011 and 2012 using inputs from the long term data set and comparing them to results of the model calibration and validation provided in the Reservoir Temperature Model Report (W&AR-03), to which this write-up is an attachment. As detailed further below, the resulting modeled water temperatures discharged from the reservoir using the 2011 and 2012 data from full period of record data set were very similar to those modeled during calibration and validation.

The air temperature and relative humidity data sets developed for the Stockton Metropolitan Airport weather station were direct inputs in the MIKE3-FM model. It was observed that the peak daily air temperatures observed at Stockton were representative of the peak air temperatures observed at the Districts' Don Pedro meteorological station. The nighttime air temperatures differed noticeably between the two data sets. The relative humidity data at Stockton followed the same diurnal patterns as observed at Don Pedro. Differences in magnitudes of the peak values were observed, but this is due primarily to the difference in nighttime temperatures when the relative humidity is the greatest.

The differences in temperature and relative humidity data sets were considered to be acceptable upon review of the 2011 to 2012 calibration and validation test results. The resulting modeled water temperatures discharged from the reservoir were very similar to those modeled during calibration and validation. It was observed that the peak daily air temperatures at Stockton were representative of the peak air temperatures observed at the Districts' Don Pedro meteorological station. The nighttime air temperatures differed noticeably between the two data sets, when relative humidity was the greatest.

The relative humidity data at Stockton followed the same diurnal patterns as observed at Don Pedro. Differences in magnitudes of the peak values were observed, but this is due primarily to the difference in nighttime temperatures. The differences in temperature and relative humidity data sets were considered to be acceptable upon review of the 2011 to 2012 calibration and validation test results as described above.

Review of the average wind speed at the Districts' Don Pedro meteorological station showed that it was nearly twice that recorded at Stockton. Hence, wind speed data at the Stockton Metropolitan Airport weather station were modified using linear regression techniques to better represent the wind conditions at Don Pedro. The linear regression analysis employed modified regression coefficients that were calculated so the resulting long-term data set had the same mean values and standard deviation as the Don Pedro weather station. This approach was chosen due to the fact that a strong correlation is not possible due to the inherent variability of measured instantaneous wind speeds. The method chosen produced a data set that adequately captured the peak wind events and the hourly variability of wind speeds.

A relationship between wind direction at the Stockton Metropolitan Airport and the Don Pedro weather station could not be developed because wind direction is a highly localized parameter, especially in locations with varying terrain as typical of the Sierra foothills. Instead, it was deemed more important to capture the local conditions at the Don Pedro weather station, despite only having two years of recorded data. Don Pedro station wind direction data were examined in HEC-DSS using a cyclic analysis, which overlays the statistical average and percentiles of wind direction, in order to describe the variability in the data set. A diurnal pattern to wind direction emerged by this analysis, and it was also observed that May, June, and July exhibited a different pattern than the remainder of the year. Thus, a synthetic data set was created for Oct 1971 to Dec 31st 2012 based on the median hourly wind direction for May through July, and median hourly wind direction for August through April.

The clearness of the sky is related to the cloud cover. Daily cloud cover data for either Don Pedro Reservoir or Modesto is not available; however, monthly data are. Monthly average clearness was obtained from weatherspark.com which compiles data from NOAA's National

Weather Service - Aviation Weather Center, which includes the Modesto City-County Airport. The comparison of computed and measured solar radiation is presented in Section 4.4. 6.6 Short Wave Radiation of the Reservoir Model Report (W&AR-03), to which this write-up is attached.

4.2 Lower Tuolumne Temperature Model Data Set

The full period of record meteorological data set for input into the HEC-RAS model was developed to best represent conditions at the Districts' Crocker Ranch weather station. The data set was tested by running the HEC-RAS model for 2011 and 2012 using inputs from the long term data set and comparing them to results of the model calibration and validation provided in the Reservoir Temperature Model Report (W&AR-03), to which this write-up is an attachment. As detailed further below, the resulting modeled 2011 and 2012 water temperatures within the Tuolumne River were very similar to those modeled during calibration and validation.

The full period of record air temperature and relative humidity data developed for the Stockton Metropolitan Airport weather station were direct inputs into Lower Tuolumne River Temperature Model as they were representative of the conditions at the Districts' Crocker Ranch weather station.

Wind speed data at the Stockton Metropolitan Airport weather station were modified to better represent the wind conditions at the Districts' Crocker Ranch weather station using linear regression. Modified regression coefficients were applied so the resulting data set had the same mean values and standard deviation as the Crocker Ranch weather station. This approach was chosen because a strong correlation is not possible due to the inherent variability of measured instantaneous wind speeds. This method produced a data set that adequately captured the peak wind events and the hourly variability of wind speeds.

The primary source of hourly solar radiation data came from modeled data from the National Solar Radiation Database (NSRDB) developed by the NREL (NREL 2013), a laboratory of the United States Department of Energy. The NRSDB consists of two models; solar radiation from 1961 to 1990, and solar radiation from 1991 to 2010. The 1991 to 2010 database was developed based upon updated methods and techniques and benefits from plentiful solar radiation data.

Sacramento Executive Airport weather station was the closest weather station modeled by NREL for the 1961 to 1991 period. A strong correlation was observed during the overlapping period of record, 1987 to 1991, between the measured solar radiation at the Modesto CIMIS weather station and the NREL modeled solar radiation data. Hourly modeled Sacramento Executive Airport solar radiation data were used in the full period of record data set for Oct 1, 1970 to Dec 31st, 1990.

The 1991 to 2010 database included the Modesto City-County Airport, the Stockton Metropolitan Airport, and Castle Air Force Base near Atwater, California. The Modesto City-County Airport modeled solar radiation data were used in the full period of record data set from 1991 to 2010. The Modesto City-County Airport was selected as it is the closest weather station to the project.

For 2010 through 2012, the Oakdale CIMIS station solar radiation data were the primary source with missing data filled in using the Denair II CIMIS and Modesto CIMIS weather stations.

5.0 REFERENCES

California Irrigation Management Information System (CIMIS). 2013, California Department of Water Resources. Data available online: <www.cimis.water.ca.gov>. Accessed February, 2013.

Danish Hydraulic Institute (DHI). 2011. MIKE 21 and MIKE 3 Flow Model FM, Hydrodynamic and Transport Module, Scientific Documentation.

National Oceanic and Atmospheric Administration (NOAA). 2013. US department of Commerce. Data available online: <www.climate.gov>. Accessed February 2013.

National Renewable Energy Laboratory (NREL). 2013. U.S. Department of Energy. Available online: < http://rredc.nrel.gov/solar/old_data/nsrdb/>. Accessed February, 2013.

Turlock Irrigation District and Modesto Irrigation District (TID/MID). 2011a. Reservoir Temperature Model Study Plan (W&AR-03). Attachment to Don Pedro Hydroelectric Project Revised Study Plan. November 2011.

_____. 2011b. Lower Tuolumne River Temperature Model Study Plan (W&AR-16). Attachment to Don Pedro Hydroelectric Project Revised Study Plan. November 2011.

US Army Corp of Engineers. 2010. HEC-RAS, River Analysis System Users Manual , Version 4.1. January 2010.

STUDY REPORT W&AR-03
RESEVOIR TEMPERATURE MODEL

ATTACHMENT F

FULL PERIOD OF RECORD INFLOW TEMPERATURE DATA SET

This Page Intentionally Left Blank.

1.0 OBJECTIVE

FERC approved the Districts' Don Pedro Reservoir Temperature Model Study Plan (W&AR-03) in its December 22, 2011 Study Plan Determination. The study includes the development of a three-dimensional (3-D) model of the reservoir's thermal conditions. One of the input requirements for the model is an inflow temperature data set for the full period of record to be evaluated by the model: that is, Water Year (WY) 1971 through WY 2012 (TID/MID 2011a).

Available stream temperature data measured from flowing water upstream, within, and downstream of the Project are available in electronic format as Attachment C of this report. The objective of the analysis described in the following sections is to develop a method for predicting average daily water temperature in the upper Tuolumne River when observed water temperature data are unavailable.

2.0 ANALYSIS

The water temperature in the main stem Tuolumne River just below the South Fork confluence (CDFG Station TBSFRK) was selected to be representative of reaches downstream to the Don Pedro Reservoir (Figure 1). Water temperature data for the Tuolumne River below the South Fork (TBSFRK, RM 96.5; 37.8361 °N, 120.0537 °S) was obtained from the California Department of Fish and Game (CDFG). The period of record extends from April 27, 2007 through the present.

An obvious feature of the TBSFRK water temperatures is the annual cycle of high summer temperatures followed by low winter temperatures (Figure 2). This suggests that a cyclical function based on 2πDOY/365.25, where DOY is the day of the year, would be useful in constructing a predictive regression model. A wide range of meteorological, geomorphic and hydraulic factors may influence water temperatures at a given point in a stream. In an effort to include the meteorological effects the following data were obtained from Buck Meadows (*BuckMeadows-daily.xlsx,* a daily worksheet attached to the Operations Model Report (W&AR-02)(TID/MID 2013)):

- solar radiation
- wind speed
- wind direction
- wind gust speed
- average daily air temperature
- maximum daily air temperature
- minimum daily air temperature
- average daily relative humidity
- maximum daily relative humidity
- minimum daily relative humidity
- total daily precipitation

These parameters were evaluated as independent variables in the regression models. Several additional sources of average daily air temperature were available, but they were generally less complete than the Buck Meadows record and were very highly correlated with Buck Meadows; consequently, only the Buck Meadows records were used in the final models. Independent variables representing hydraulic effects included in the analysis were: Total Flow into Don Pedro, Unregulated Flow, Regulated Flow (downstream from Hetch Hetchy, Cherry Lake and Lake Eleanor reservoirs), and South Fork Tuolumne River Flow (assumed to be 37% of the Unregulated flow based on proportional drainage basin area). The computed flow values were obtained from the Don Pedro *Unimpaired and Other Flow Data Version 1(added data 9-27-2012).xlsx*, Data worksheet, Column AU (Provided as an attachment to the Operations Model Report (W&AR-02)(TID/MID 2013)).

Multiple regression analysis using Huber's Method for robust fit was used to obtain the least squares fit for the equation having the general from:

$$T_{TBSFRK} = \propto + \beta_1 Sin(B) + \ \beta_2 Cos(B) + \beta_3 x + . \cdots + \ \beta_n$$

where TBSFRK is the average daily water temperature. Various variable selection algorithms, including forward stepwise, backward stepwise, and all possible regressions (NCSS 2007), were used to select the independent variables used for the final model. Most putative independent variables were entered in an untransformed (x) state, but were also entered with the following transformations: $y^{0.5}$, y^2, ln(y), 1/y, $1/y^{0.5}$, $1/y^2$. Additionally, cubic terms and interaction terms were also explored for most variables. After the transformations and variable selection process, the "best" model was (Table 1):

$$TBSFRK_{Temp} = 15.8250 - 0.7992 \text{ x } \ln(Q_{Total}) - 1.9413 \text{ x } \sin(B) - 3.5872 \text{ x } \cos(B)$$

where B = 2π x DOY / 365.25; DOY = day of year, i.e., 1 through 365 with January 1 = 1.

Table 1. Regression Coefficients for TSFRK Model (Original)

Independent Variable	Regression Coefficient b(i)	Standard Error Sb(i)	T-Value To Test H0:B(i)=0	Probability Level	Reject H0 at 5%?	Power of Test at 5%
Intercept	7.0008	0.2182	32.078	0.0000	Yes	1.0000
AT_{t-1}	0.4184	0.0095	44.196	0.0000	Yes	1.0000
Cos_B	-2.8973	0.0923	-31.381	0.0000	Yes	1.0000
Ln_Q_{TSFRK}	-0.2766	0.0328	-8.437	0.0000	Yes	1.0000
Sin_B	-2.0898	0.0719	-29.084	0.0000	Yes	1.0000
R^2 = 0.9391; RMSE = 1.380687; n = 1683						

Note that the lagged air temperature was not significant in this relationship and was, therefore, dropped.

The values predicted by the multiple regression model are shown in Figure 3. Overall, the model is reasonably accurate, with approximately 80% of the predictions within ±1.7 °C of the observed value and precise, explaining approximately 85% of the total variance.

Despite the relative good fit of the multiple regression model, the distribution of the residuals is of some concern. There appears to be a systematic under-prediction of high temperatures during late summer /fall and a systematic over-prediction of low winter temperatures (Figure 4). A more detailed investigation of the distribution of observed water temperatures by month indicates an unusual, often bimodal, pattern (Appendix A). During December through March, the temperature distributions tend to be skewed to the left while the July through October distributions are bimodal and skewed to the right. The temperatures during the remaining months (April, May, June and November), are relatively normally distributed. Under typical circumstances, water temperatures should be approximately normally distributed throughout the year. The bimodality and skewness suggests an artificial situation likely brought about by the seasonal mixing of reservoir release water mixing with unregulated surfaces waters from the South Fork Tuolumne River. Temperatures from the unregulated South Fork (measured at TSFRK) fluctuate widely, reaching a maximum average of approximately 20°C in the summer and a minimum average of approximately 3.5°C in the winter (Figure 5; Appendix B). Regulated waters (measured at TRSFRK), on the other hand, are primarily from the bottom layers of the Hetch Hetchy, Cherry Lake and Lake Eleanor reservoirs. These waters tend to be much more constant in temperature with maximum summer averages of approximately 15°C and with minimum winter averages of 7°C. Stream flows are approximately equal from both sources from September through April, but during the summer regulated flows greatly exceed unregulated flows (Figure 6). This mixing of the different temperature waters in proportions determined by the amount of water released from the reservoirs, can easily determine the mixtures of right skew, left skew, bimodality, and normality seen in the histograms. A similar pattern can be seen at regulated TRSFRK, but to a much lesser extent at the unregulated TSFRK (Appendix C and Appendix D) Under these circumstances, a prediction based a flow weighted temperature from both regulated and unregulated waters will likely prove more useful than a simple model based on average TBSFRK data.

To construct the flow weighted prediction model, separate regression models were constructed for the unregulated South Fork Tuolumne River (CDFG TSFRK) and for the regulated mainstem Tuolumne River above the South Fork (CDFG TRSFRK). The same procedures used for developing the TBSFRK regression model were applied to the TSFRK and TRSFRK data sets. Results are presented below (Table 2 and Table 3).

$$TRSFRK_{Temp} = 11.4226 - 0.4624 \times \ln(Q_{Regulated}) - 1.3321 \times \sin(B) - 1.7947 \times \cos(B) + 0.1613 \times AT_{t-1}$$

$$TSFRK_{Temp} = 7.0008 - 0.2766 \times \ln(Q_{TSFRK}) - 2.0898 \times \sin(B) - 2.8973 \times \cos(B) + 0.4184 \times AT_{t-1}$$

Note: QTSFRK = 0.37 × $Q_{Unregulated}$. The 0.37 value represents the proportional size of the TSFRK drainage basin.

Table 2. Regression Coefficients for TSFRK Model

Independent Variable	Regression Coefficient b(i)	Standard Error Sb(i)	T-Value To Test H0:B(i)=0	Probability Level	Reject H_0 at 5%?	Power of Test at 5%
Intercept	2.9156	0.1814	16.075	0.0000	Yes	1.0000
AT_{t-1} (Average)	0.4903	0.0109	45.099	0.0000	Yes	1.0000
Cos_B	-3.0543	0.0971	-31.452	0.0000	Yes	1.0000
Ln_Q_{UnReg}	-0.0002	0.0000	-8.980	0.0000	Yes	1.0000
Sin_B	-2.1931	0.0615	-35.655	0.0000	Yes	1.0000

R^2 = 0.9310; RMSE = 1.51365; n = 2355

Table 3. Regression Coefficients for TRSFRK Model

Independent Variable	Regression Coefficient b(i)	Standard Error Sb(i)	T-Value To Test H0:B(i)=0	Probability Level	Reject H_0 at 5%?	Power of Test at 5%
Intercept	4.2008	0.2231	18.829	0.0000	Yes	1.0000
AT_{t-1} (Maximum)	0.2774	0.0090	30.709	0.0000	Yes	1.0000
Cos_B	-4.1797	0.1031	-40.549	0.0000	Yes	1.0000
Ln_Q_{UnReg}	-0.0001	0.0000	-3.323	0.0009	Yes	0.9135
Sin_B	-2.7806	0.0667	-41.676	0.0000	Yes	1.0000

R^2 = 0.9102; RMSE = 1.73721; n = 2355

Predictions for $TBSFRK_{Temp}$ are then obtained from the average separate regression predictions weighted by the proportional flow from the Regulated and Unregulated sources.

$$TBSFRK_{Temp} = \alpha \times TRSFRK_{Temp} + (1-\alpha) \times TSFRK_{Temp}, \text{ where } \alpha = Q_{Regulated} / (Q_{Regulated} + Q_{Unregulated}).$$

The flow weighted, combined regression fit, as measured by R^2, is nearly identical to the single TBSFRK model, 0.8468 versus 0.8484.

3.0 DISCUSSION AND RESULTS

For the Don Pedro Reservoir Temperature Model, the flow weighted model offers several important advantages over the single TBSFRK model:

(1) There is a somewhat better fit to the extreme values thereby improving the distribution of residuals. The single regression model yielded residuals (the difference between observed and model predicted values) with a range of 12.15 °C (-6.82 to 5.33 °C). By comparison, the flow weighted model yielded a range of 10.82 °C (-5.58 to 5.24 °C), a 10.9% reduction in the range. A plot of the cumulative frequency distribution of residuals (Figure 5) indicates that most of the improvement was in the lower temperatures. For both models, 80% of the predicted observations were within approximately 1.7 °C of the observed value.

(2) The flow weighted model is likely to be more accurate for estimating missing values. The skewed and bimodal distributions of the observed water temperatures downstream of the South Fork emphasize the importance of the temperature and volume of the water released from upstream reservoir operations. Despite repeated efforts to capture this effect in the single model regression, no practical method for incorporating spillage was found. As a result, reservoir operations are only implicitly incorporated through the observed average day-to-day downstream temperatures. The flow weighted model, on the other hand, explicitly incorporates the temperatures and flow composition. As dam operations may change in a substantial manner from day-to-day and are known, the flow weighted model can use the additional information directly rather than assume an average value to produce missing temperature estimates.

(3) The flow weighted model offers greater flexibility in that it can be used for addressing alternative operating scenarios. If alternative release schedules are to be explored, the single regression model cannot adjust for different release volumes; it can base predictions based only on the “average release”. The flow weighted model can use the hypothesized releases to producing estimates which are adjusted for the specified release flows.

Hence, the flow weighted model was used to fill in missing temperatures in the temperature monitoring record.

3.1 Comparison with Model Calibration and Validation Data Sets

As pointed out in Section 4.3.3 of the Reservoir Temperature Report, to which this document is an attachment, obtaining a complete inflow temperature dataset for calibration and validation was particularly challenging because the CCSF site, TR-8, and CDFG site, TRWARDS, are located within the reservoir at approximate elevation 785 ft and 763 ft respectively, and are often inundated. Hence, the Districts’ temperature station “Tuolumne River at Indian Creek Trail (ICT)” was installed in October 2010 to collect inflow temperatures for the calibration and validation of the model. ICT is located upstream of the North Fork Tuolumne River confluence at approximately 37.8839 °N, 120.1534 °S at approximately RM 88.3.

How the TSFRK station relates to the ICT monitoring station and what the differences says about the extent of warming between the two is discussed below. Originally, the comparison was planned for the period 2011 through 2012, the calibration and validation years. However at the time of this comparison, only data through June 14, 2012 were available from the Districts' thermistors and large periods of data were missing in both the TSFRK data set, as well. Since CCSF and UC Davis have previously measured temperatures at ICT, the period of comparison was expanded to the entire period of available data, April 26, 2009 through June 14, 2012 (See Attachment E and F).

Only days where temperatures were recorded at both TSFRK and ICT were compared. Average daily water temperatures were computed by averaging all readings within a day and monthly average temperatures were computed from the daily averages. No attempts were made to adjust for an unequal number of readings within a day or month. (These case were relatively rare and would have little influence due to the large number of samples overall). The daily difference in temperature was computed as: ICT – TSFRK.

As apparent in Figure 9, there is an obvious seasonal difference between the two stations. During the colder months, September through April, average water temperatures at ICT are about 1.1 to 2.9°C warmer than TSFRK. During the warmer months, however, temperatures at ICT were as low as 3.4°C cooler. It should be noted that the comparison between TSFRK and ICT stations highlights the difference between regulated and unregulated flow temperatures. The seasonal difference between these two sources has been noted before. To address the amount of warming within the river, a comparison between TBSFRK and ICT would be better.

A comparison of between TBSFRK and ICT reveals a pattern more consistent with a comparison of two regulated flow stations (Figure 10). While overall differences are considerably smaller, a seasonal pattern is still apparent. In all months, except December through February , downstream temperatures were warmer. The greatest difference occurs in July through September when ICT averaged 1.26 to 1.55°C warmer.

Overall the developed relationships are strong and should therefore provide a reliable long term data set for both incoming flow and temperature for use in the Don Pedro Reservoir Model.

3.2 Inflow Data Set Availability

The complete data set is available on CD upon request from John Devine at John.Devine@hdrinc.com.

4.0 REFERENCES

NCSS website. 2007. Statistical power and analysis software. www.ncss.com.

Turlock Irrigation District and Modesto Irrigation District (TID/MID). 2013. Project Operations/Water Balance Model Study Report (W&AR-02). Attachment to Don Pedro Hydroelectric Project Initial Study Report. January.

_____. 2011. Reservoir Temperature Model Study Plan (W&AR-03). Attachment to Don Pedro Hydroelectric Project Revised Study Plan. November 2011.

5.0 FIGURES

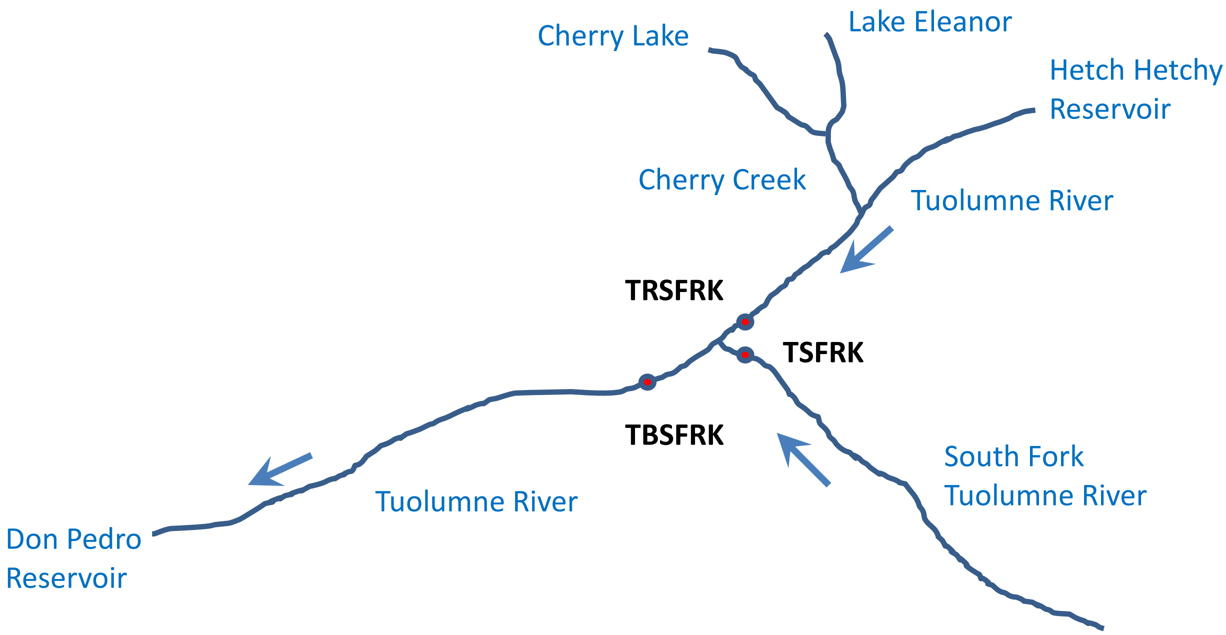

Figure 1. **Upper Tuolumne River Schematic showing Water Temperature Monitoring Locations.**

Stations:
CDFG TBSFRK - Tuolumne River below the South Fork (at RM 96.5); 37.8361 °N, 120.0537 °S; 4/27/2005 through present.
CDFG TSFRK - South Fork of the Tuolumne River near confluence; 37.8376 °N, 120.0473 °S; ; 4/27/2005 through present.
CDFG TRSFRK - Tuolumne River above the South Fork (at RM 97.1); 37.8403 °N, 120.0472 °S; 4/27/2005 through present.

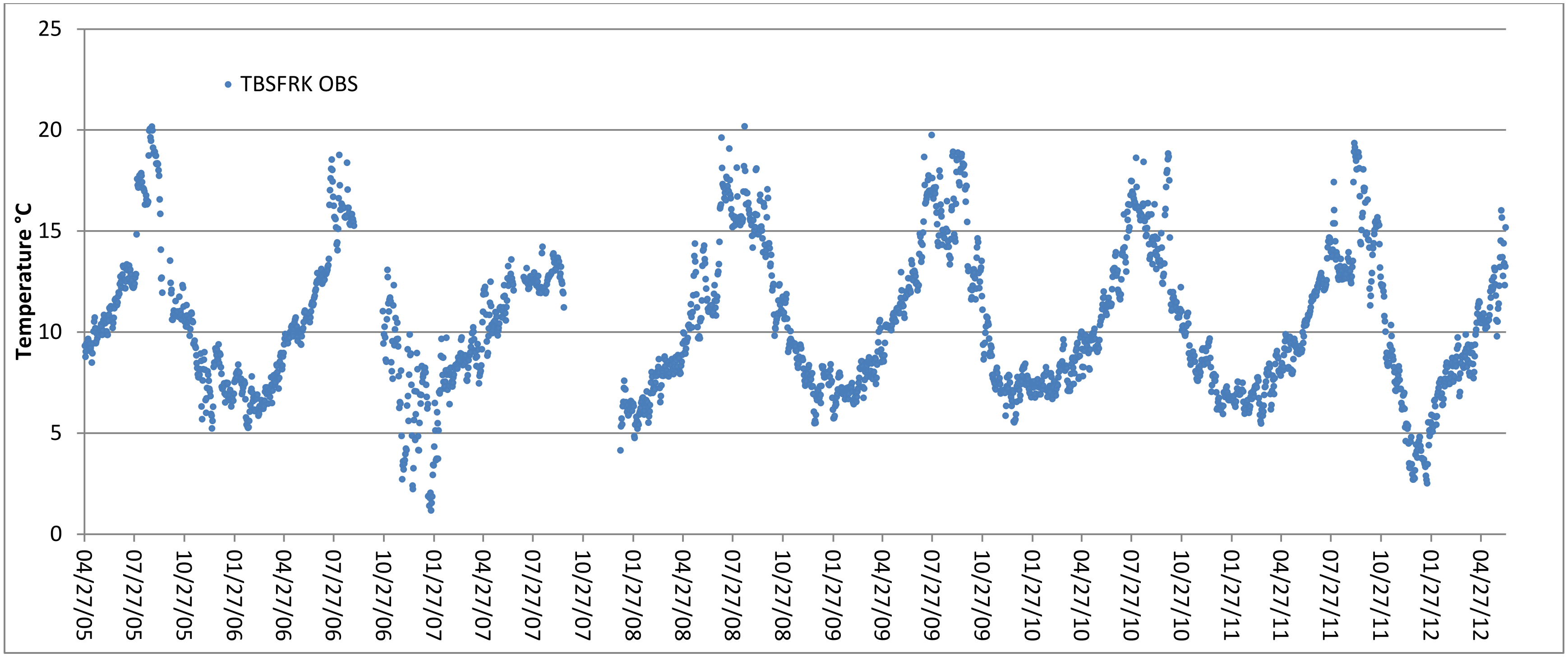

Figure 2. Observed Average Daily Water Temperature for CDFG Station TBSFRK during the period 4/27/05 through 6/14/2012.

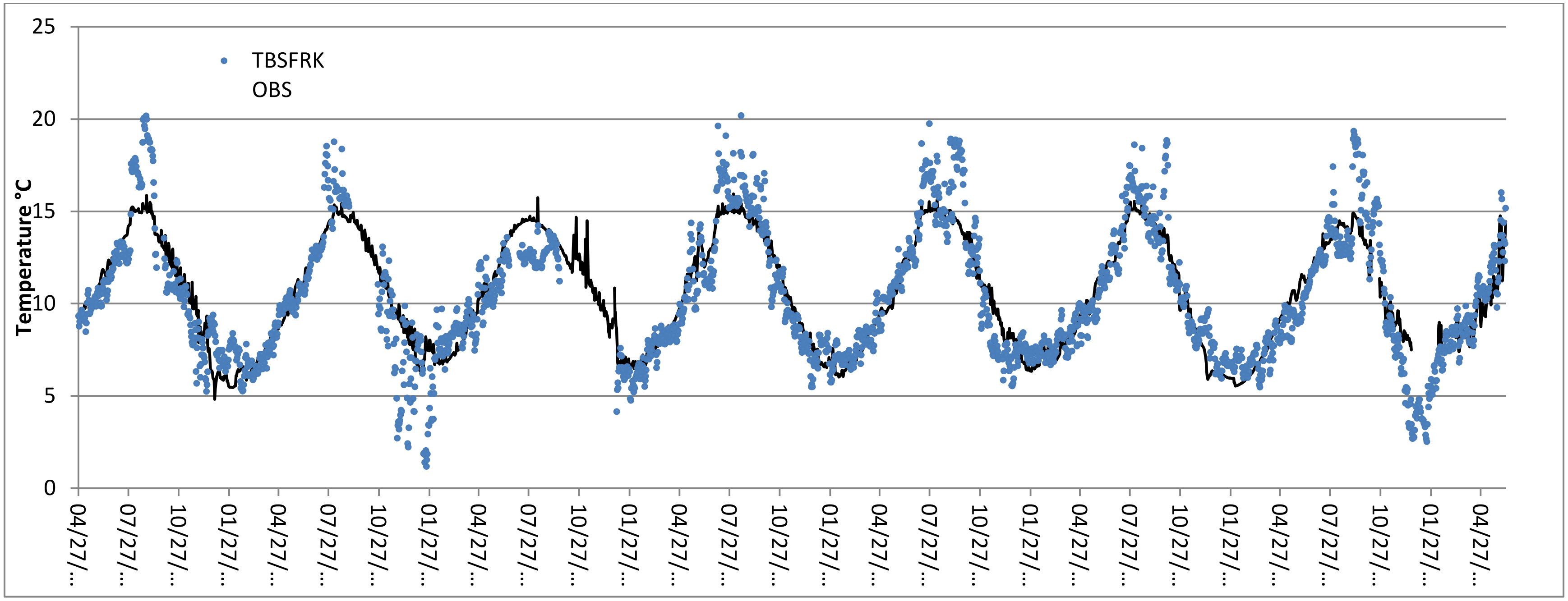

Figure 3. Observed Average Daily Water Temperature for CDFG Station TBSFRK for the period 4/27/05 through 6/14/2012 with regression model predictions.

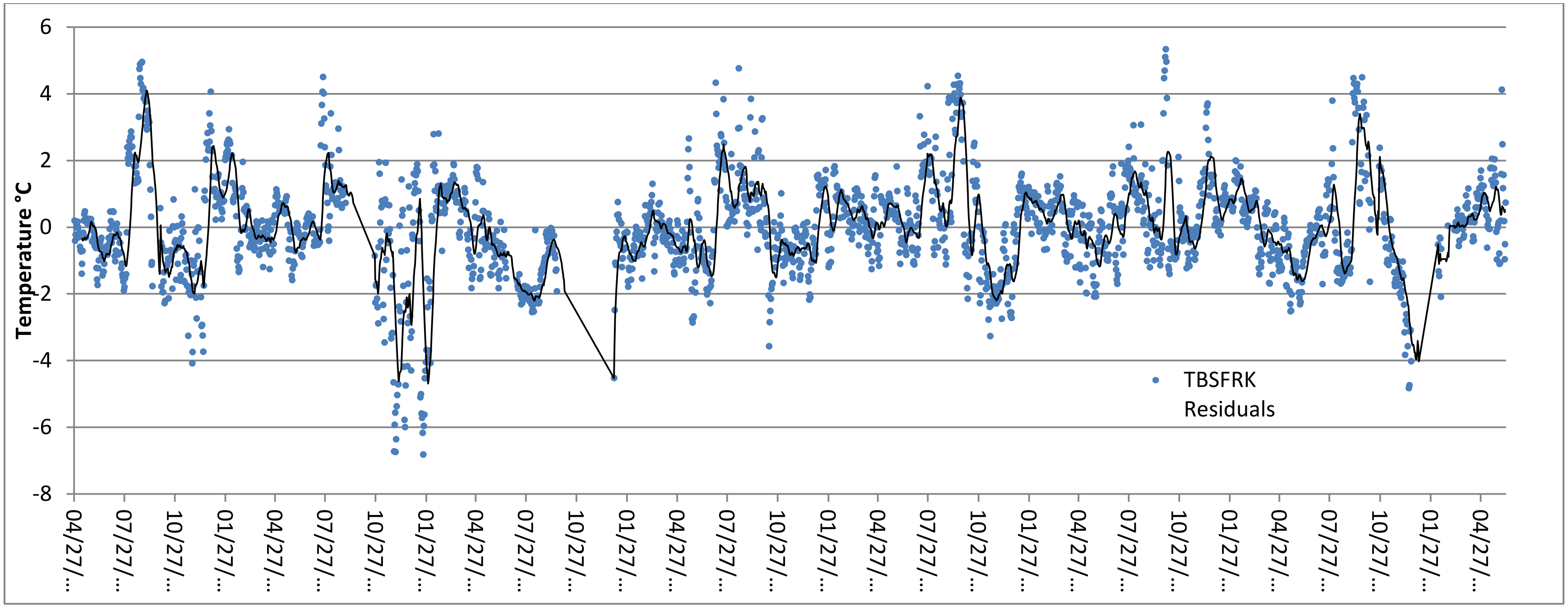

Figure 4. **Average Daily Water Temperature Residuals for CDFG Station TBSFRK for the period 4/27/05 through 6/14/2012.**

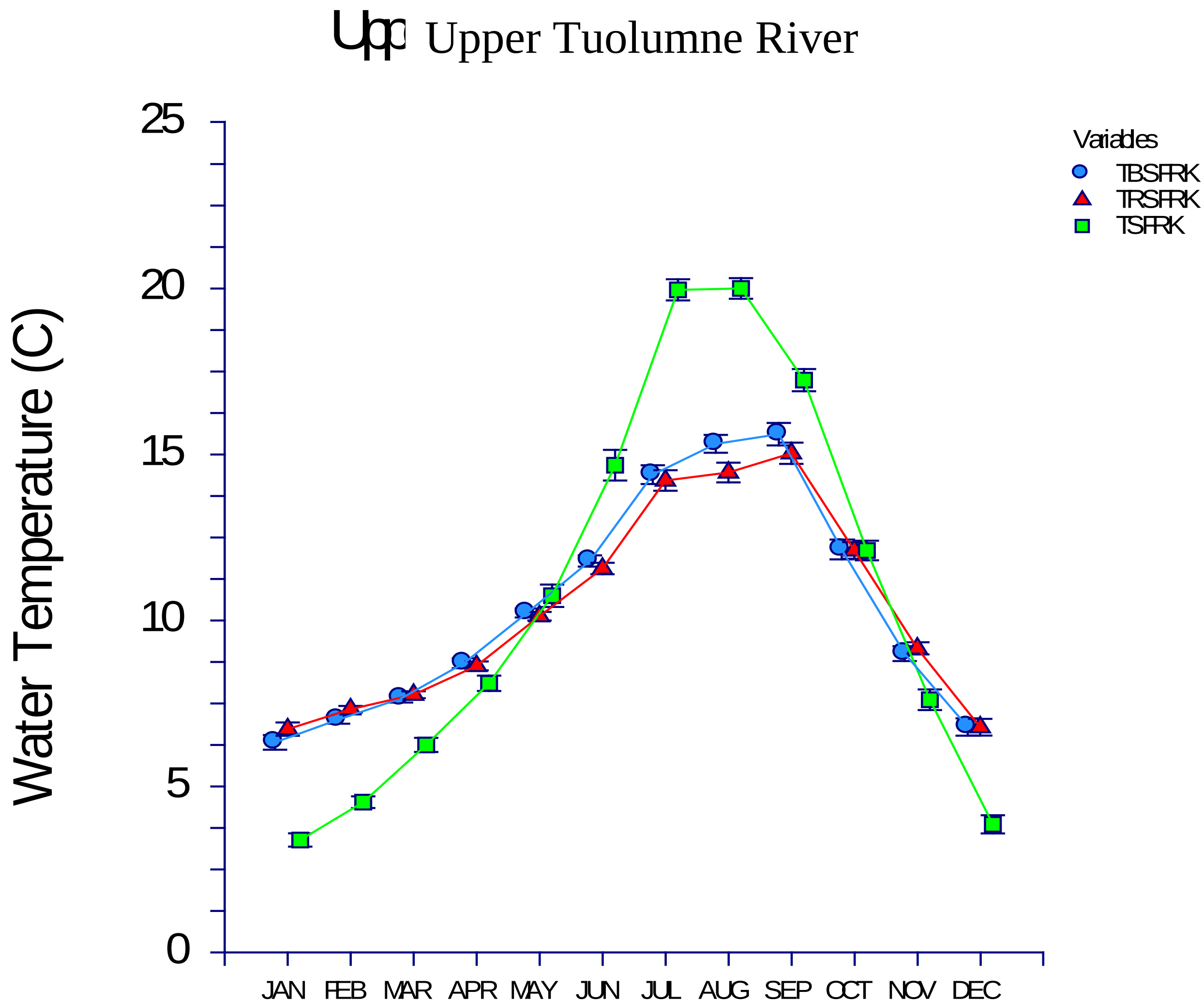

Figure 5. **Average Monthly Observed Water Temperatures by Monitoring Station. Vertical bars represent 95% Confidence Interval of Mean.**

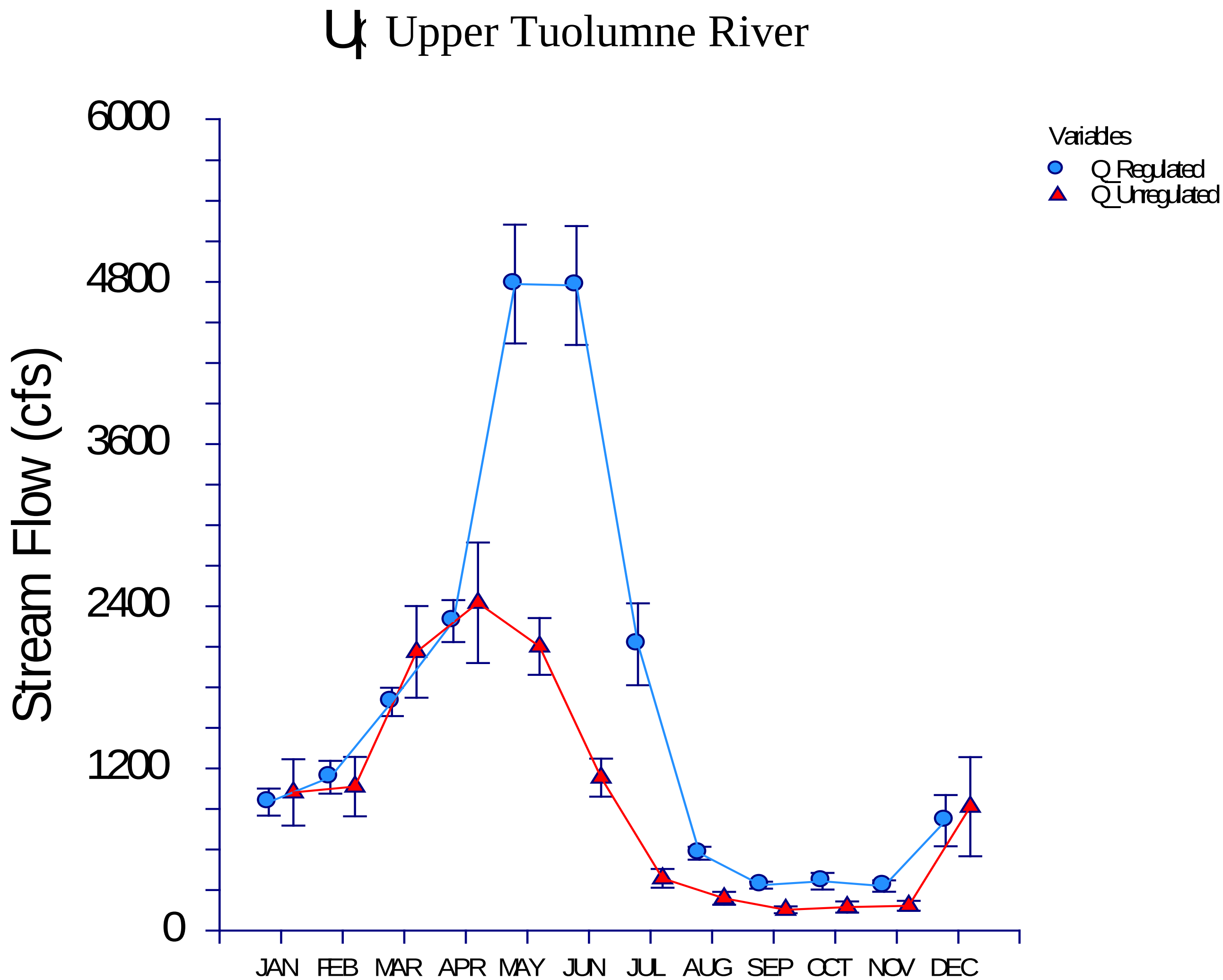

Figure 6. Average Monthly Observed Streamflow (Q) for Regulated and Unregulated Reaches of the Upper Tuolumne River. Vertical bars represent 95% Confidence Interval of Mean.

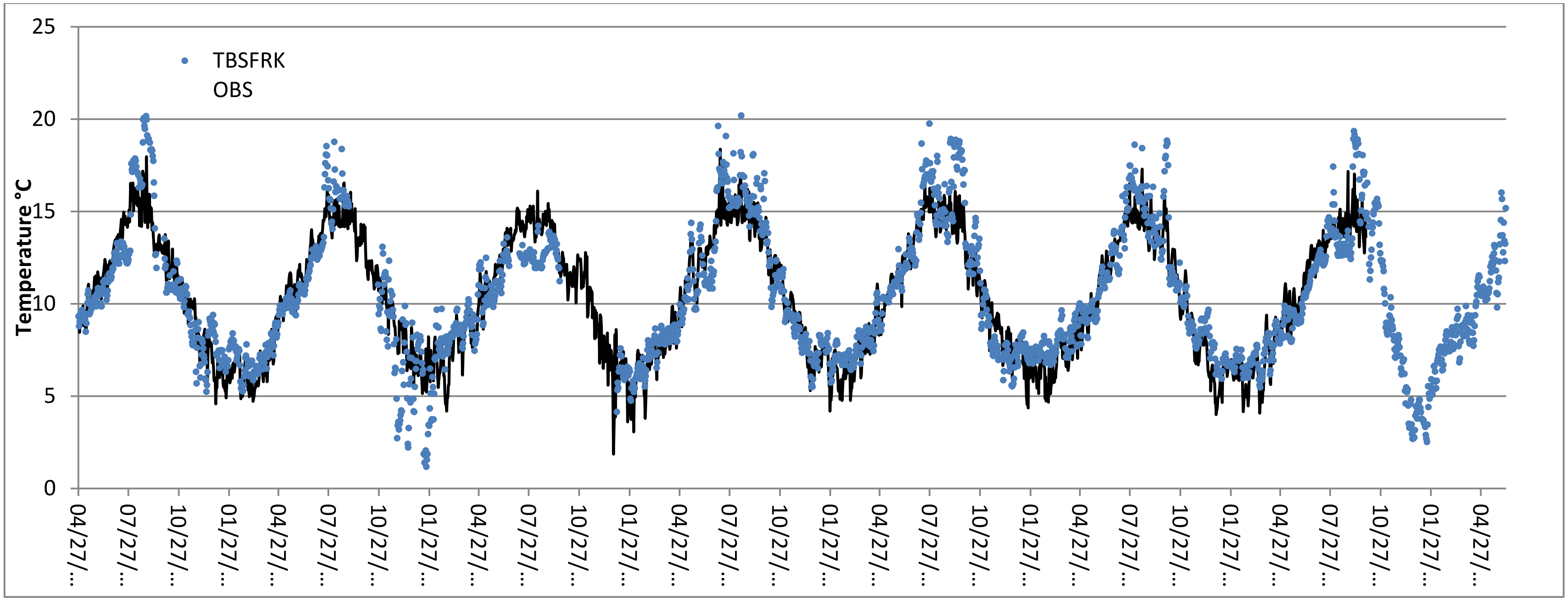

Figure 7. Observed Average Daily Water Temperature for CDFG Station TBSFRK for the period 4/27/05 through 6/14/2012 with flow weighted combined regression model predictions.

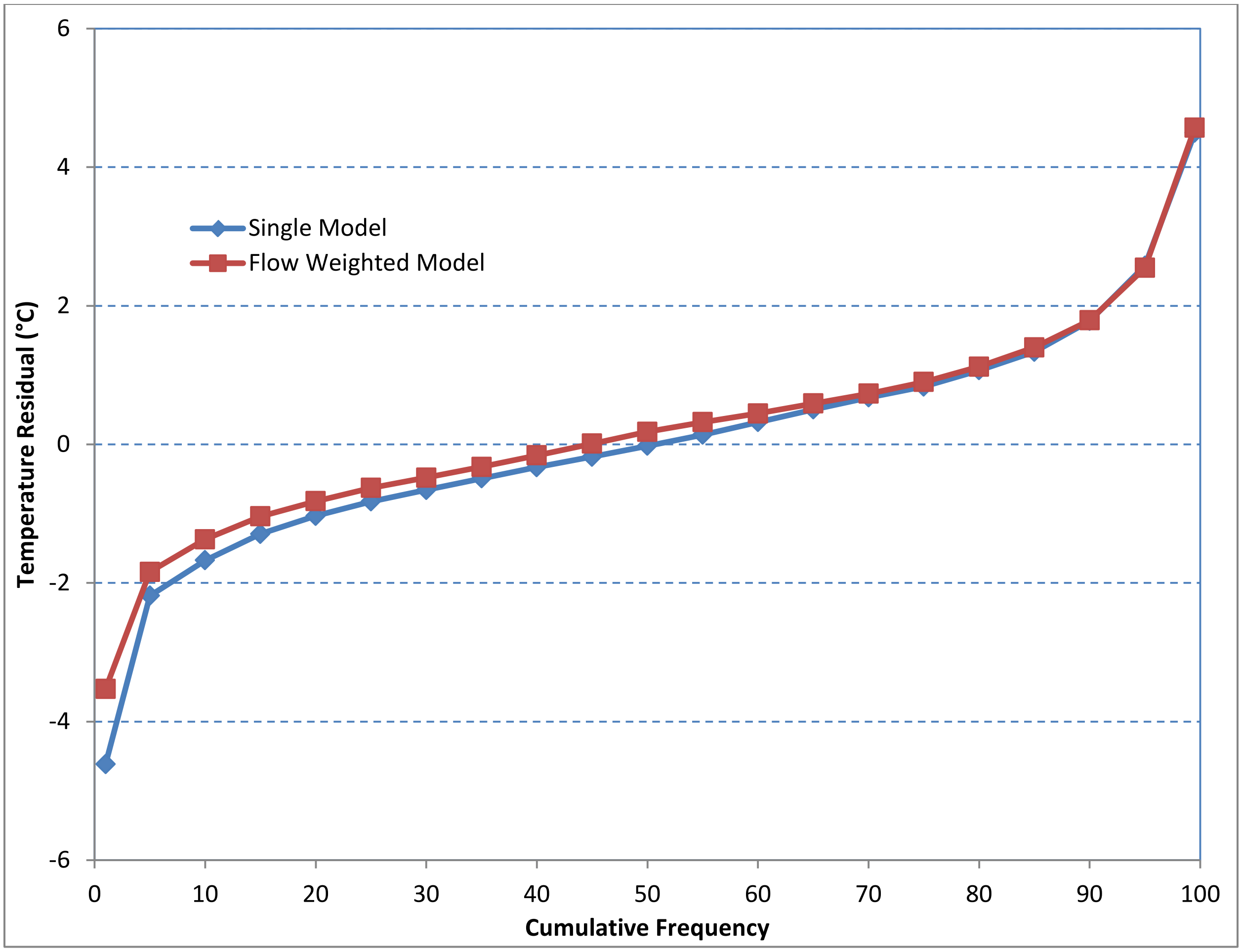

Figure 8. Cumulative Frequency Distribution of Residuals for Single Regression Model and Flow Weighted Model.

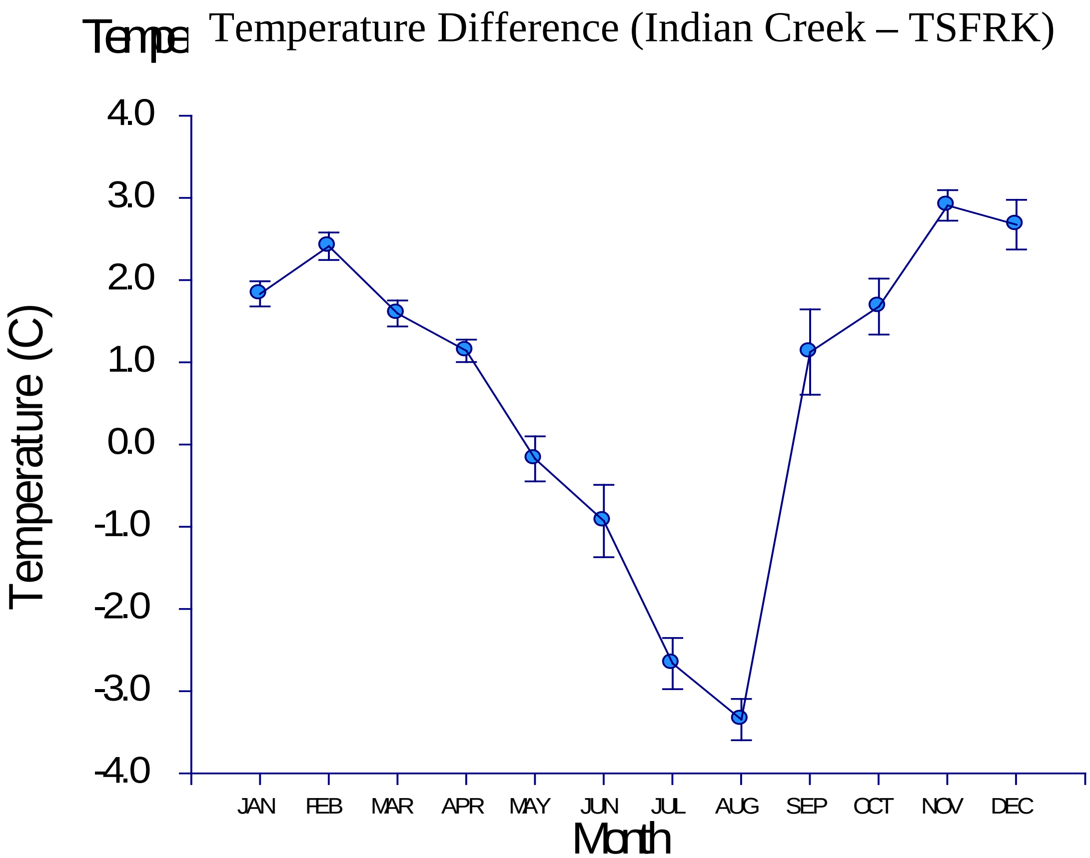

Figure 9. **Seasonal difference in average daily water temperatures between Stations TSFRK and ICT.**

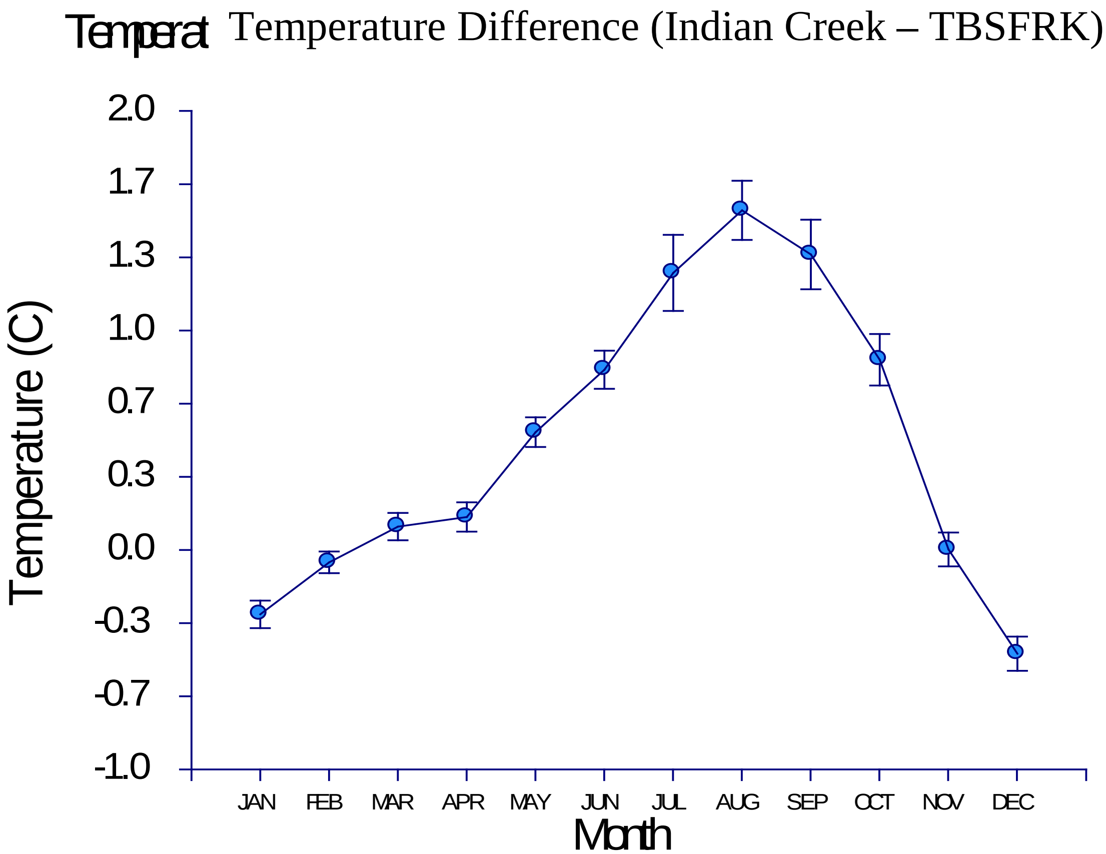

Figure 10. **Seasonal difference in average daily water temperatures between Stations TBSFRK and ICT.**

APPENDIX A

STATION TBSFRK

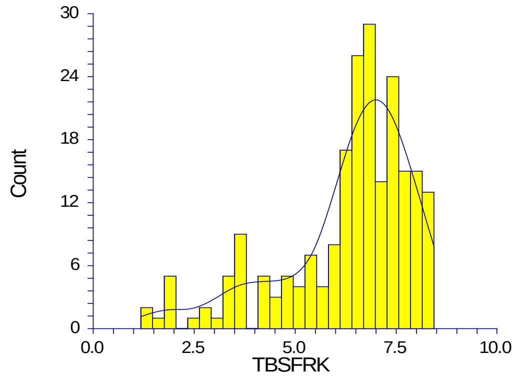

Plots Section of TBSFRK when Month=JAN

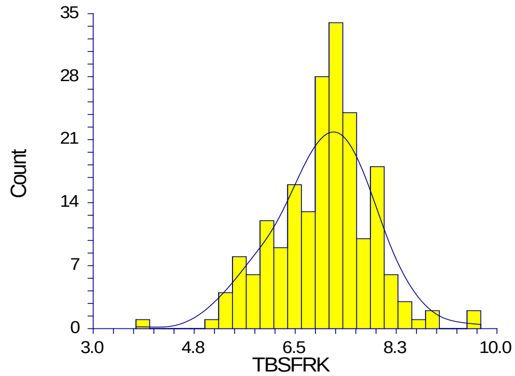

Plots Section of TBSFRK when Month=FEB

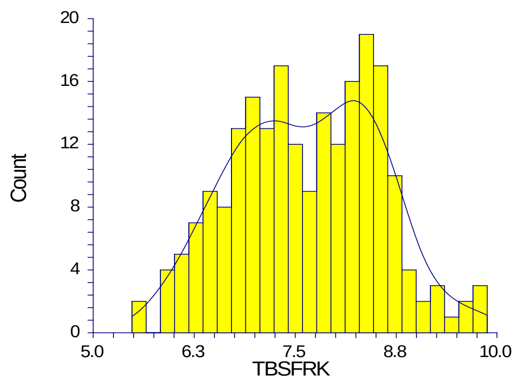

Plots Section of TBSFRK when Month=MAR

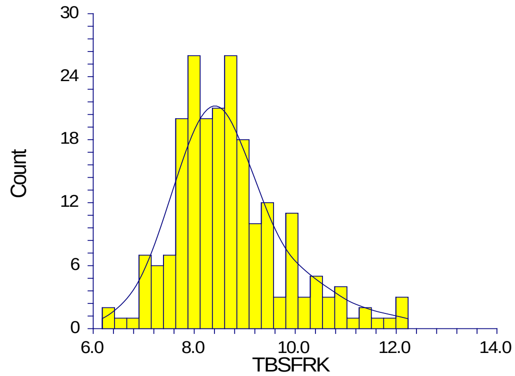

Plots Section of TBSFRK when Month=APR

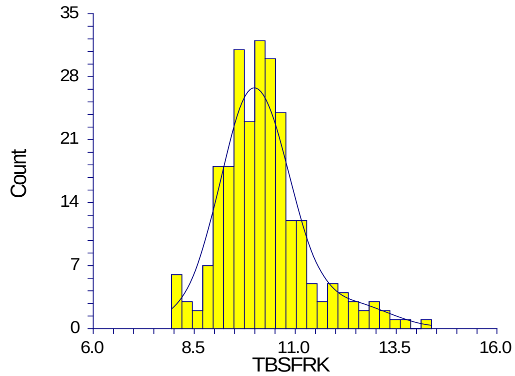

Plots Section of TBSFRK when Month=MAY

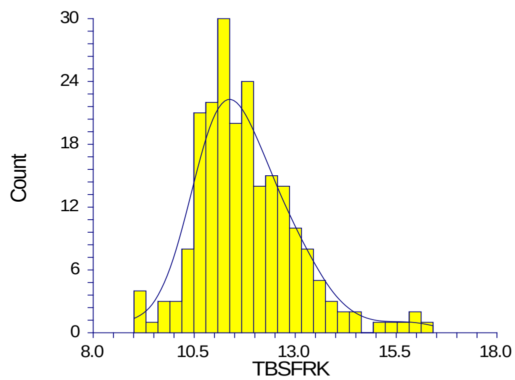

Plots Section of TBSFRK when Month=JUN

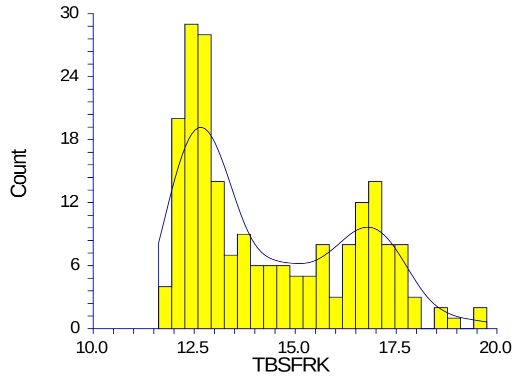

Plots Section of TBSFRK when Month=JUL

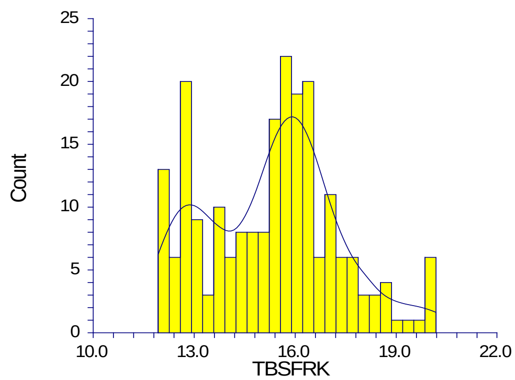

Plots Section of TBSFRK when Month=AUG

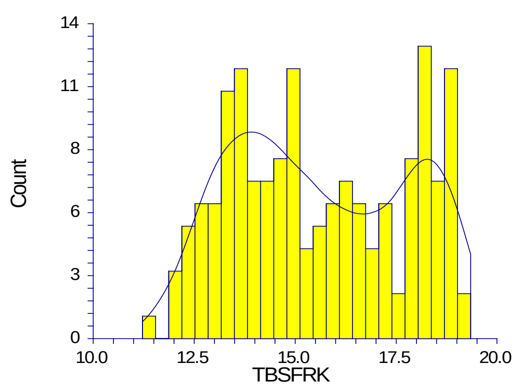

Plots Section of TBSFRK when Month=SEP

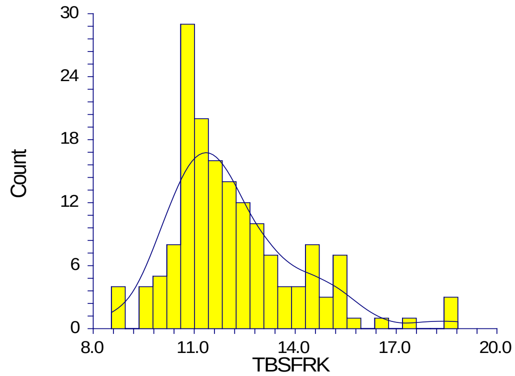

Plots Section of TBSFRK when Month=OCT

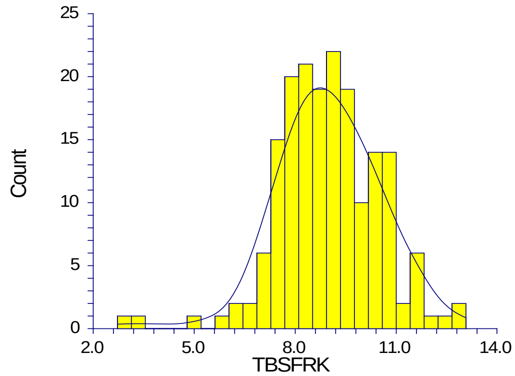

Plots Section of TBSFRK when Month=NOV

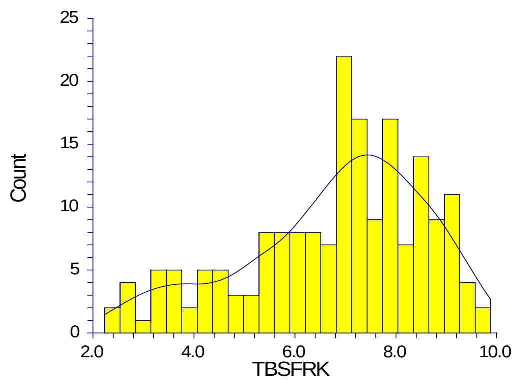

Plots Section of TBSFRK when Month=DEC

APPENDIX B

DESCRIPTIVE STATISTICS FOR WATER TEMPERATURE

Table 1. Descriptive Statistics for Observed Monthly Water Temperatures at TBSFRK, TRSRK, and TSFRK.

STATION: TBSFRK						
Month	**Count**	**Mean**	**Median**	**StdDev**	**Min**	**Max**
JAN	215	6.32	6.73	1.61	1.18	8.44
FEB	198	7.01	7.10	0.84	3.74	9.72
MAR	217	7.65	7.71	0.90	5.48	9.88
APR	214	8.71	8.56	1.10	6.18	12.24
MAY	248	10.22	10.15	1.07	7.94	14.38
JUN	215	11.78	11.57	1.24	9.01	16.42
JUL	208	14.38	13.68	2.04	11.62	19.75
AUG	217	15.31	15.59	1.98	11.93	20.19
SEP	160	15.60	15.22	2.14	11.22	19.35
OCT	161	12.13	11.72	1.89	8.54	18.84
NOV	180	8.99	8.97	1.50	2.72	13.08
DEC	186	6.79	7.09	1.78	2.23	9.88
STATION: TRSFRK						
Month	**Count**	**Mean**	**Median**	**StdDev**	**Min**	**Max**
JAN	217	6.72	7.20	1.48	1.89	8.76
FEB	198	7.32	7.43	0.71	5.35	8.86
MAR	216	7.76	7.75	0.77	5.93	10.01
APR	184	8.62	8.52	0.91	6.69	11.32
MAY	217	10.12	9.96	0.95	8.32	14.49
JUN	194	11.56	11.27	1.20	9.09	15.86
JUL	208	14.21	13.47	2.23	11.05	20.49
AUG	155	14.45	15.13	1.84	11.68	19.97
SEP	202	15.03	14.55	2.28	11.56	19.45
OCT	217	12.10	11.95	1.84	8.52	18.76
NOV	210	9.15	9.18	1.34	4.95	12.45
DEC	217	6.78	7.25	1.86	2.68	9.86
STATION: TSFRK						
Month	**Count**	**Mean**	**Median**	**StdDev**	**Min**	**Max**
JAN	200	3.38	3.36	1.42	-0.05	7.04
FEB	198	4.52	4.74	1.24	1.55	7.29
MAR	217	6.25	6.38	1.57	2.61	9.68
APR	214	8.10	7.95	1.70	4.14	12.74
MAY	238	10.74	10.07	2.60	5.36	17.84
JUN	183	14.67	14.28	3.12	7.69	20.89
JUL	183	19.95	20.30	2.15	13.93	23.36
AUG	186	19.99	19.21	2.11	15.88	25.00
SEP	202	17.23	17.13	2.37	13.26	24.07
OCT	202	12.10	11.83	2.09	6.79	19.81
NOV	150	7.61	7.83	1.90	2.79	12.33
DEC	183	3.86	3.76	1.85	0.57	8.39

APPENDIX C

STATION TRSFRK

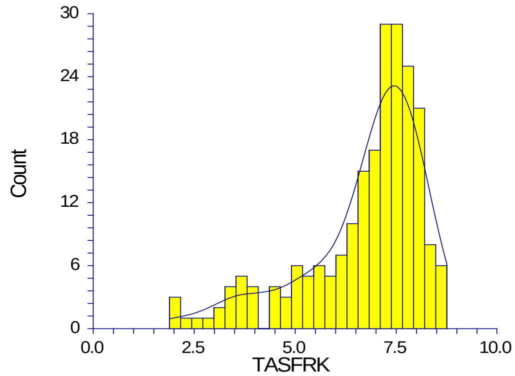

Plots Section of TRSFRK when Month=JAN

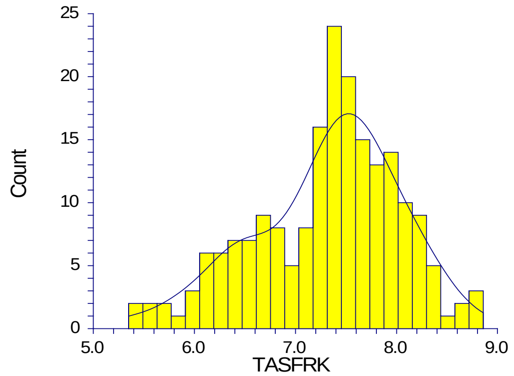

Plots Section of TRSFRK when Month=FEB

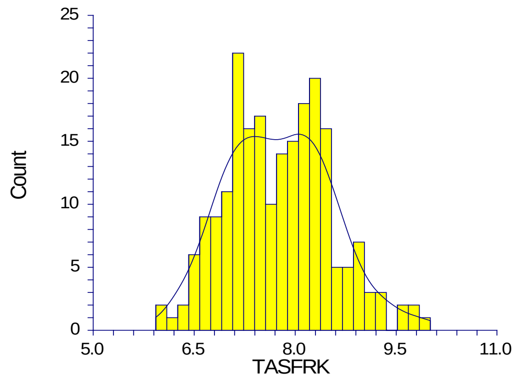

Plots Section of TRSFRK when Month=MAR

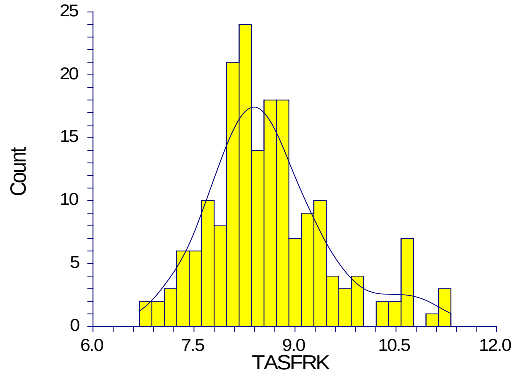

Plots Section of TRSFRK when Month=APR

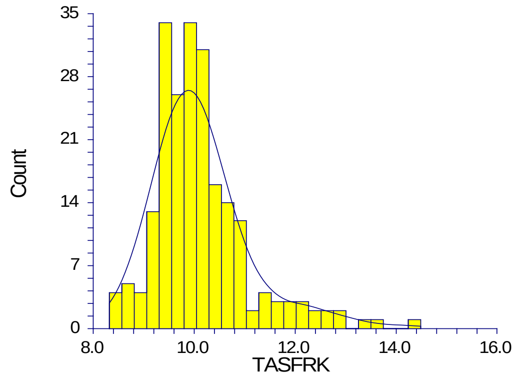

Plots Section of TRSFRK when Month=MAY

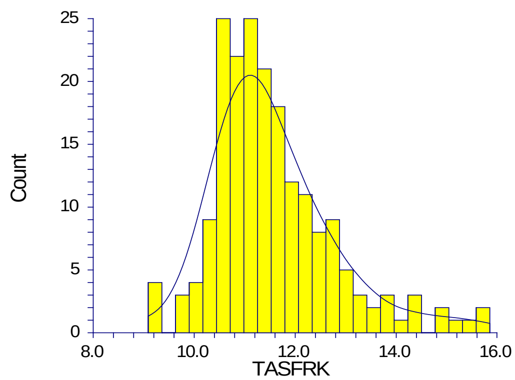

Plots Section of TRSFRK when Month=JUN

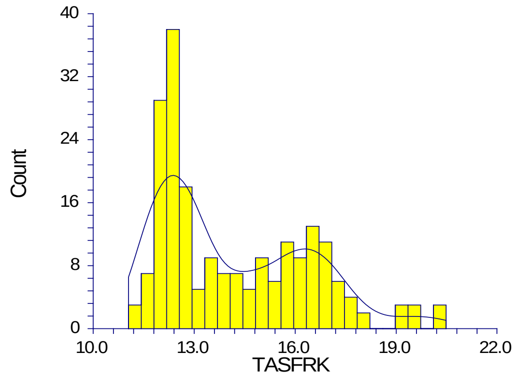

Plots Section of TRSFRK when Month=JUL

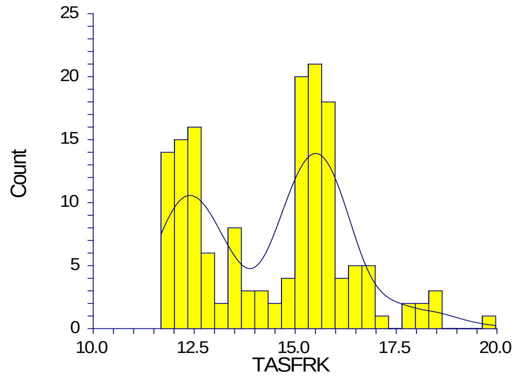

Plots Section of TRSFRK when Month=AUG

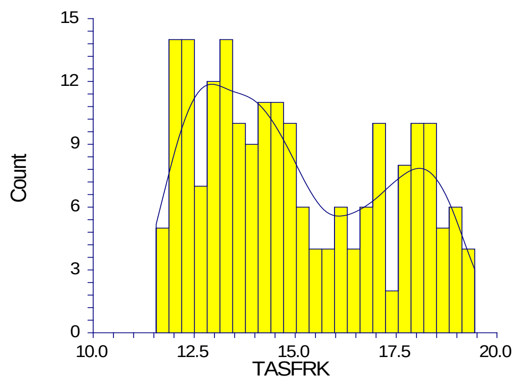

Plots Section of TRSFRK when Month=SEP

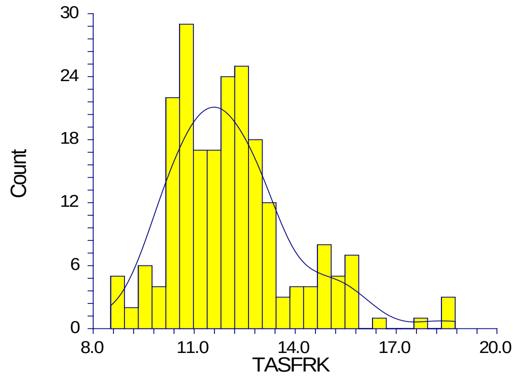

Plots Section of TRSFRK when Month=OCT

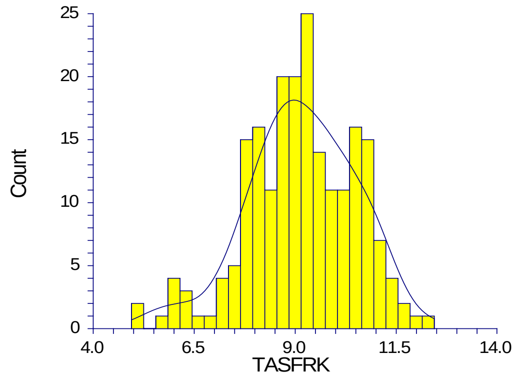

Plots Section of TRSFRK when Month=NOV

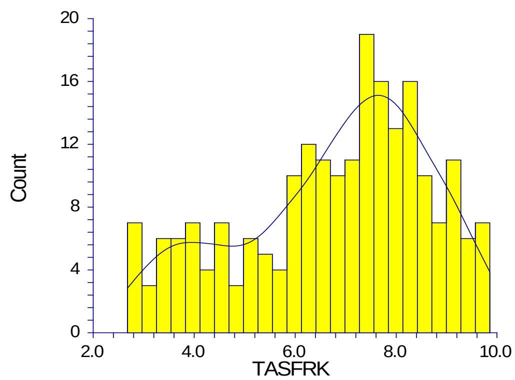

Plots Section of TRSFRK when Month=DEC

APPENDIX D

STATION TSFRK

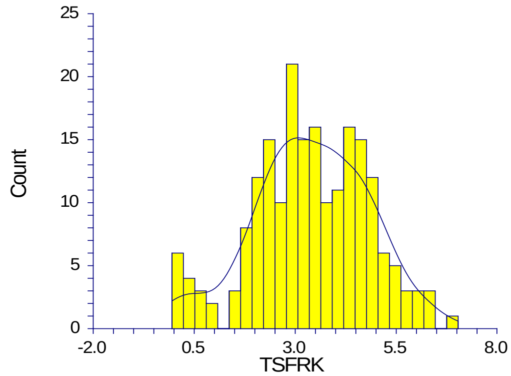

Plots Section of TSFRK when Month=JAN

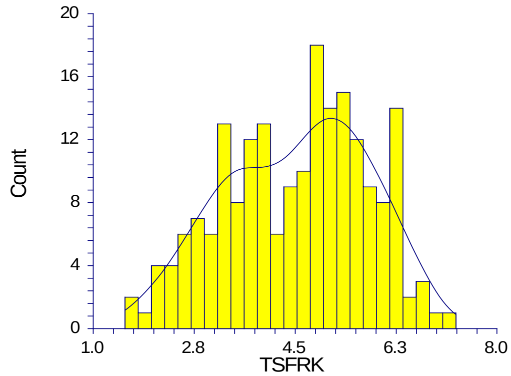

Plots Section of TSFRK when Month=FEB

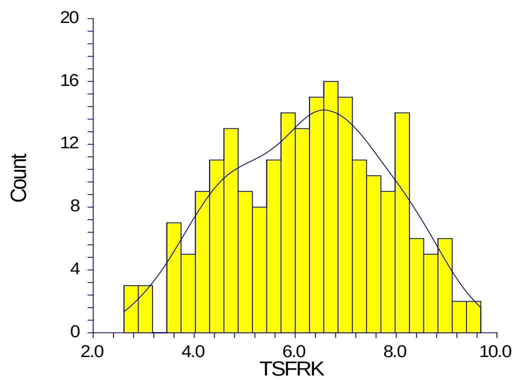

Plots Section of TSFRK when Month=MAR

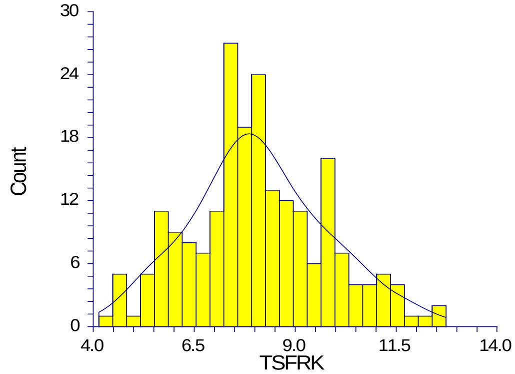

Plots Section of TSFRK when Month=APR

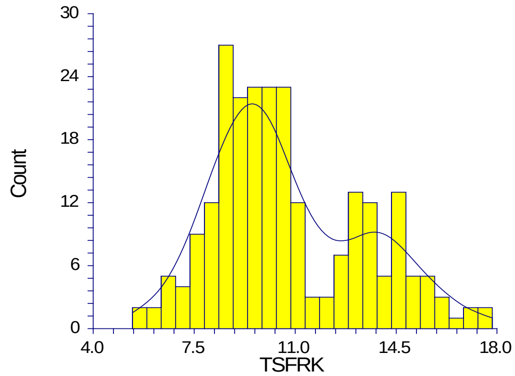

Plots Section of TSFRK when Month=MAY

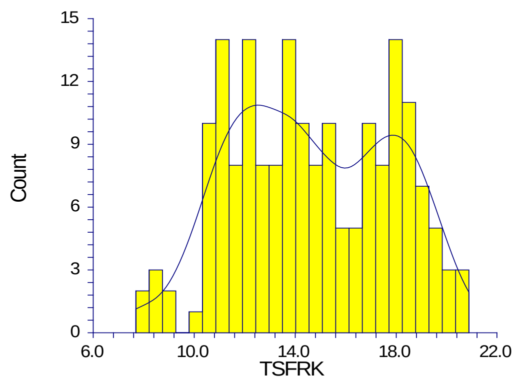

Plots Section of TSFRK when Month=JUN

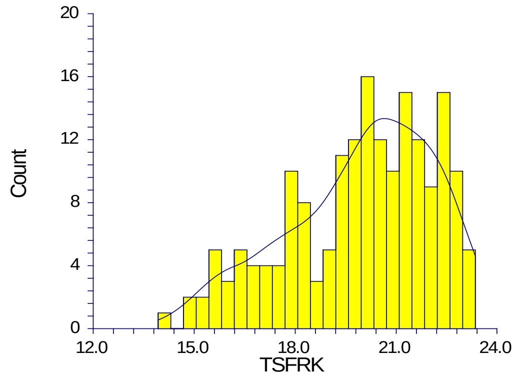

Plots Section of TSFRK when Month=JUL

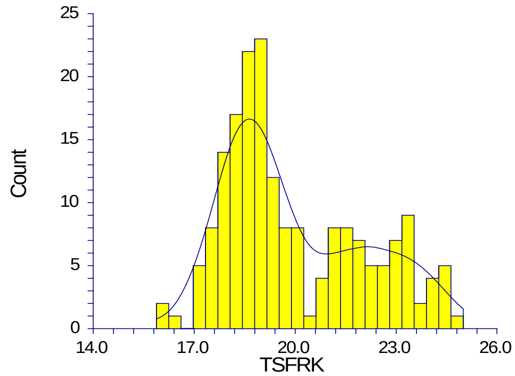

Plots Section of TSFRK when Month=AUG

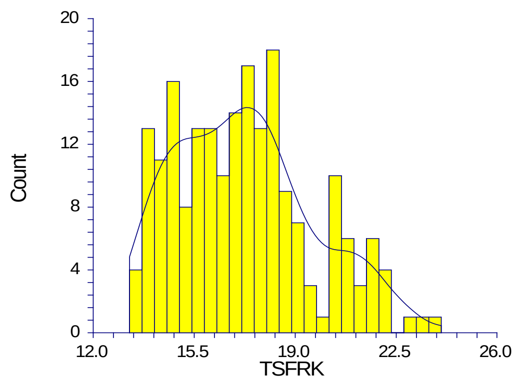

Plots Section of TSFRK when Month=SEP

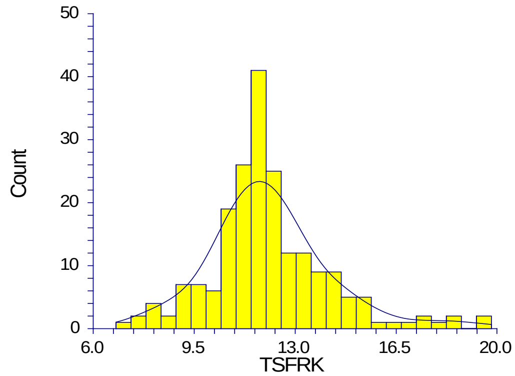

Plots Section of TSFRK when Month=OCT

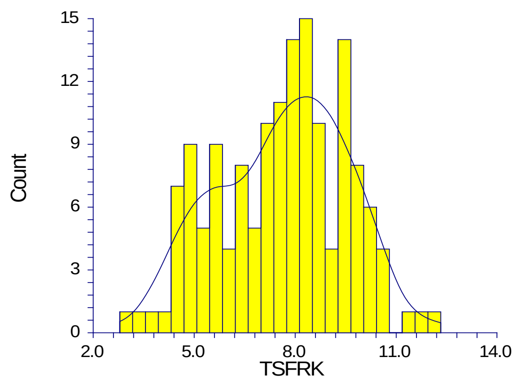

Plots Section of TSFRK when Month=NOV

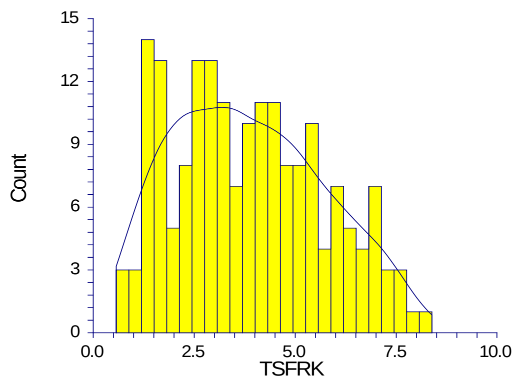

Plots Section of TSFRK when Month=DEC

APPENDIX E

STATION ICT – TSFRK

Summary Section of Diff when MM=JAN

Count	Mean	Standard Deviation	Standard Error	Minimum	Maximum	Range
76	1.833421	0.6673121	7.654595E-02	-0.07	3.3	3.37

Plots Section of Diff when MM=JAN

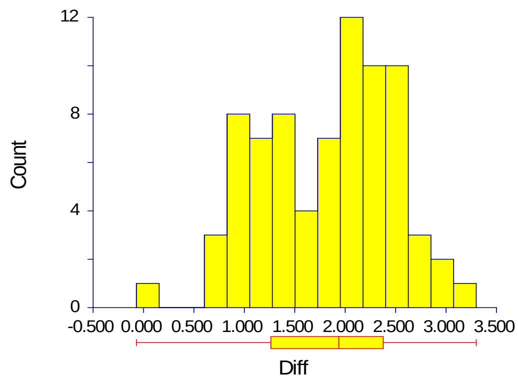

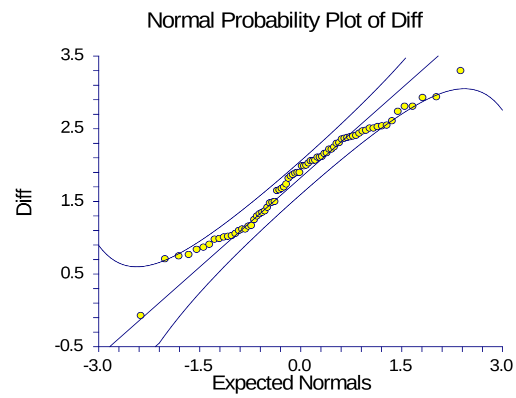

Summary Section of Diff when MM=FEB

Count	Mean	Standard Deviation	Standard Error	Minimum	Maximum	Range
85	2.412706	0.7717997	8.371343E-02	0.58	3.74	3.16

Plots Section of Diff when MM=FEB

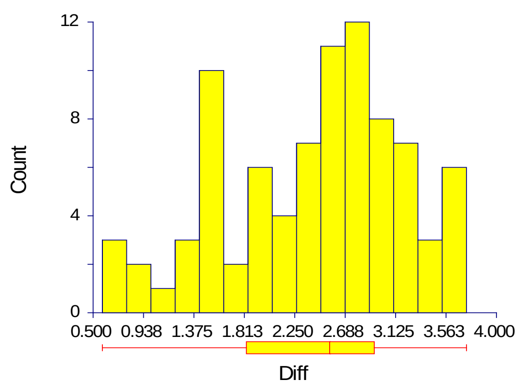

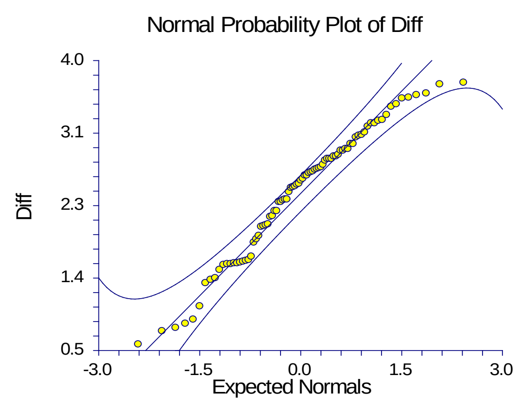

Summary Section of Diff when MM=MAR

Count	Mean	Standard Deviation	Standard Error	Minimum	Maximum	Range
93	1.594731	0.7626122	0.0790792	0.22	3.42	3.2

Plots Section of Diff when MM=MAR

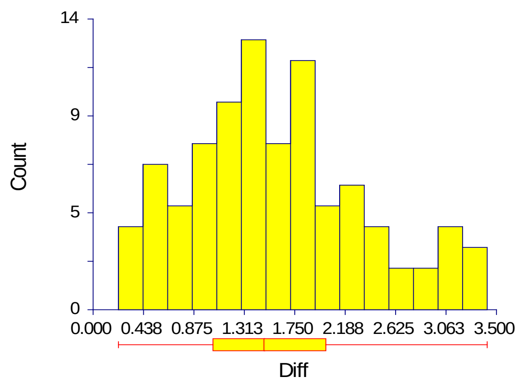

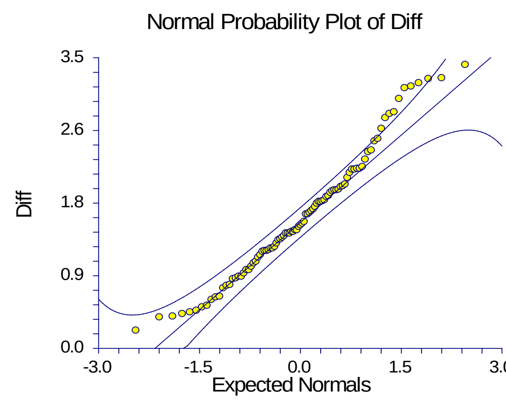

Summary Section of Diff when MM=APR

Count	Mean	Standard Deviation	Standard Error	Minimum	Maximum	Range
94	1.140426	0.6621518	6.829574E-02	-0.1	2.85	2.95

Plots Section of Diff when MM=APR

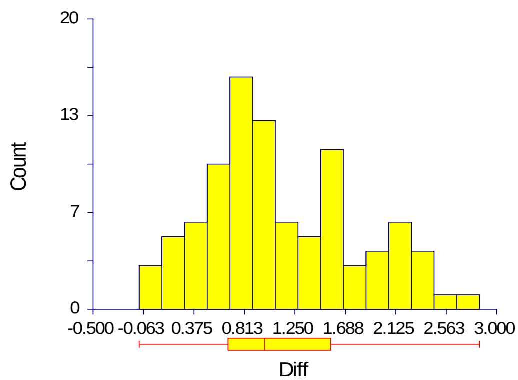

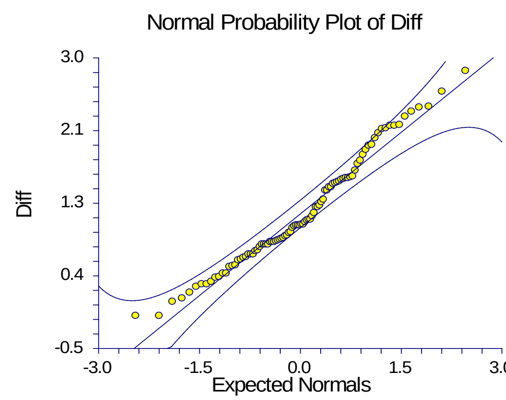

Summary Section of Diff when MM=MAY

Count	Mean	Standard Deviation	Standard Error	Minimum	Maximum	Range
101	-0.1738614	1.374295	0.1367474	-2.84	2.25	5.09

Plots Section of Diff when MM=MAY

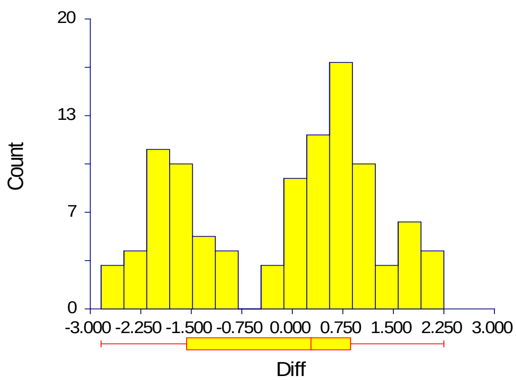

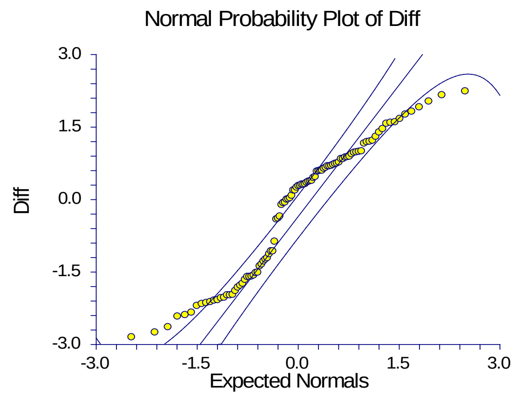

Summary Section of Diff when MM=JUN

Count	Mean	Standard Deviation	Standard Error	Minimum	Maximum	Range
74	-0.9294595	1.891714	0.2199072	-6.68	1.71	8.39

Plots Section of Diff when MM=JUN

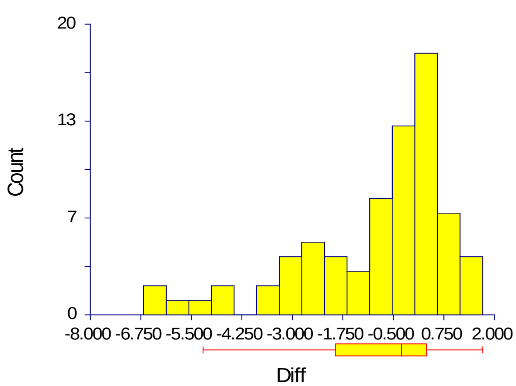

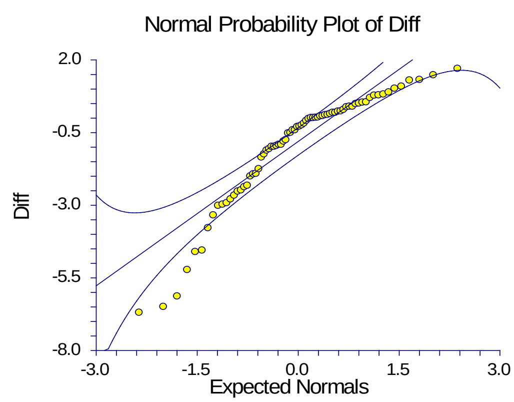

Summary Section of Diff when MM=JUL

Count	Mean	Standard Deviation	Standard Error	Minimum	Maximum	Range
56	-2.66375	1.163666	0.1555014	-6.37	0.91	7.28

Plots Section of Diff when MM=JUL

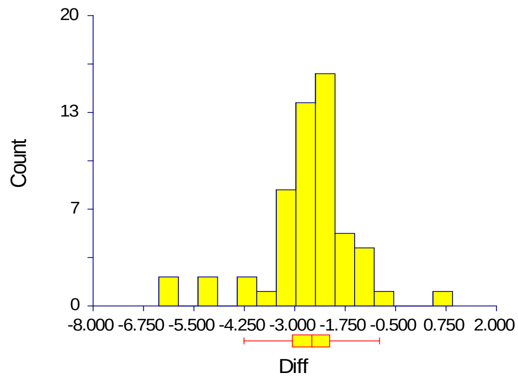

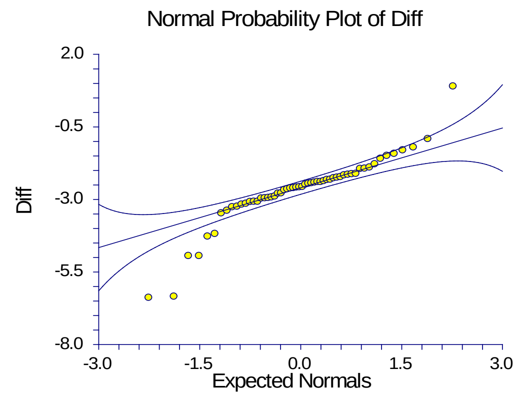

Summary Section of Diff when MM=AUG

Count	Mean	Standard Deviation	Standard Error	Minimum	Maximum	Range
31	-3.345161	0.6976765	0.1253064	-4.97	-2.17	2.8

Plots Section of Diff when MM=AUG

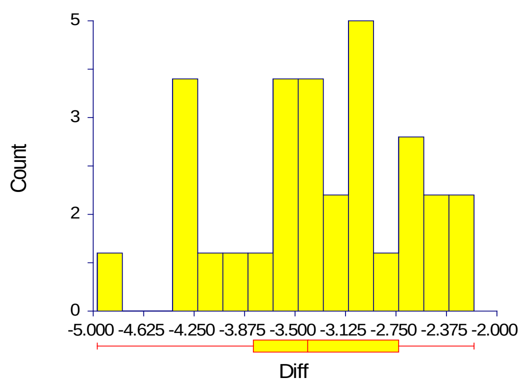

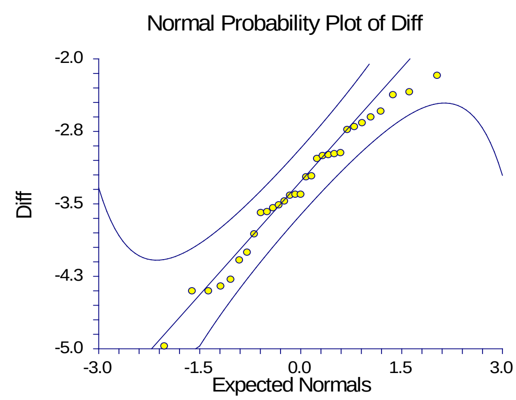

Summary Section of Diff when MM=SEP

Count	Mean	Standard Deviation	Standard Error	Minimum	Maximum	Range
52	1.125385	1.870636	0.2594106	-4.16	3.41	7.57

Plots Section of Diff when MM=SEP

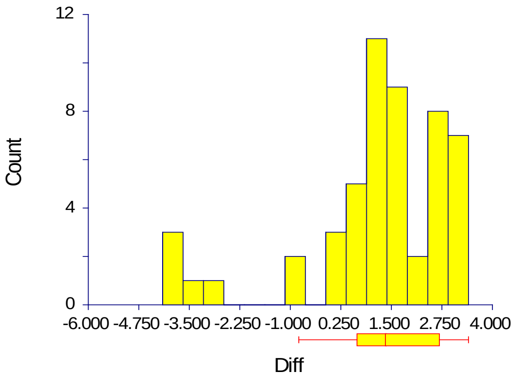

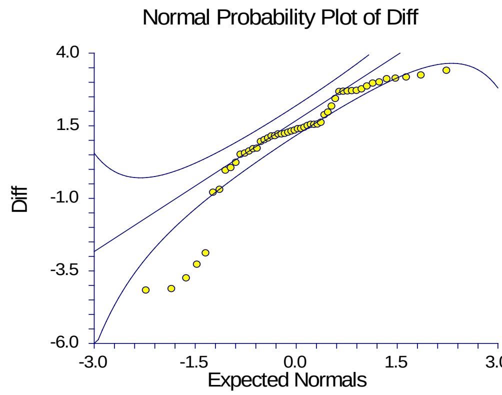

Summary Section of Diff when MM=OCT

Count	Mean	Standard Deviation	Standard Error	Minimum	Maximum	Range
78	1.678846	1.505353	0.1704477	-1.55	5.33	6.88

Plots Section of Diff when MM=OCT

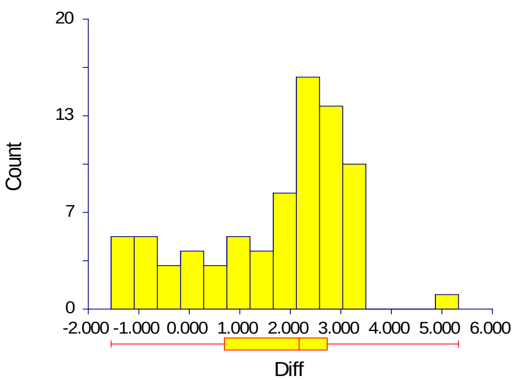

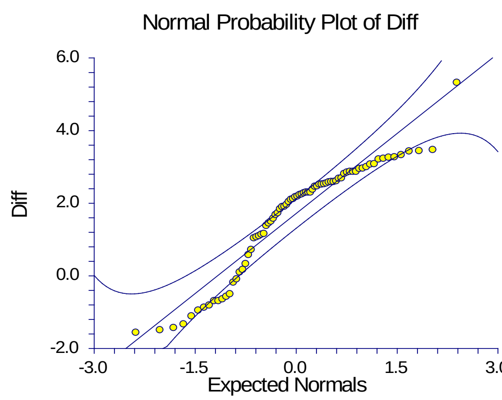

Summary Section of Diff when MM=NOV

Count	Mean	Standard Deviation	Standard Error	Minimum	Maximum	Range
30	2.909333	0.508242	9.279186E-02	2.21	3.98	1.77

Plots Section of Diff when MM=NOV

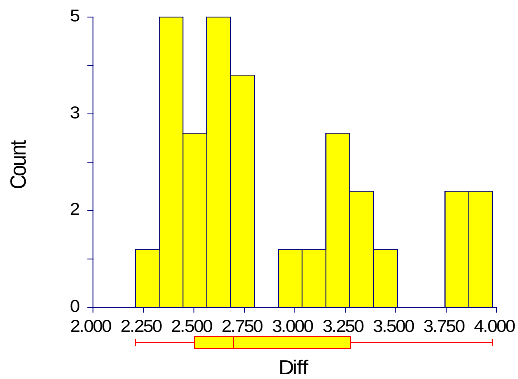

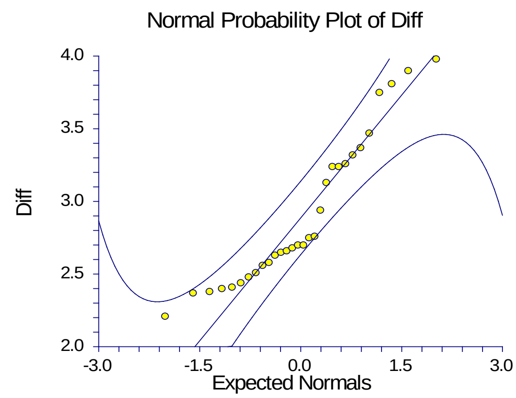

Summary Section of Diff when MM=DEC

Count	Mean	Standard Deviation	Standard Error	Minimum	Maximum	Range
59	2.675254	1.159795	0.1509925	0.44	5.18	4.74

Plots Section of Diff when MM=DEC

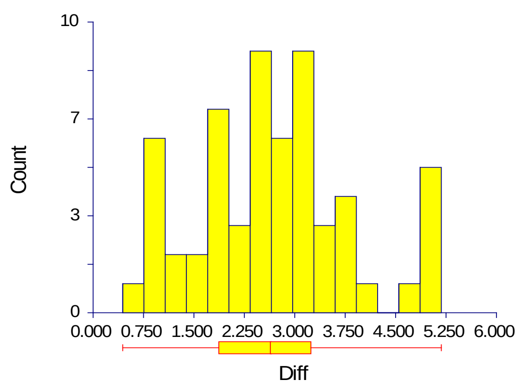

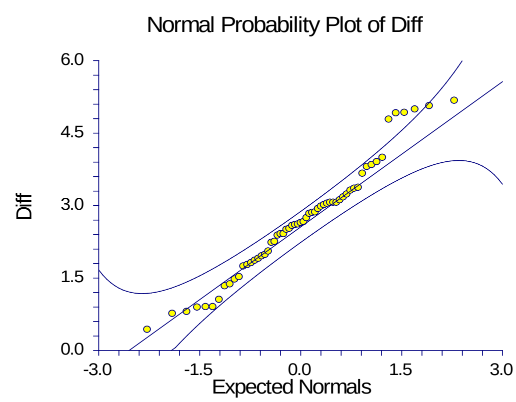

APPENDIX F

STATION ICT – TBSFRK

Summary Section of Diff2 when MM=JAN

Count	Mean	Standard Deviation	Standard Error	Minimum	Maximum	Range
93	-0.2934408	0.3027608	3.139484E-02	-1.25	0.39	1.64

Plots Section of Diff2 when MM=JAN

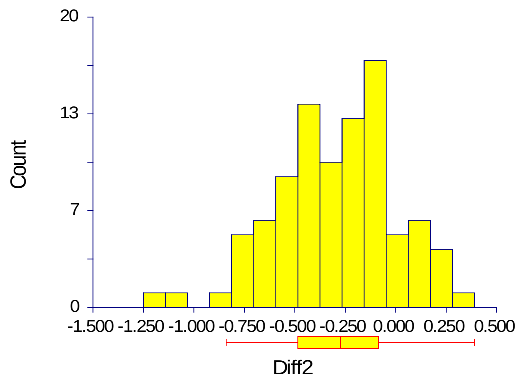

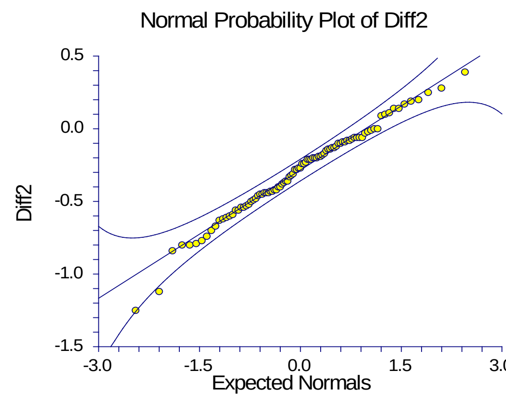

Summary Section of Diff2 when MM=FEB

Count	Mean	Standard Deviation	Standard Error	Minimum	Maximum	Range
85	-5.658824E-02	0.2277873	0.024707	-0.53	0.66	1.19

Plots Section of Diff2 when MM=FEB

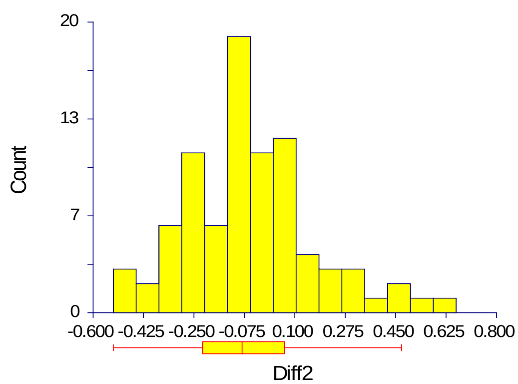

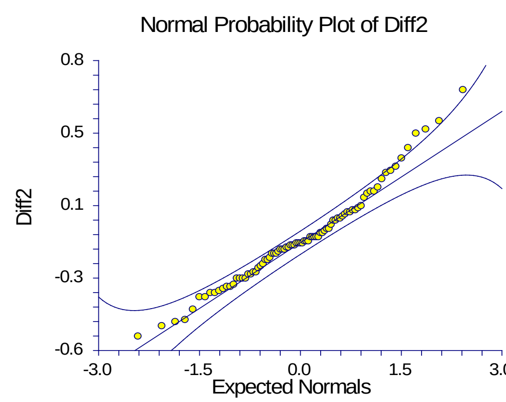

Summary Section of Diff2 when MM=MAR

Count	Mean	Standard Deviation	Standard Error	Minimum	Maximum	Range
93	0.1062366	0.3007198	3.118319E-02	-0.74	0.67	1.41

Plots Section of Diff2 when MM=MAR

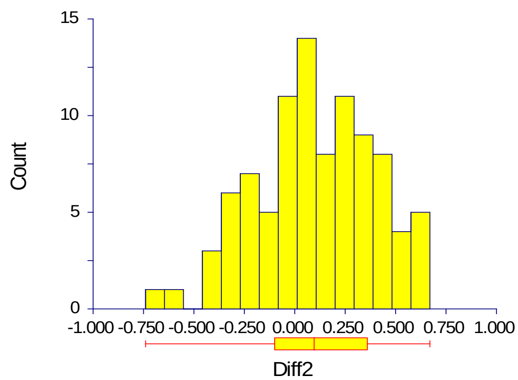

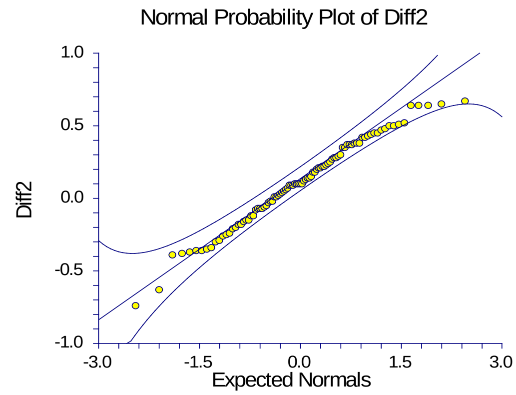

Summary Section of Diff2 when MM=APR

Count	Mean	Standard Deviation	Standard Error	Minimum	Maximum	Range
94	0.15	0.3239773	3.341571E-02	-0.64	0.69	1.33

Plots Section of Diff2 when MM=APR

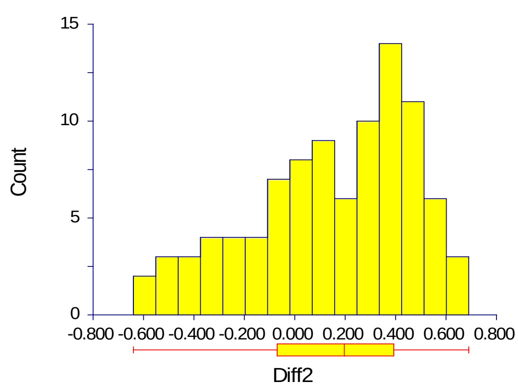

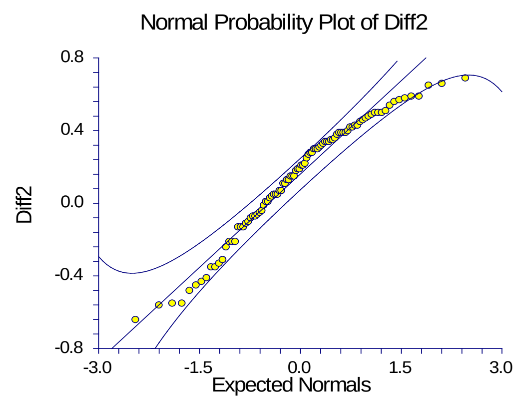

Summary Section of Diff2 when MM=MAY

Count	Mean	Standard Deviation	Standard Error	Minimum	Maximum	Range
101	0.5364357	0.3401017	3.384138E-02	-0.4	1.75	2.15

Plots Section of Diff2 when MM=MAY

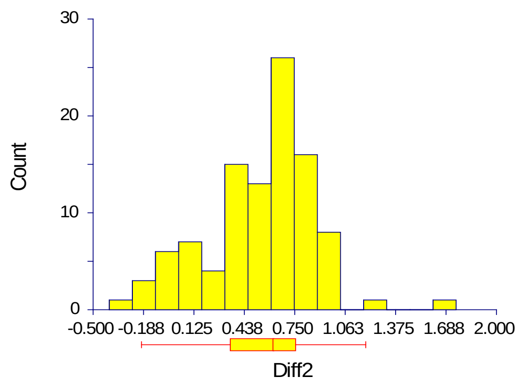

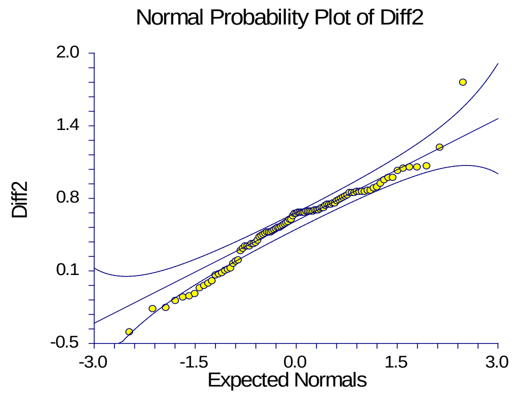

Summary Section of Diff2 when MM=JUN

Count	Mean	Standard Deviation	Standard Error	Minimum	Maximum	Range
74	0.8209459	0.3734774	4.341587E-02	0.1	1.88	1.78

Plots Section of Diff2 when MM=JUN

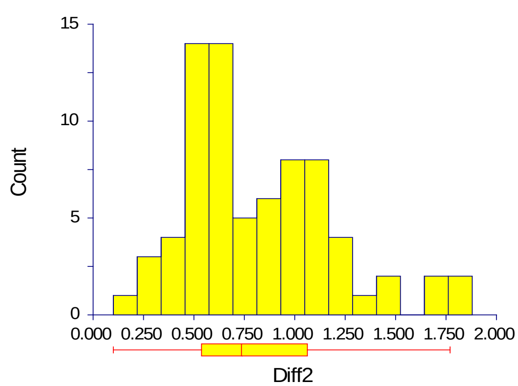

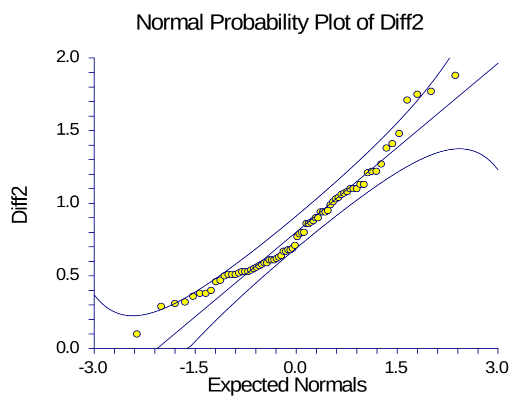

Summary Section of Diff2 when MM=JUL

Count	Mean	Standard Deviation	Standard Error	Minimum	Maximum	Range
62	1.262097	0.683072	8.675023E-02	-0.74	3.75	4.49

Plots Section of Diff2 when MM=JUL

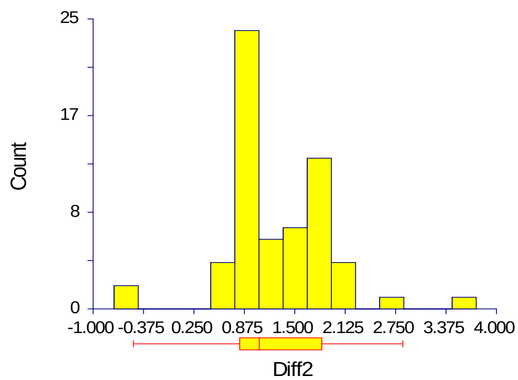

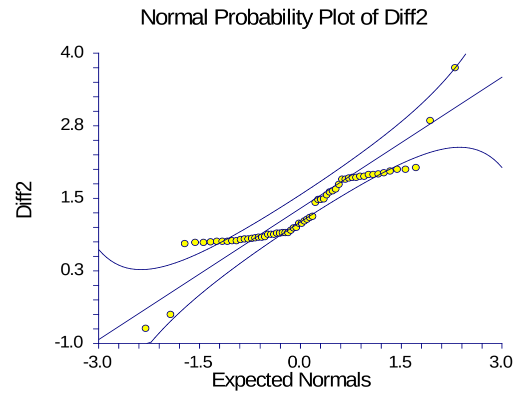

Summary Section of Diff2 when MM=AUG

Count	Mean	Standard Deviation	Standard Error	Minimum	Maximum	Range
62	1.547097	0.5309638	6.743247E-02	-0.51	3.06	3.57

Plots Section of Diff2 when MM=AUG

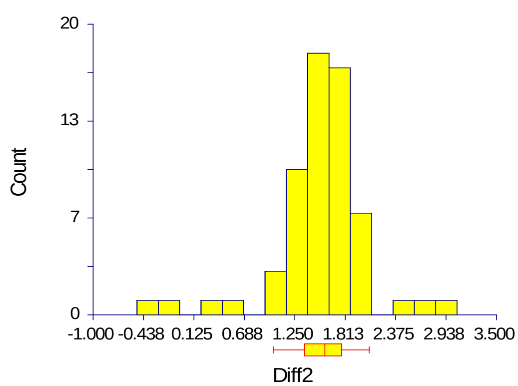

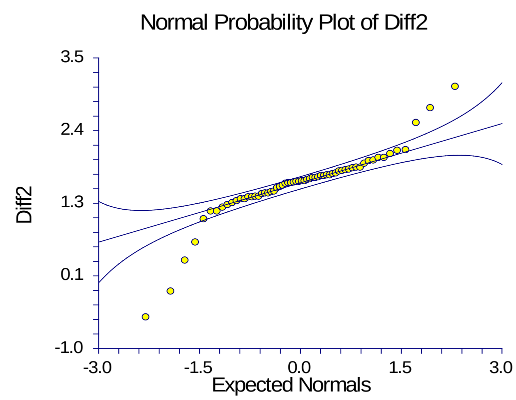

Summary Section of Diff2 when MM=SEP

Count	Mean	Standard Deviation	Standard Error	Minimum	Maximum	Range
60	1.346	0.6142439	7.929855E-02	-0.78	2.93	3.71

Plots Section of Diff2 when MM=SEP

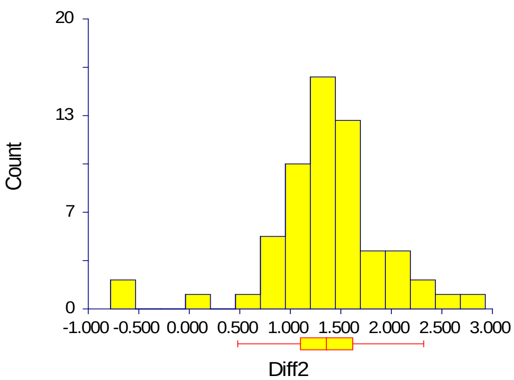

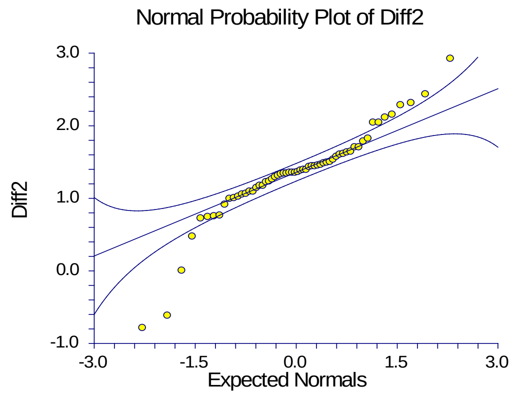

Summary Section of Diff2 when MM=OCT

Count	Mean	Standard Deviation	Standard Error	Minimum	Maximum	Range
93	0.8664516	0.5657213	5.866256E-02	-0.13	2.5	2.63

Plots Section of Diff2 when MM=OCT

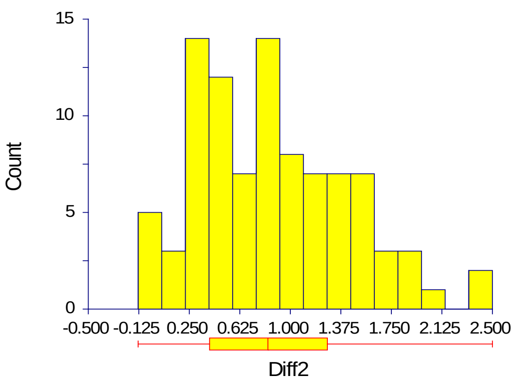

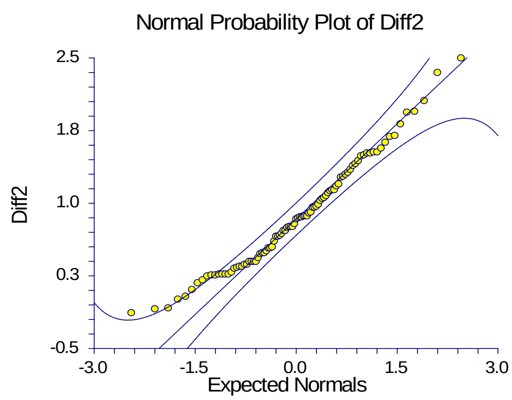

Summary Section of Diff2 when MM=NOV

Count	Mean	Standard Deviation	Standard Error	Minimum	Maximum	Range
90	2.222222E-03	0.3654942	3.852647E-02	-0.76	0.9	1.66

Plots Section of Diff2 when MM=NOV

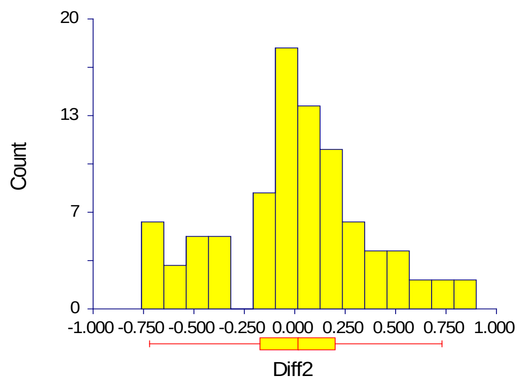

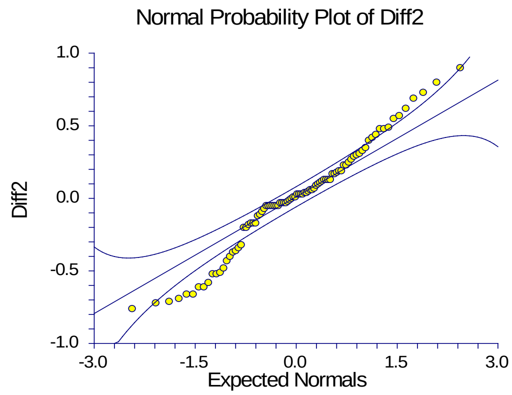

Summary Section of Diff2 when MM=DEC

Count	Mean	Standard Deviation	Standard Error	Minimum	Maximum	Range
93	-0.4726882	0.3762433	3.901461E-02	-1.37	0.24	1.61

Plots Section of Diff2 when MM=DEC